Feasibility Study on Conducting a Subcritical Molten Salt Reactor Experiment Using a DD Neutron Source

Master of Science Thesis - Engineering Physics

Author:
Mohammed H. Mahdi
Supervisors:
Dr. Adriaan Buijs
M.Eng Ron Robinson

April 2020

McMaster
University

Feasibility Study on Conducting a Subcritical Molten Salt Reactor Experiment Using a DD Neutron Source

Evaluation of Different Reactivity Measurement Methods

by

Mohammed H. Mahdi, B.Sc (Eng)

A Thesis
Submitted to the School of Graduate Studies
in Partial Fulfillment of the Requirements
for the Degree
Master of Science

McMaster University - Department of Engineering Physics

MASTER OF SCIENCE (2020)	McMaster University
(Engineering Physics)	Hamilton, Ontario, Canada

TITLE:	Feasibility Study on Conducting a Subcritical Molten Salt Reactor Experiment Using a DD Neutron Source: Evaluation of Different Reactivity Measurement Methods
AUTHOR:	Mohammed Mahdi, B.Sc(Eng) (McMaster University, Hamilton, ON)
SUPERVISOR:	Dr. Adriaan Buijs
CO-SUPERVISOR:	M.Eng Ron Robinson
NUMBER OF PAGES:	xiv, 124

ABSTRACT

Over the last two decades, there has been widespread international interest in the development of the molten salt reactor concept due its passive safety, high coolant boiling temperature, low operational pressure, high thermal efficiency and ease of breeding. Terrestrial Energy Incorporated (TEI) is developing a thermal-spectrum converter type molten salt reactor, called the Integral Molten Salt Reactor (IMSR-400) to be built by 2030. A physics experiment is needed in order to validate the theoretical predictions of the temperature reactivity coefficients of the IMSR-400. This thesis will determine the feasibility of conducting a subcritical experiment, utilizing a Deuterium-Deuterium Fusion Neutron Source (DD).

ACKNOWLEDGEMENTS

My deepest gratitude to both, my academic supervisor at McMaster University, Dr. Adriaan Buijs, and my industrial supervisor at Terrestrial Energy Incorporation, M.Eng. Ron Robinson for the continues guidance and support throughout my research.

Many thanks to Terrestrial Energy Incorporation and Mitacs for funding my research.

Sincere thanks to the Canadian National Laboratories, personnel at the McMaster Nuclear Reactor and colleagues at the Department of Engineering Physics for providing me with information and data to help with my research.

My sincerest thanks to my fiancée, Daniela Dering, for supporting me throughout the years, and for helping me debug my MATLAB and LaTeXcodes. I love you with all my heart and soul.

Special thanks to my family, my mother Zakia Sindi, my father Hashem Mahdi, my step-mother Ghaida Hamoda, my sisters Ahood and Logain, and my brother Abdullah for helping me keep my sanity throughout my undergraduate and graduate studies.

Table of Contents

List of Figures

List of Tables

Chapter 1

Introduction

1.1 Nuclear Energy

Nuclear energy is a clean, sustainable and virtually limitless (on the time-scale of human existence) source of energy thanks to its lower emissions and significantly larger power density than carbon-based fuels. Current commercial nuclear reactors rely mostly on the fissioning of uranium-235, a fissile isotope of uranium, which is a naturally occurring radioactive element. Fission produces heat. Heat is used generate steam. Steam is used to turn turbines, generating electricity. A gram of uranium-235 contains five million times the energy in one gram of coal. On average, the abundance of natural uranium in the earth crust is about 2.7 ppm, and 0.003 ppm in seawater [Lumen Learning, 2020] [Lamarsh and Baratta, 2001, p. 199]. However, total uranium reserves in seawater are considered virtually limitless, but the extraction cost is still higher than mining uranium [Lamarsh and Baratta, 2001, p. 199]. Natural uranium is mainly 99.27% uranium-238 and 0.72% uranium-235 in weight [Lamarsh and Baratta, 2001, p. 46].

Today, there are 440 nuclear reactors that supply approximately 13% of the world's electricity, and 29% of all low-carbon energy [Government of Canada, 2020]. Compared to other energy sources, nuclear energy requires the least amount of land and natural resources.

The Bruce Power Generating Station in Ontario, for instance, supplies 20% of Ontario's electricity while occupying only 2300 acres (9.3 km^2) of land [Power Technology, 2017]. In the fight against climate change, nuclear energy has a proven track record in radical reduction of greenhouse gas emissions and air-pollution. In 2003, Ontario began phasing out coal-fired power plants while adding nuclear, non-hydro renewables and natural gas (as back-up) electric generation capacities to the grid. By 2014, Ontario had successfully eliminated all coal-based electric generation. The lost generation capacity was absorbed mainly by nuclear energy (72% of replaced capacity) [Government of Ontario, 2017].

Figure 1.1: Percentage share of total generation in Ontario for 2003 and 2014.

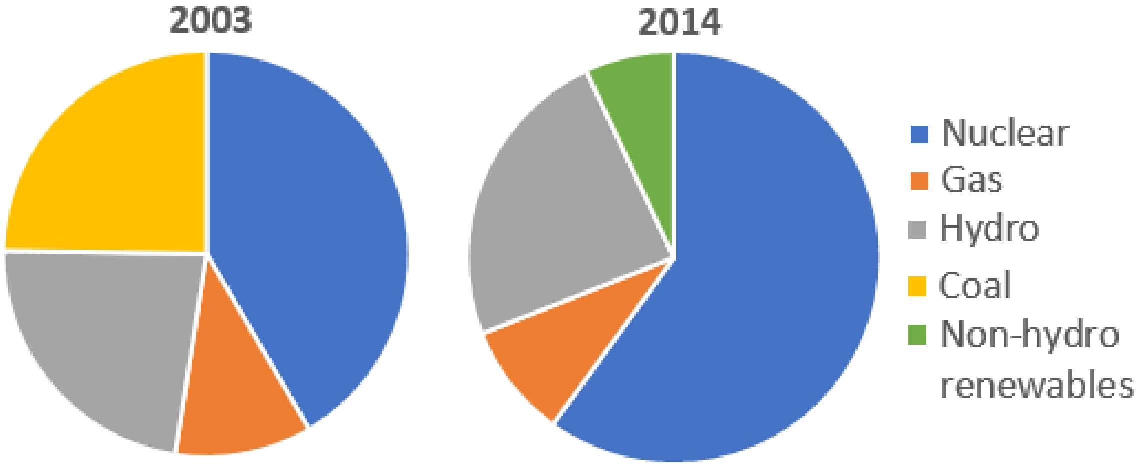

Greenhouse gas emissions and major air-pollutants were either drastically reduced, or completely eliminated. The average concentration of particulate matter (PM2.5) in 2018 was 20% less than it was in 2005 [Government of Ontario, 2017].

Figure 1.2: Total greenhouse gases, NOx, SOx and mercury emissions, and PM2.5 concentration relative to 2005.

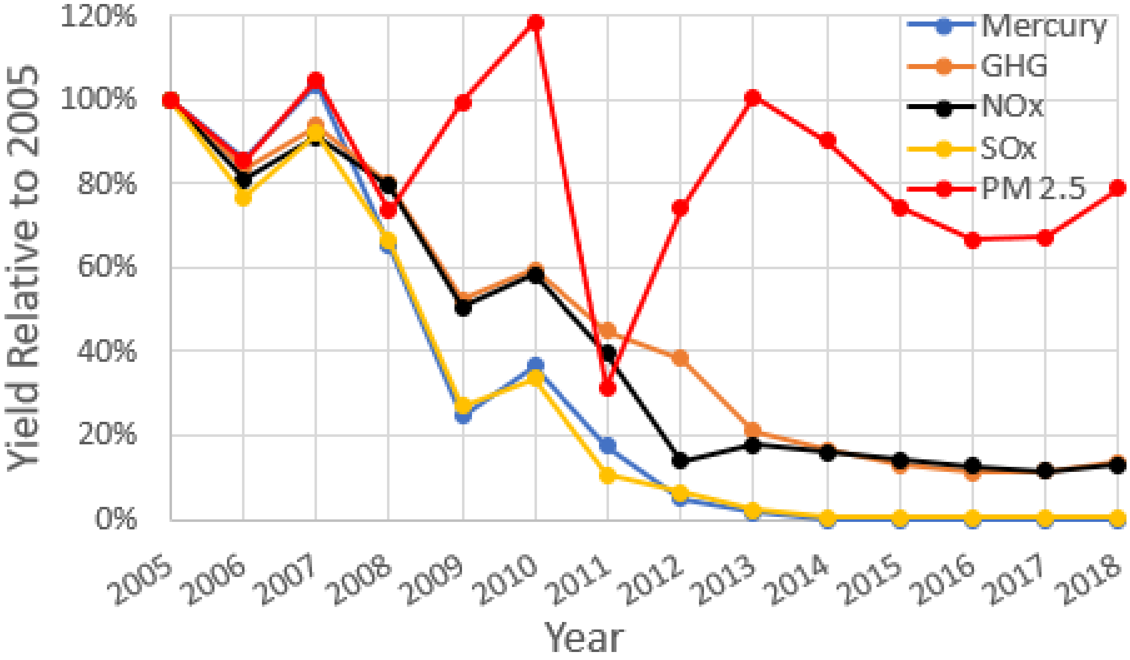

As a result of this initiative, Ontario was able to achieve 7% reduction in total greenhouse gas emissions below 1990 levels, exceeding its initially set target of 6%. In addition to significant improvement in air-quality, smog days have become a rare occurrence as of 2014, compared to 53 smog days in 2005. It is estimated that the annual mitigated health, financial and environmental costs from phasing out coal are approximately CAD$4.4 billion (2004 dollar value) [Government of Ontario, 2017].

The Intergovernmental Panel on Climate Change (IPCC) identified in its 2019 report four possible scenarios with four respective pathways to prevent a global temperature rise above 1.5 °C by 2050 [IPCC, 2019]. The first three scenarios base achievable deep decarbonization measures on both changing industrial habits, and adopting clean energy technologies. The fourth scenario assumes deep decarbonization is achievable only by large-scale implementation of clean energy technologies [IPCC, 2019]. According to the US Energy Information Administration (EIA), more than 50% rise in global energy demand is expected by 2050, mainly in Asia. Thus, even if developed countries (i.e. OECD) were committed to moderating industrial growth, it is unlikely that non-OECD countries will do the same [EIA, 2019]. According to the IPCC, meeting the growing energy demand while achieving climate goals in the fourth scenario would require five folds increase in the global share of nuclear energy by 2050 [IPCC, 2019].

The primary components of the heat generation system in most commercial nuclear reactors are:

- Mean of heat generation as uranium dioxide (UO_2) solid nuclear fuel.
- Mean of cooling as light water, heavy water, or carbon dioxide.
- Mean of neutron moderation as heavy water, light water or graphite.
- Mean of controlling the nuclear chain reaction as steel rods, gadolinium oxide rods, soluble boric acid, etc.

When a uranium-235 nucleus absorbs a slow moving neutron (i.e. thermal neutron), a highly unstable uranium-236 nuclide is formed momentarily, followed either by fission (82% probability), or by gamma ray release (18% probability). Fission yields two unstable nuclides (i.e. fission products), plus, two to three additional neutrons, resulting a cascade of fission events. Using a neutron moderator, composed of light atoms, fast neutrons born from fission can be thermalized (i.e. slowed down). Control rods, made of neutron absorbing materials, are used to control the rate of fission in the fuel. By allowing one neutron on average from every fission event to continue the chain reaction, while other neutrons are lost via parasitic absorption or leakage, the reactor becomes critical, and energy is produced at a constant rate.

The ratio of the neutron production rate to the neutron loss rate is described as the effective multiplication factor (k_{eff}). A reactor is called critical when k_{eff} equal one, subcritical when k_{eff} is less than one, and supercritical when k_{eff} is greater than one. The thermal power remains constant if the reactor is critical, decreases at a certain rate if subcritical, and increases at a certain rate if supercritical. Achieving and maintaining criticality is essential in reactor operation for both safety and economical reasons. Whereas the fuel and the moderator are means of boosting the chain reaction, control rods are a mean of suppressing the chain reaction. As time passes, uranium-235 is slowly consumed, and the chain reaction slows down. As a long term measure of keeping the reactor critical, old fuel is removed from the reactor and new fuel is added. In order to keep the fuel in the reactor for a longer period, hence, reducing the frequency of refueling, it is a common practice to increase the uranium-235 content in the total mass of uranium, described as the enrichment process. Relying on the mass difference between uranium-238 and uranium-235, various known techniques can be used to enrich uranium such as gaseous diffusion and gas centrifuge enrichment techniques. Enrichment levels can be classified into four groups [Wilson, 1996]:

- Natural uranium (NU): 0.72% uranium-235 in weight.
- Low-enriched uranium (LEU): more than 0.72% up to 5.0% uranium-235 in weight.
- High-assay low-enriched uranium (HALEU): more than 5% up to 20% uranium-235 in weight.
- Highly-enriched uranium (HEU): more than 20% up to 90% uranium-235 in weight.

NU, LEU and HALEU are most common in commercial power and research reactors. The use of HEU is uncommon in civilian nuclear reactors, but still can be found today in nuclear-powered submarines and icebreakers. Since uranium metal has a relatively low melting point (1132 °C), uranium dioxide (UO_2) is the standard fuel material in most commercial nuclear reactors. In addition to the high melting point of UO_2 (2865 °C), advantages to using UO_2 include a robust crystal structure for effective entrapment of fission products, chemical stability, high yield strength and low solubility in water.

The main useful product of fission is heat. The most common type of commercial power reactors in the world is the light water cooled reactor, where water is used for cooling, neutron moderation and generating steam for electricity production. However, the magnitude of extractable useful energy is limited by the coolant's thermophysical properties. Water has favourable thermophysical properties and is also nontoxic, making it ideal for purposes of cooling and power generation. Nevertheless, in comparison to gas, molten salt or liquid metal cooled reactors, the thermal efficiency of pressurized water-cooled reactors is relatively lower due to the limitations on heat transfer, imposed by the low boiling temperature of water [Pioro, 2016]. Additionally, in the event of accidental depressurization of the system due to a main pipe break event, liquid water would boil into steam incautiously, resulting in a loss of the cooling capability of the core, potentially leading to fuel melting. Nevertheless, modern nuclear reactors have highly redundant, highly reliable and fast-acting safety and emergency systems, rendering such accidents extremely rare and limiting severe consequence to the immediate vicinity of the reactor vessel. According to the World Health Organization, global fatalities due to nuclear energy in deaths per trillion-watt-hour (including Chernobyl and Fukushima) is 90 compared to 440 for solar energy and 150 for wind energy [Conca, 2012].

1.2 Generation IV Nuclear Reactors

In January 2000, representatives from nine nuclear countries discussed the potential of a large scale collaboration to develop new reactor designs, called the "generation IV nuclear reactors". The meeting, organized by the US Department of Energy (DOE), was concluded by the formation of the Generation IV International Forum (GIF). Among numerous design candidates, only six design concepts were considered by GIF, namely:

- The Gas-cooled Fast Reactor (GFR)
- The Lead-cooled Fast Reactor (LFR)
- The Molten Salt Reactor (MSR)
- The Supercritical Water-Cooled Reactor (SCWR)
- The Sodium-cooled Fast Reactor (SFR)

- The Very High Temperature Reactor (VHTR)

The respective designs were favoured for satisfying several qualities, which the GIF considered essential if generation-IV reactors were to be more efficient and cost-competitive with fossil fuels. These qualities are:

Table 1.1: Conceptual design criteria of Generation IV nuclear reactors as envisioned by GIF [Pioro, 2016].

Generation IV Conceptual Design Criteria	
Sustainability	Generation IV nuclear energy systems will provide sustainable energy generation that meets clean air objectives and provides long-term availability of systems and effective fuel utilization for worldwide energy production. Generation IV nuclear energy systems will minimize and manage their nuclear waste and notably reduce the long-term stewardship burden, thereby improving protection for the public health and the environment.
Economics	Generation IV nuclear energy systems will have a clear lifecycle cost advantage over other energy sources. Generation IV nuclear energy systems will have a level of financial risk comparable to other energy projects.
Safety and Reliability	Generation IV nuclear energy systems operations will excel in safety and reliability. Generation IV nuclear energy systems will have a very low likelihood and degree of reactor core damage. Generation IV nuclear energy systems will eliminate the need for offsite emergency response.
Proliferation Resistance and Physical Protection	Generation IV nuclear energy systems will increase the assurance that they are very unattractive and the least desirable route for diversion or theft of weapons usable materials, and provide increased physical protection against acts of terrorism.

In summary, the generation IV reactors are expected to be cheaper to build, inherently safer, produce less radioactive waste and be more energy efficient [Pioro, 2016]. As most designs are still in the early stages, more research and development are needed to resolve some of the technological issues relating to material, operation, maintenance, and disposal of spent fuel. In Canada, stakeholders in the nuclear industry have been particularly interested in the Molten Salt Reactor design concept thanks to its inherent safety and high thermal efficiency. There are currently two companies working on the Molten Salt Reactor design concept, Terrestrial Energy Incorporated (TEI) in Ontario and Moltex Energy Incorporated in New Brunswick.

1.3 Overview of IMSR-400

The Integral Molten Salt Reactor (IMSR-400) is a thermal spectrum converter-type small modular molten salt reactor design, currently under development by TEI to become commercially available by 2030 [Terrestrial Energy In, 2016a]. The IMSR-400's normal operation heat transport system consists of three main loops:

- Primary loop, containing liquid fuel salt (fluoride salts mixture) that acts as fuel and coolant, generating heat when passing through the core and then rejecting heat to the secondary loop through a shell and tube heat exchanger.
- Secondary loop, containing cooling salt (fluoride salts mixture without uranium) that removes heat from the primary loop.
- Tertiary loop, containing cooling water, used to generate steam to turn turbines and generate electricity.

The fuel salt is composed of a unique mixture of fluoride salts, developed and owned by TEI. The primary fissile isotope is uranium-235, which is diluted into the fuel salt mixture in the form of uranium tetrafluoride (UF_4), enriched to about 2 to 3 %. A predominantly thermal spectrum is achieved through the use of high-density low-porosity high purity nuclear grade

Table 1.2: Summarized IMSR-400 core specifications

Design Parameter	**Details**
Thermal power	400 MW
Gross electric power	194-202 MW
Active core height	4 m
Active core diameter	3.4 m
Fuel enrichment	2-3%
Makeup fuel enrichment (online refueling)	5-19%
Shutdown rods material (no control rods)	Gadolinium oxide
Core inlet temperature	625-660 ^{o}C
Core outlet temperature	670-700 ^{o}C
Average temperature change across the core	75 ^{o}C

graphite for neutron moderation and reflection. The projected thermal and electrical power capacities are 400 MW and 194 MW respectively (nearly 50% thermal efficiency). Core design parameters such as height-to-diameter ratio, pitch distance, fuel-to-moderator ratio were optimized such that to achieve desired power output, inherent stability and passive safety. Material selection was thoroughly refined in order to achieve prolonged structural durability, low cost of manufacturing, low cost of fuel and ease of maintenance. The core design specifications of the of the IMSR-400 are summarized in table 1.2. More information about the current status of the IMSR-400 can be found on the International Atomic Energy Agency (IAEA)'s Advanced Reactors Information System (ARIS) website [Terrestrial Energy In, 2016b].

1.4 Overview of the MSRE

1.4.1 History

Evaluation of the liquid fuel fluoride salt reactor with thorium fuel cycle took place between 1957 and 1960. The implementation of a thorium fuel cycle for thermal breeding was motivated by the need to conserve uranium resources as lesser uranium reserves were known back then. By mid 1960, promising results prompted the US Atomic Agency to authorize the Oak Ridge National Laboratory (ORNL) to begin the design and construction of the

Molten Salt Reactor Experiment (MSRE). The primary goal of the MSRE was to demonstrate the feasibility of building a commercial scale thermal breeder molten salt reactor with thorium fuel cycle. Exiting facilities from the Aircraft Nuclear Propulsion (ANP) program were used as basis for the design of the MSRE. Assembly of reactor components began in mid 1962, and first criticality was achieved on June 1st 1965. Zero-power operations lasted about a month, followed by final preparations. Power operations (up to 10 MWth) began in early 1966 and ended by early 1968 with 75% capacity factor. Nuclear characteristics portrayed in the experimental results of the MSRE were found to be in agreement with the theoretical predictions to a high degree. No structural change or compromising levels of corrosion were observed in critical reactor system components after 13000 hours of full power operation. Dynamic stability of the reactor system were demonstrated at different power levels and core configurations. Therefore, the ORNL concluded the feasibly of a large scale molten salt reactor [ORNL, 1969].

1.4.2 Experimental Setup

The MSRE reactor core is a cylindrical vessel made of hastelloy (INOR-8), a nickel based alloy, containing molybdenum, chromium and iron, characterized by high corrosion resistance in both aerated and molten fluoride salt environments at elevated temperatures up to 820 °C. The fuel salt mixture, used in the MSRE, have the following molar composition:

- 65% lithium fluoride (LiF)
- 29.2% beryllium difluoride (BeF_2)
- 5% zirconium tetrafluoride (ZrF_4)
- 0.8% uranium tetrafluoride (UF_4)

The reactor vessel is 1.5 m in diameter and 2.4 m in height, but the active core is 1.4 m in diameter and 1.6 m in height. Inside the reactor vessel, there are 513 vertical graphite stringers, horizontally arranged in a rectangular lattice with 5.08 cm pitch distance. The fuel salt passage through the graphite stringers have a rounded rectangular cross section as shown in figure 1.3.

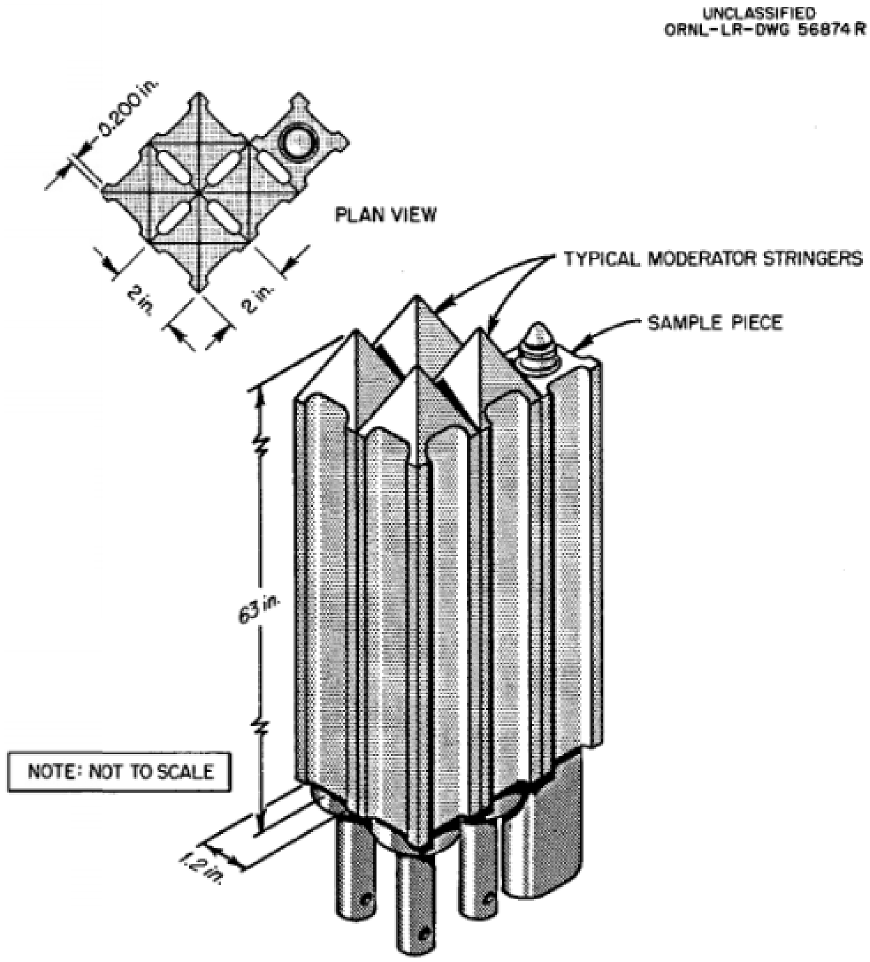

Figure 1.3: Top and side of view of MSRE's graphite stringers, containing fuel channels.

Each graphite stringer on its own forms four half-channels. Hence, full-channels are formed when graphite stringers are interlocked side by side. The top section of the graphite stringer is tapered in order to prevent salt pooling after draining the reactor. Three control rods and a single sample holder vertically penetrate the reactor vessel from the top. The four central graphite stringers contain cylindrical thimbles, providing an entry passage for the control rods and the sample holder. The fuel salt inlet pipe is connected to a flow distribution ring, located at the top of the reactor vessel. From the inlet pipe and through the flow distributor, the fuel salt flows downward, filling the bottom plenum. From the bottom plenum, the fuel salt flows upward through the fuel salt channels, formed by the vertically interlocked graphite stringers. The fuel salt then fills the top plenum, and exits the reactor vessel through an outlet pipe. A sump-type centrifugal pump siphons the fuel salt from the outlet pipe through the pump bowl to the shell and tube primary heat exchanger. Two systems are connected to the pump bowl, each performs a unique function: helium off-gas system and sampler enricher system. The helium off-gas system injects helium gas at a rate of 4 L/min through a bubbler tube, purging gaseous fission products such as xenon and krypton from the fuel salt. The sampler enricher system serves two functions: chemistry control and increasing uranium enrichment in the fuel salt. Ten gram sample at a time is drawn from the pump bowl to a two-compartment dry box for lab analysis. Samples are analyzed for composition, corrosion products and abnormal oxidation. $UF_4 - LiF$ filled capsules (93% enriched uranium) is added to the pump bowl to achieve desired fuel enrichment. Beryllium metal is occasionally added to the pump bowl to balance the U^{4+} to U^{3+} ratio. Finally, the fuel salt flows through the primary heat exchanger and back to the reactor. Depending on the operational power mode of the MSRE (zero-power, or power operations), the primary heat exchanger serves as a heat sink, or a source of heat for the fuel salt.

The coolant salt mixture, composed of LiF and BeF_2 salts only, is used to remove/add heat from/to the fuel salt through the primary heat exchanger. A shell and tube air radiator, enclosed by a furnace system, is used to either remove heat from the coolant salt by forced air flow, or add heat via electric heaters inside the furnace. The furnace has a door that can slide upward or downward, used to control the intake of cooling air. Hot air exits the furnace through a stack to outside the building. Furnace doors can be quickly closed in order to prevent sudden freezing of the coolant salt. After removing/adding heat from/to the coolant salt, a sump-type centrifugal pump is used to siphon the coolant salt from the outlet of the radiator back to the primary heat exchanger. The following schematic summarizes the MSRE setup and the process readily described:

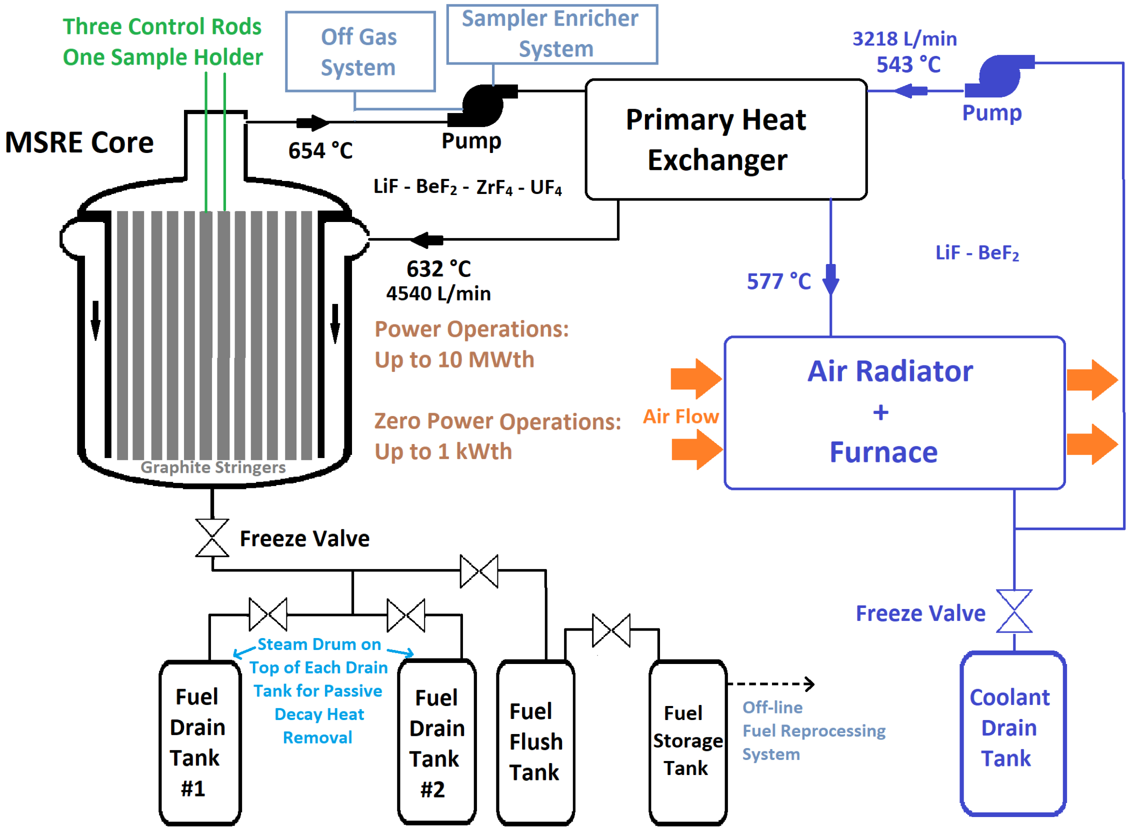

Figure 1.4: MSRE reactor system schematic.

As shown in figure 1.4, fuel salt and coolant salt inventories in the primary and secondary loops respectively are controlled via freeze valves. A freeze valve is made of a short plug of salt, maintained in the solid state by a cooling gas system. The primary loop is connected via freeze valves to two fuel drain tanks, a fuel flush tank and a fuel storage tank. One fuel drain tank is capable of taking the entire fuel salt inventory in non-critical conditions. The fuel drain tanks are equipped with passive water-steam cooling system capable of handling decay heat in the fuel salt after shutdown. The fuel flush tank contain non-fissile salt mixture used to wash the circulation system after shutdown. The fuel storage tank diverts fuel salt flow from the drain tanks and stores it. Fuel salt in the fuel storage tank can be directed toward an off-line fuel reprocessing system. The secondary loop is connected via freeze valves to the coolant drain tank, which serves the same function as the fuel drain tank, except having a decay heat cooling system since the coolant salt does not contain any fissile material, hence, it generates no heat.

1.4.3 Zero-Power Experiments

Initial criticality experiments with the MSRE were performed at low power levels (i.e. zero-power: 1 - 1000 W). The purpose of these experiments was to establish the nuclear characteristics of the MSRE system and validate calculation techniques and models previously developed. Several test were performed to determine uranium-235 criticality loading for different control rods configurations, calibrate control rods, determine reactivity loss due to circulation, determine different reactivity feedback coefficients and study the reactor system's dynamic performance [Prince *et al.*, 1968].

At the start, fuel salt, containing depleted uranium only, was loaded into the core. Then, the fuel salt was circulated in the system at 650 °C for ten days while analyzing 18 samples in order to verify the initial composition. Criticality approach was performed by adding frozen $73\% LiF - 27\% UF_4$ salt capsules, containing 85 grams of uranium-235 (93% enriched uranium). A $^{241}Am -^{242} Cm - Be$ neutron source was used during subcriticality. Additional neutrons are generated within the fuel salt due to interactions between alpha particles from U-234 and beryllium and fluorine nuclides. The fuel salt internal neutron generation rate was found to be 3-5% with respect to the yield of the external neutron source. The flux monitoring instrumentation consisted of two fission chambers and two BF_3 gas chambers. As enriched fuel salt capsules were added one at a time into the pump bowl, the increase in multiplication was determined for each detector. The minimum uranium-235 criticality loading was determined to be at 69.6 kg of uranium-235. By consecutively adding enriched fuel salt capsules while inserting the control rods, reactivity worth of control rods were measured for different rods configurations. Control rods differential and integral worth values were calculated by stable period measurements and rod-drop experiments. Sufficient excess reactivity was added to the core such that transient behavior would closely resemble full power conditions [Prince *et al.*, 1968]. Various reactivity feedbacks such as pressure, temperature and uranium-235 loading reactivity feedbacks were measured using the readily calibrated control rods. The reactivity and the delayed neutron fraction losses due to fuel circulation were also measured. Measurements of various parameters were conducted for both static and circulating fuel salt.

1.5 IMSR-400 Subcritical Test

Analysis has shown that the IMSR-400 is expected have a largely negative overall temperature-reactivity coefficient (α_T), induced by inherent neutronic properties of the core in terms of material and core design parameters. The α_T is sufficiently negative such that control rods are not needed to maintain the reactor power. Previous MSRE, conducted by ORNL, have readily demonstrated the self-regulation effect from utilizing the combination of molten salt fuel and a graphite moderator. However, the MSRE's results can not be used as an experimental validation of the IMSR-400's analysis since the IMSR-400's design differs from the MSRE design in terms of the core configuration and the fuel salt mixture, therefore, having different inherent neutronic properties. Additionally, different thermophysical properties such as density, melting temperature, thermal expansion coefficient and viscosity are associated with different fuel salt mixtures. The α_T associated with fuel salt expansion accounts for more than 20% of the total α_T. Moreover, the α_T associated with the graphite moderator is determined by the fuel-to-moderator ratio, which influences the degree of core moderation. Therefore, a unique physics test of the IMSR-400 concept must be conducted in order to properly validate the results of the IMSR-400's analysis. Furthermore, building a critical test facility would be costly. For this reason, building a subcritical test facility was considered as an option. The main objective of this thesis is to determine the feasibility of conducting an IMSR-400 subcritical physics test, using a subcritical scaled-down version of the IMSR-400 design. The IMSR-400's subcritical pile would closely resemble the primary design features of the IMSR-400, such as the pitch distance, the active core height-to-diameter ratio and the material composition. The primary tests to be performed using the subcritical pile can be outlined as follow:

1. Constant source test to measure the temperature-reactivity coefficient.

2. Pulsed source test to measure the delayed neutron fraction and the prompt generation time.

Although a subcritical physics test is not expected to predict the exact α_T values of the IMSR-400 core, the purpose is to demonstrate the negative values of α_T. Furthermore, establishing appropriate procedures and methods to measure the delayed neutron fraction would be useful for future physics tests to measure the delayed neutron fraction loss due to circulation of the fuel salt.

Since the fuel salt mixture formula and the specific core design parameters of the IMSR-400 are proprietary information (protected by a non-disclosure agreement) design alterations were made and a different fuel salt mixture was used in the published analysis (see section 4.3). However, the results were still representative of the trends and patterns, obtained from analyzing the real IMSR-400's subcritical test.

Chapter 2

Reactor Physics Theory

2.1 Nuclear Stability

Physical properties of different elements is determined mainly by the number of protons in the nuclear valence (i.e. atomic number). Nuclear stability, however, is determined by the number of neutrons in the nuclear valence. Neutrons act as nuclear glue by canceling the electric repulsion forces between positively charged protons in the nucleus. For atomic numbers greater than 20, more neutrons than protons are needed to maintain stability [Lamarsh and Baratta, 2001, p. 18]. Nuclides that share the same atomic number, but differ in the number of neutrons are called isotopes. Isotopes of the same element, could either be stable or radioactive based on the ratio of the number of protons to the number of neutrons. Stable and radioactive isotopes alike could exist naturally, but some are artificial. All known isotopes and their respective stability are presented in the Segré chart (or the chart of nuclides), which is a more detailed version of the periodic table:

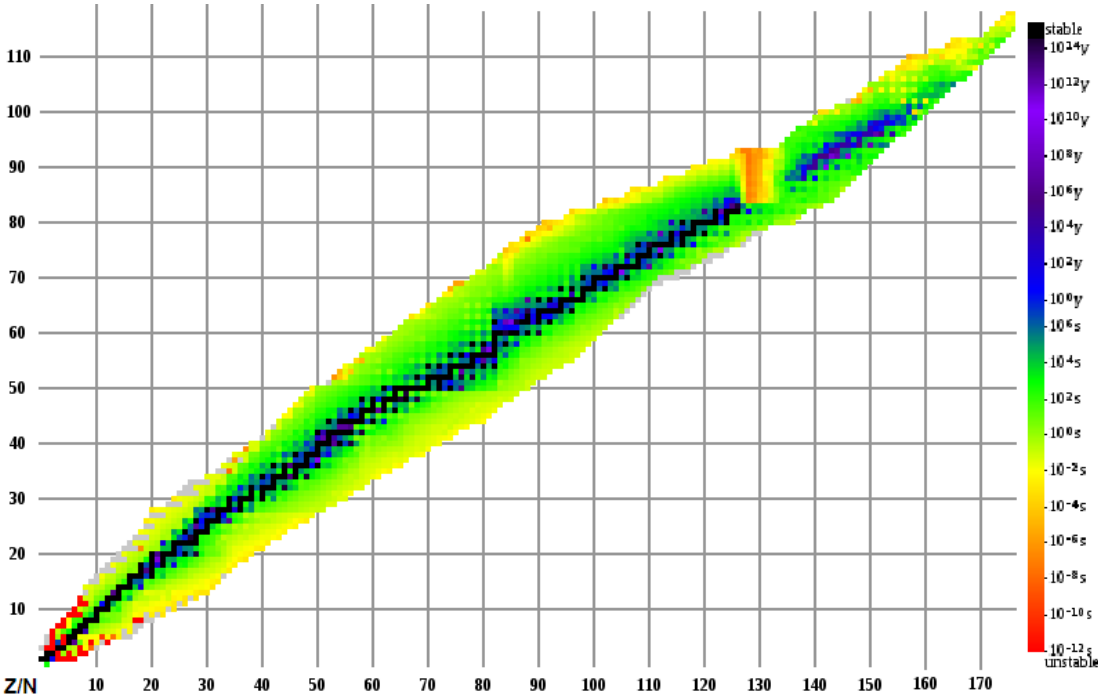

Figure 2.1: Segre chart or the chart of nuclides.

The region outside the colored region is known as the "sea of instability" where it is impossible for isotopes to exist based on the current understanding of physics. For the same atomic number, there could be one or more stable isotope. However, if the proton-to-neutron ratio is outside the optimal range, the nuclide is radioactive. Heavy nuclides (Z $>$ 90) are an exception since no stable isotopes are known currently. Common decay modes of radioactive nuclides are:

Table 2.1: Common modes of radioactive decay in nature.

Decay mode	Definition	Reaction Equation
Alpha decay	Emission of helium-4 nucleus	${}^{A}_{Z}X \rightarrow {}^{4}_{2}He + {}^{A-4}_{Z-2}Y$
Beta-minus decay	Emission of electron	${}^{A}_{Z}X \rightarrow {}^{0}_{-1}e + {}^{A}_{Z+1}Y$
Gamma ray emission	Emission of photon	${}^{A}_{Z}X \rightarrow {}^{0}_{0}\gamma + {}^{A}_{Z}Y$
Beta-plus decay	Emission of anti-electron	${}^{A}_{Z}X \rightarrow {}^{0}_{1}e + {}^{A}_{Z-1}Y$
Electron capture	Electron fall from orbit into nucleus	${}^{A}_{Z}X + {}^{0}_{-1}e \rightarrow {}^{A}_{Z-1}Y$

Radioactive nuclides do not decay instantly upon formation. Instead, the decay of a parent nuclide into a daughter nuclide is governed by an exponential decay probability function. In a bulk matter made of the parent nuclide, the time it takes for half of all parent nuclides to decay into daughter nuclides is known as the half-life ($T_{1/2}$). The general equation describing parent-to-daughter radioactive decay is as follow:

$$N_p(t) = N_{p0}\ e^{\frac{-\ln 2}{T_{1/2}} t} = N_{p0}\ e^{-\lambda t}, \tag{2.1}$$

where N_p is the concentration of parent nuclides as a function of time t, N_{p0} is the initial concentration of parent nuclides, and λ is the decay constant. It is possible that the daughter nuclide is also radioactive. Uranium-238, for example, goes through 14 steps of radioactive decay until lead-206 (stable) is reached. Such phenomenon is described as ”decay chain”.

Different versions of the Segre chart may also show the average binding energy between nucleons (i.e. protons and neutrons). Nuclei with low binding energy are less tightly bound than nuclei with high binding energy. This has less to do with nuclear stability and more to do with energetic favourability of the nuclear configuration. Both light elements (Z $<$ 20) and heavy elements (Z $>$ 90) tend to have relatively lower binding energy between nucleons. Consequently, light elements are fusible (forming heavier atoms) and heavy element are fissionable (forming lighter atoms). Either fusion or fission reactions can be exothermic only if the net binding energy of the products is larger than the net binding energy of the reactants, hence, endothermic if the opposite is true.

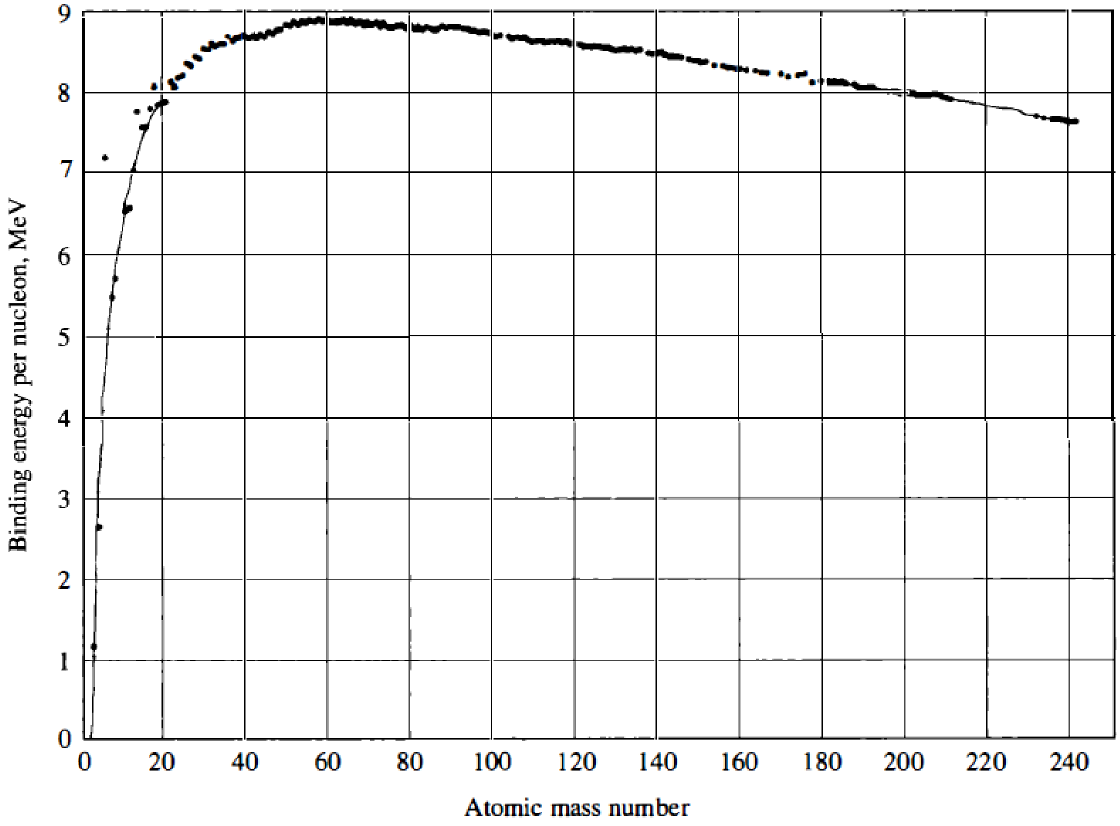

Figure 2.2: Average binding energy per nucleon profile with respect to the atomic mass.

2.2 Neutron Interaction with Matter

A neutrons is a subatomic particle, slightly more massive than a proton, made of one up-quark and two down-quarks, classified both as brayon and hadron particle. Free neutrons are unstable and decay into a protons, releasing an anti-neutrino and a beta-minus particle with a mean lifetime of 15 minutes. Due to its elementary particle composition, a neutron exhibits neutral electric charge and measurable magnetic momentum, hence, influenced by magnetic fields but not by electric fields [Adair, 1987]. The electric charge neutrality enable neutrons to interact directly with atoms' nuclei in one of the following ways:

Table 2.2: Common modes of interaction between neutrons and nuclei.

Interaction mode	Description	Reaction Equation
Elastic Scattering	The nucleus is left at ground-state after collision. Incident neutron retain its kinetic energy	${}^{A}_{Z}X + {}^{1}_{0}n \rightarrow {}^{A}_{Z}X + {}^{1}_{0}n$
Inelastic Scattering	The nucleus is left at excited state after collision. Incident neutron looses some of its kinetic energy. Excited nucleus undergoes γ decay later	${}^{A}_{Z}X + {}^{1}_{0}n \rightarrow {}^{A}_{Z}X^{*} + {}^{1}_{0}n^{*}$
Radiative Capture	Neutron absorption forms a compound nucleus at excited state, releasing γ ray instantly	${}^{A}_{Z}X + {}^{1}_{0}n \rightarrow {}^{A+1}_{Z}Y + {}^{0}_{0}\gamma$
Charged-Particle Reactions	Neutron absorption leads to consecutive release of a positively charged particle (e.g. proton, alpha, etc.)	${}^{A}_{Z}X + {}^{1}_{0}n \rightarrow {}^{A-M}_{Z-N}Y + {}^{M}_{N}S$
Neutron-Producing Reactions	Collision leads to release of two or more neutrons. It can be classified as a type of inelastic scattering	${}^{A}_{Z}X + {}^{1}_{0}n \rightarrow {}^{A-x}_{Z}Y + x{}^{1}_{0}n$
Fission	Neutron absorption leads to splitting of the nucleus and release of two to three neutrons	${}^{A}_{Z}X + {}^{1}_{0}n \rightarrow {}^{M}_{N}Y + {}^{G}_{H}S + x{}^{1}_{0}n$

Neutron interaction with matter is a stochastic event. The probability that a neutron will interact with a nucleus through one interaction mode or another is described as the microscopic cross section (σ). That is the mathematical meaning of σ. The physical meaning of σ describes the effective two-dimensional area of the nucleus in barns ($10^{-24}cm^2$) as seen by an incident neutron. The total microscopic cross section (σ_t), lumping together all possible interaction modes, can be described as the sum of scattering (σ_s) and absorption (σ_a) microscopic cross sections:

$$\sigma_t = \sigma_a + \sigma_s \tag{2.2}$$

$$\sigma_a = \sigma_\gamma + \sigma_f + \sigma_p + \sigma_\alpha + ...$$

$$\sigma_s = \sigma_e + \sigma_i + ...$$

σ_a includes all interactions involving initial neutron absorption such as radiative capture (σ_γ), fission (σ_f), proton emission (σ_p), alpha emission (σ_α), etc. σ_s includes elastic (σ_e) and inelastic (σ_p) scatterings.

By scaling up the system into a beam of neutrons and a bulk material target, the frequency of interactions (i.e. reaction rate or beam attenuation rate) can be described by the following equations:

$$F = \sigma N I, \tag{2.3}$$

$$N = \frac{\rho N_A}{M},$$

$$I = \mathrm{n}v,$$

where N is the atomic density of the material ($atom\ cm^{-3}$), I is the intensity of the neutron beam ($n\ cm^{-2}\ s^{-1}$), ρ is the mass density of the material ($g\ cm^{-3}$), N_A is the Avogadro number ($6.022 \times 10^{23}\ mol^{-1}$), M is the molar mass of the material ($g\ mol^{-1}$), n is the neutron density ($n\ cm^{-3}$) and v is the average neutron speed ($cm\ s^{-1}$). The degree to which the neutron beam is attenuated by a specific thickness of target material, can be determined by integrating equation (2.3) with respect to distance (x):

$$\int F\ dx = \int \frac{dI}{dx} dx = I_0\ e^{-\sigma N x} = I_0\ e^{-\Sigma x} \tag{2.4}$$

Σ is known as the attenuation coefficient, or the macroscopic cross section. The standard unit of Σ is cm^{-1}. The total macroscopic cross section (Σ_t) is defined as the sum of absorption (Σ_a) and scattering (Σ_s) macroscopic cross sections:

$$\Sigma_t = \Sigma_a + \Sigma_s = \sigma_a N + \sigma_s N \tag{2.5}$$

If the target material is a mix of two or more isotopes, say X and Y, then:

$$\Sigma = \Sigma_X + \Sigma_Y = \sigma_X N_X + \sigma_Y N_Y \tag{2.6}$$

Assuming the target material is subjected to multiple mono-energetic beams (i.e. same neutron velocity), coming from different directions, then equation (2.3) can be rewritten as follow:

$$F = \Sigma(I_A + I_B + I_C + ...) = \Sigma(n_A + n_B + n_C + ...)v = \Sigma\phi \tag{2.7}$$

Where ϕ in the sum of beam intensities from all directions, described as the neutron flux, and shares the same unit as I.

The magnitude of the neutron cross section is dependant on the the kinetic energy of incident neutrons and inherent properties of the target nucleus. Except for low neutron energy scattering, in most interaction modes, the reaction proceeds in two-steps: 1) forming an unstable compound nucleus with the incident neutron, then 2) decay by emitting elastic/inelastic neutron, γ ray, α particle, proton, etc., or even by fissioning. Whether or not a compound nucleus is formed is determined by available excitation energy states. cross section profiles of interactions modes involving formation of compound nucleus exhibit some maxima corresponding to certain neutron energies. These maxima are known as resonance regions where the cross section is relatively higher.

2.3 Neutron Transport Equation

Neutron migration through a medium and interaction with matter within the medium can be mathematically described by the Boltzmann equation, also known as the neutron transport equation:

$$\frac{1}{v(E)}\frac{\partial}{\partial t}\Psi(r,E,\hat{\Omega},t) + \Sigma_t(r,E,t)\Psi(r,E,\hat{\Omega},t) + \hat{\Omega}\cdot\nabla\Psi(r,E,\hat{\Omega},t) \tag{2.8}$$

$$= \int_0^{\infty} dE^{'} \int_0^{4\pi} d\hat{\Omega}^{'}\Sigma_s(r,E^{'}\rightarrow E,\hat{\Omega}^{'}\cdot\hat{\Omega})\Psi(r,E^{'},\hat{\Omega}^{'},t) + s(r,E,\hat{\Omega},t)$$

$$+\frac{\chi_p(E)}{4\pi}\int_0^{\infty} dE^{'}\upsilon_p(E^{'})\Sigma_f(r,E^{'})\phi(r,E^{'},t) + \sum_{i=1}^{N}\frac{\chi_{di}(E)}{4\pi}\lambda_i C_i(r,t)$$

The description of parameters and terms in the Boltzmann equation is provided in tables 2.3 and 2.4.

Table 2.3: Brief description of parameters in the Boltzmann equation.

r	Position in polar coordinates	E	Final energy
$\hat{\Omega}$	Final solid angle	v	Neutron velocity
t	Time	Ψ	Angular flux
ϕ	Angle-integrated flux	υ_p	Average prompt neutrons yield per fission
χ_p	Probability density function of the prompt neutron spectrum	χ_{di}	Probability density function of the delayed neutron spectrum for a delayed neutron precursor i
Σ_t	Total macroscopic cross section	Σ_f	Fission macroscopic cross section
Σ_s	Scattering macroscopic cross section	N	Total number of delayed neutron precursors
λ_i	Decay constant of delayed neutron precursor i	C_i	Concentration of a delayed neutron precursor i
$\hat{\Omega}'$	Initial solid angle after scattering	$E^{'}$	Initial energy after scattering

Table 2.4: Brief description of terms in the Boltzmann equation.

Term	Description
$\frac{1}{v(E)}\frac{\partial}{\partial t}\Psi(r,E,\hat{\Omega},t)$	Neutron rate of change
$\Sigma_t(r,E,t)\Psi(r,E,\hat{\Omega},t)$	Total reaction rate
$\hat{\Omega}\cdot\nabla\Psi(r,E,\hat{\Omega},t)$	Neutron leakage rate
$\int_0^\infty dE^{'}\int_0^{4\pi} d\hat{\Omega}^{'}\Sigma_s(r,E^{'}\rightarrow E,\hat{\Omega}^{'}\cdot\hat{\Omega})\Psi(r,E^{'},\hat{\Omega}^{'},t)$	Down-scattering reaction rate
$s(r,E,\hat{\Omega},t)$	Neutron source rate
$\frac{\chi_p(E)}{4\pi}\int_0^\infty dE^{'}\upsilon_p(E^{'})\Sigma_f(r,E^{'})\phi(r,E^{'},t)$	Prompt neutrons generation rate
$\sum_{i=1}^{N}\frac{\chi_{di}(E)}{4\pi}\lambda_i C_i(r,t)$	Delayed neutrons generation rate

Notice in equation (2.8), the fission neutron yield is divided into two parts, prompt neutron yield (υ_p) and delayed neutron yield (υ_d). The Greek letter ”υ” describes the total neutron yield, prompt and delayed, per fission event.

$$\upsilon = \upsilon_p + \upsilon_d \tag{2.9}$$

Prompt neutrons are released instantly after fission, whereas delayed neutrons are produced via radioactive decay of some fission products such as bromine-87 and cesium-142, known as delayed neutron precursors. For simplicity, precursors with similar half life and neutron energy are often lumped together into groups. It is common in neutronic calculations to use six precursor groups.

$$\upsilon_d = \beta\ \upsilon = \sum_{i=1}^{N} \beta_i\ \upsilon \tag{2.10}$$

Where N is the number of precursor groups, β is the total delayed neutron fraction and β_i is the delayed neutron fraction associated with i precursor group. The energies of prompt neutrons are around 1 MeV (see figure 2.3), whereas the energies of delayed neutrons are in the order of a few hundreds keV (see table 2.5).

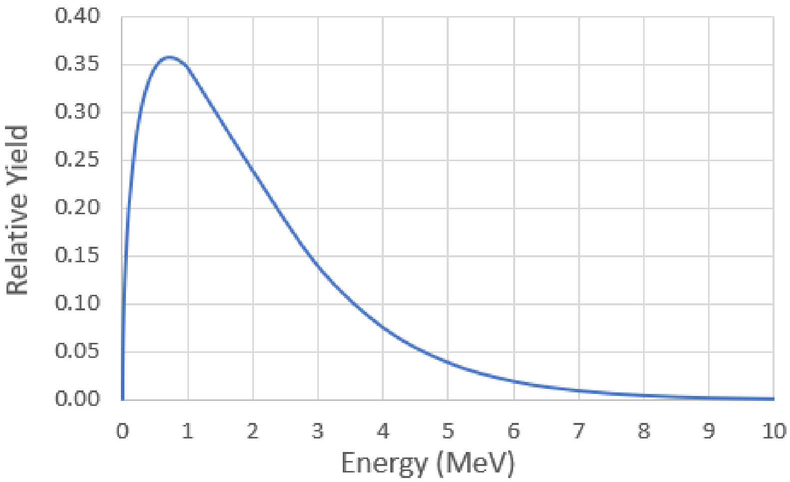

Figure 2.3: Common prompt neutron spectrum, approximated by the Watt distribution.

Table 2.5: Six delayed neutron group structure yield and energy for uranium-235, plutonium-239 and uranium-233 fissile isotopes.

i	Precursor	E_{avg} (MeV)	$T_{1/2}$			$\beta_i(\%)$		
			^{235}U	^{239}Pu	^{233}U	^{235}U	^{239}Pu	^{233}U
1	^{87}Br, ^{142}Cs	0.25	55.72	54.28	55.0	0.021	0.0072	0.0226
2	^{137}I, ^{88}Br	0.56	22.72	23.4	20.57	0.140	0.0626	0.0786
3	^{138}I, ^{89}Br, ^{93,94}Rb	0.43	6.22	5.60	5.00	0.126	0.0444	0.0658
4	^{139}I, ^{134}Xe, ^{93,94}Kr, ^{90,92}Br	0.62	2.3	2.13	2.13	0.252	0.0685	0.0730
5	^{140}I, ^{145}Cs	0.42	0.61	0.618	0.615	0.074	0.018	0.0135
6	Br, Rb, As, etc.	-	0.23	0.257	0.277	0.027	0.0093	0.0087
Total						0.64	0.21	0.26

When applying the Boltzmann equation to a reactor operating in steady-state (flux and cross section do not vary with time) and without an external neutron source, it is possible to remove the first and fifth terms and join the prompt and delayed yields terms together:

$$\begin{gathered}\Sigma_t(r,E,t)\Psi(r,E,\hat{\Omega},t)+\hat{\Omega}\cdot\nabla\Psi(r,E,\hat{\Omega},t) \\ +\int_0^\infty dE^{'}\int_0^{4\pi}d\hat{\Omega}^{'}\Sigma_s(r,E^{'}\rightarrow E,\hat{\Omega}^{'}\cdot\hat{\Omega})\Psi(r,E^{'},\hat{\Omega}^{'},t) \\ +\frac{\chi(E)}{4\pi}\int_0^\infty dE^{'}\upsilon(E^{'})\Sigma_f(r,E^{'})\phi(r,E^{'},t)=0\end{gathered} \tag{2.11}$$

The new form of the Boltzmann equation is known as the time-independent linear Boltzmann equation. It is also homogeneous, meaning that there is a trivial solution to the neutron flux. Thus, by modifying the nuclear properties of the core, desired neutron flux (or power) can be achieved at criticality conditions (i.e. $k_{\text{eff}}=1$).

Even for the simplest problems, obtaining an analytical (i.e. deterministic) solution of the Boltzmann equation is difficult if not impossible [Garland, 2014]. This is mainly due to the fact that the Boltzmann equation is an integro-differential equation and has seven dimensions: three for spatial coordinates, two for angle, one for time and one for energy. Thus, solving the Boltzmann equation analytically requires low-order approximations such as the diffusion and grey approximations. The diffusion approximation eliminates angular dependence by integrating flux over the full range of the solid angle, based on the assumption that the fission cross section is independent from the direction of the incident neutron. Applying the grey approximation eliminates energy dependence by averaging cross sections over the entire energy spectrum. Depending on the application, such approximations may, or may not be sufficiently accurate. Another approach to solving the Boltzmann equation is by stochastic (i.e. probabilistic) solution methods, namely, Monte Carlo methods.

In the Monte Carlo simulation approach to solving the Boltzmann equation, several neutrons are generated in a random direction at a random position (unless mono-directional, or isotropic source is specified) while tracking the travel path and collision events associated with each neutron. The neutron flux in a certain region is estimated either by tracking path-lengths, or collision rates, using reaction probabilities. Reaction probabilities represent the possible outcomes of collision events, governed by the ratios between different macroscopic cross sections of the constituent materials. The scattering energy and direction of incident neutrons are used to predict the travel path and collision rates. The ratio between the total travel distance and the volume of the region is equivalent to the neutron flux. The ratio between the total collision rate and the total macroscopic cross section is also equivalent to the neutron flux. Statistical errors in the neutron flux predictions decay as a function of the inverse square-root of neutron histories (i.e. number of randomly generated neutrons), making Monte Carlo methods an attractive approach to solving the Boltzmann equation [Brown, 2016].

By nature, Monte Carol simulations are computation-intensive, hence, for practical reasons require the use of computer codes and large computational capabilities. Today, several Monte Carlo based computer codes are commonly used for reactor physics analysis such as:

- Monte Carlo Neutron-Particle Transport Code (MCNP), developed by Los Alamos

National Laboratory in the USA.

- TRIPOLI, developed by the Service d'Etudes des Réacteurs et de Mathématiques Appliquées (SERMA) in France.
- KENO, developed by Oak Ridge National Laboratory in the USA.
- SERPENT, developed by VTT Technical Research Centre of Finland.

The main underlying assumptions of Monte Carlo simulations are [Brown, 2016]:

- Neutrons behave as particles.
- Collisions occur instantaneously.
- Relativistic effects are neglected.
- Quantum effects are neglected.
- Material properties remain fixed during the simulation.

2.4 Temperature Reactivity Coefficient

The rate at which reactor power is increasing or decreasing in a transient, is governed by the degree of deviation from criticality. The deviation from criticality is described as reactivity (ρ).

$$\rho = 1 - \frac{1}{k_{\text{eff}}} \tag{2.12}$$

Controlling reactivity by external means can be achieved via control rods, chemical shimming, refueling, etc. Furthermore, the temperature of the fuel, coolant and moderator provide a reactivity feedback upon variation. The temperature reactivity coefficient (α_T), described as the change in reactivity due to the change in the temperature of materials in the core, is expressed by the following relation:

$$\alpha_T = \frac{d\rho}{dT} \approx \frac{\rho(T_2) - \rho(T_1)}{T_2 - T_1} \tag{2.13}$$

Where ρ is the reactivity and T is the temperature. A positive α_T indicates that an increase in average temperature would result in a positive change in reactivity, and vice-versa. A reactor is considered inherently unstably if the overall α_T is positive, or inherently stably if the overall α_T is negative. The overall α_T is approximately the sum of the fuel temperature-reactivity coefficient (α_{prompt}) and the moderator temperature-reactivity coefficient (α_{mod}). Mathematical representation of the contributing factors toward the magnitude and the signal of α_{prompt} and α_{mod} can be done based on the six-factors formula:

$$k_{\text{eff}} = \eta f p \epsilon P \tag{2.14}$$

Where k_{eff} is the effective multiplication factor, η is the reproduction factor, f is the thermal utilization factor, ϵ is the fast fission factor, p is the resonance escape probability and P is the non-leakage probability (thermal and fast). By taking the derivative of the log of both sides with respect to temperature, the following relation is obtained:

$$\frac{d}{dT}(\ln k_{\text{eff}}) = \frac{1}{\eta}\frac{d\eta}{dT} + \frac{1}{f}\frac{df}{dT} + \frac{1}{p}\frac{dp}{dT} + \frac{1}{\epsilon}\frac{d\epsilon}{dT} + \frac{1}{P}\frac{dP}{dT}. \tag{2.15}$$

In the context of the IMSR-400, it is apparent that neither change in temperature of the molten salt fuel nor the graphite moderator would have any significant impact on η since it is dependent on the fissile composition of the fuel and the neutron spectrum. Additionally, operating in the thermal spectrum means that ϵ would always be close to unity. Also, since the graphite absorption cross section is small (0.7 mb at 0.625 eV) and fuel salt ejection from the core due to thermal expansion occurs uniformly across the core, the change in f with respect to temperature is insignificant. Therefore, the α_T can be expressed as the sum of contributions from p and P:

$$\alpha_T = \alpha_T(p) + \alpha_T(P) \tag{2.16}$$

Considering first α_{mod}, (assume the core is under-moderated) slight spectrum hardening occurs when graphite temperature increases. Consequently, more neutrons are captured in uranium-238's resonances, hence, $\alpha_T(p)$ contribution would be negative. Moreover, $\alpha_T(p)$

might become slightly positive as Pu-239 builds-up in the fuel. Lastly, the contribution from $\alpha_T(P)$ is essentially zero since the change in graphite density with respect to temperature is small.

Considering next α_{prompt}, the Doppler broadening effect of uranium-238 resonances will increase resonance capture, hence, $\alpha_T(p)$ contribution would also be negative. Since the molten fuel salt undergoes thermal expansion, the reduction in the fissile density in the core will increase leakage, hence, the contribution from $\alpha_T(P)$ would be negative.

In light water cooled and moderated reactors the overall α_T is negative by design (unless there are excessive amounts of dissolved burnable poison). However, due to the small magnitude of α_T, it is impractical to solely relay on α_T for maintaining reactor power within the operational limits without any external means of reactivity controls. Liquid-fuel molten salt reactors (LF-MSR), on the other hand, have a largely negative α_T, significantly reducing reliance on external reactivity mechanisms for power control. Such largely negative α_T is achieved mainly with the use of liquid fuel coolant and a graphite moderator. Liquid fuel coolants when heated, the thermal expansion effect would reduce the fissile density in the core, leading to a negative reactivity insertion in addition to the Doppler effect. Heating graphite reduces its neutron thermalization efficiency, leading to a negative reactivity insertion.

Chapter 3

Reactivity Measurement Methods

In a subcritical setting, reactivity measurement is typically useful for the measurement of criticality approach, reactivity feedbacks, reactivity worth of reactivity control instruments, reactor kinetics parameters such as the delayed neutron fraction (β) and the neutron prompt generation time (Λ), etc. For the purpose of this thesis, the interest is mainly in the determination of α_T, which is calculated using equation (3.1) once reactivity is determined at two temperature points, T_1 and T_2:

$$\alpha_T = \frac{\rho_2(T_2) - \rho_1(T_1)}{T_2 - T_1} \tag{3.1}$$

Three reactivity measurement methods are described in this section:

1. The subcritical multiplication method (SM);
2. Sjöstrand area method (SA), and
3. The slope fit method (SF).

3.1 Subcritical Multiplication Method

For a neutron traveling through a subcritical system, the number of neutrons generated due to fission after one prompt generation time increment is described by the following relation:

$$n(t+\Lambda) = k_{\text{eff}} n(t) \tag{3.2}$$

Where $n(t)$ is the measured neutron signal at time t, $n(t+\Lambda)$ is the measured neutron signal after one prompt generation time Λ. The subcritical multiplication factor M, representing the ratio between the initial and the convergence neutron signals, can be computed as follow:

$$M = \sum_{i=1}^{\infty} k_{\text{eff}}^{i} = \frac{1}{1-k_{\text{eff}}} \tag{3.3}$$

Similarly, when applying a constant neutron flux to the subcritical pile, using an external neutron source, the measured steady-state neutron signal n_{meas} is the product of the measured source rate $\dot{S}$ and the subcritical multiplication factor M:

$$n_{meas} = \frac{1}{1-k_{\text{eff}}}\dot{S} = M\dot{S} \tag{3.4}$$

As it is difficult to measure the source rate and the total neutron signal independently, it is possible to eliminate $\dot{S}$ by dividing $n_{\text{meas}}(T_1)$ by $n_{\text{meas}}(T_2)$, where T_1 and T_2 are two unique temperature points of the subcritical pile:

$$\frac{n_{\text{meas}}(T_1)}{n_{\text{meas}}(T_2)} = \frac{M(T_1)}{M(T_2)} = \frac{1-k_{\text{eff}}(T_2)}{1-k_{\text{eff}}(T_1)} \tag{3.5}$$

Therefore, if $k_{\text{eff}}(T_1)$, $n_{\text{meas}}(T_1)$ and $n_{\text{meas}}(T_2)$ are known (by experiment or simulation), it would be possible to determine $k_{\text{eff}}(T_2)$.

The main underlying assumption of the SM method is spatial independence, meaning that flux shape is assumed to not vary significantly with each reactivity insertion. Thus, any localized reactivity insertion (e.g. control rods) will reduce the accuracy of the SM method. Moreover, by ensuring that a uniform temperature distribution of fuel salt and graphite is reached during the heating process before beginning to take measurements will hold the validity of the assumption of spatial independence.

3.2 Slope Fit Method

When a neutron pulse is injected into a subcritical system and fission occurs, prompt neutrons are generated, which in turn cause more fission, leading to a rapid rise in the neutron population. Due to subcriticality, the fission chain reaction is not self-sustained since the rate of neutron loss via parasitic absorption and leakage is larger than the rate of neutron production via fission. Hence, within less than a millisecond, the rate of prompt neutron production reaches a maximum, then exponentially decays to zero. By repeatedly injecting neutron pulses at a constant frequency, the concentration of delayed neutron precursors gradually builds up and reaches an equilibrium. A stable delayed neutron background level is established once the subcritical pile is saturated with delayed neutron precursors. Consecutive injection of neutron pulses, yields similar behavior, except this time, the neutron population decays to the equilibrium delayed neutron background level (see figure 3.1). The time period when the neutron population rises rapidly and then reaches a maximum is described as the injection and adjustment period. The exponential decay of the neutron population to delayed neutron background level is described as the fundamental decay mode. According to Persson *et al.* [2005], three exponential terms and a constant are sufficient to provide a complete mathematical representation of the pulse behavior: two exponential terms for the injection and adjustment period, one exponential term for the fundamental decay mode, and finally, a constant for the equilibrium delayed neutron background level. Moreover, the fundamental decay mode can be described by the solution of the point kinetic equation with no delayed neutrons:

$$n(t) = n_0 \exp\left(\alpha t\right) = n_0 \exp\left(\frac{\rho - \beta}{\Lambda} t\right) \tag{3.6}$$

where n_0 is the peak neutron signal, α is the prompt decay constant, ρ is reactivity, β is the delayed neutron fraction, and Λ is the prompt generation time. Excluding pulse profiles prior to reaching delayed neutron background equilibrium, a sufficiently large number of pulse profiles can be added by superimposition in order to improve accuracy. The magnitude of the prompt decay constant can be obtained by fitting the average pulse profile, excluding the injection and adjustment period and the decay to background parts. By determining ρ, via SM method, then β via SA method, it would be possible to determine Λ using the SF method.

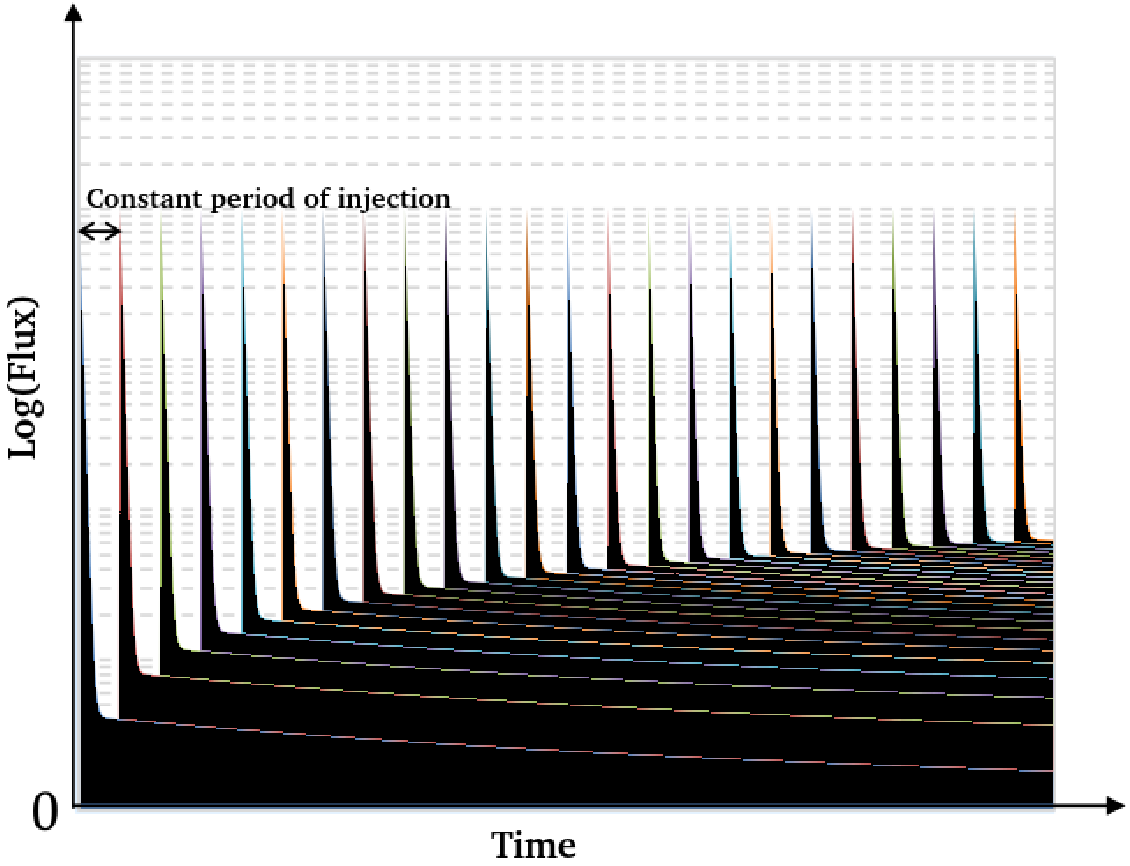

Figure 3.1: Simplified neutron flux behavior with respect to time as a result of repetitive injection of neutron pulses at a constant frequency.

3.3 Sjöstrand Area Method

Similar to the SF method, the SA method requires pulsed neutron source operation. Reactivity in dollar (i.e. $\frac{\rho}{\beta}$) can be measured by dividing the prompt response area (A_p) by the delayed response area (A_d) Persson *et al.* [2005].

$$-\frac{\rho}{\beta} = \frac{A_p}{A_d} \tag{3.7}$$

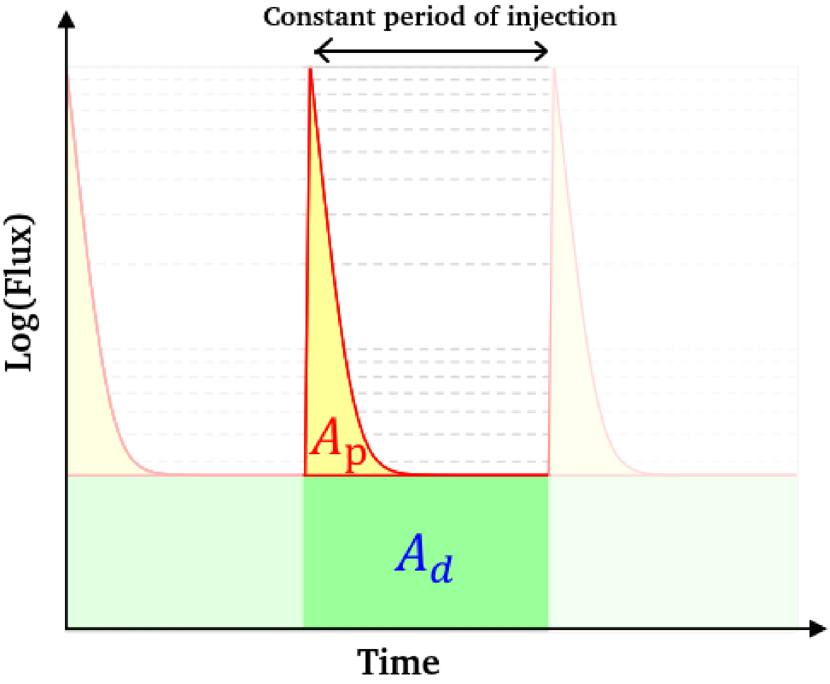

Figure 3.2: Simplified graphical representation of the prompt response area (A_p) and the delayed response area (A_d) [Endo and Yamamoto, 2015].

3.4 Comparison

Notice that the SA method takes into account delayed neutrons, whereas the SF and the SM methods do not. The assumption of no delayed neutrons is valid for the SF and the SM methods since the change in the prompt signal is independent from the delayed signal. Nonetheless, the accuracy of the SA method is more influenced by the position of the neutron detector than the SM and the SF methods since the energy of delayed neutrons is in the order of a few hundreds keV, hence, they have a shorter mean free path than prompt neutrons. Section 4.6 goes through different selection criteria and analysis performed in order to determine suitable locations for in-core flux detectors. The following table provides a summary of the three reactivity measurement methods:

Table 3.1: Brief summary of comparison between reactivity measurement methods.

Method	Source Operation Mode	Assumptions	Equation
Subcritical Multiplication	Constant	Spatial independence No delayed neutrons	$k(T_2) = 1 - (1 - k(T_1))\frac{n(T_2)}{n(T_1)}$
Slope Fit	Pulsed	Spatial independence No delayed neutrons	$\alpha = \frac{\rho - \beta}{\Lambda}$
Sjöstrand	Pulsed	Spatial independence	$-\frac{\rho}{\beta} = \frac{A_p}{A_d}$

Chapter 4

Experiment Design Process

4.1 Design Requirements

The preliminary design requirements of the IMSR-400's subcritical pile are as follow [Robinson, 2016]:

- The k_{eff} must not exceed 0.95 at any given temperature, or for any change in configuration.
- The fuel salt channel diameter must be that of the IMSR-400's core.
- The fuel salt mixture must be that of the IMSR-400's core.
- Fuel channels must be ordered in a triangular lattice.
- The pitch distance must be that of the IMSR-400's core.
- The operational temperature range must be between 300 and 1000 K.
- Fuel enrichment must be between 2.00 to 4.95%.
- Graphite must be the primary mean of neutron moderation.

As mentioned in section 1.5, due to Intellectual Property (IP) restrictions, a different salt mixture formula was used in the published analysis. The salt mixture consist of sodium fluoride, beryllium fluoride and uranium tetrafluoride ($NaF - BeF_2 - UF_4$). Additionally, analysis were performed for an operational temperature range of 750 to 1000 K based on available liquid salt density data.

4.2 Regulatory Compliance

As per Class I Nuclear Facilities Regulations (SOR/2000-204), the design for this experiment is classified as a Class IA nuclear facility. There are various nuclear facilities that belong under this class with varying levels of design characteristics, risks and hazards associated with each. For the subcritical pile design, the safety standards governing criticality safety will be applied with a graded approach. This means that the levels of analysis, the depth of documentation and the scope of actions necessary to comply with requirements are commensurate with the following elements as outline in REGDOC-1.1.5 [Canadian Nuclear Safety Commission, 2019a]:

- The relative risks to health, safety, security, the environment, and the implementation of international obligations to which Canada has agreed.
- The characteristics of a facility or activity.

Methods in which criticality safety regulations may be met are detailed in REGDOC-2.4.3. Per REGDOC-2.4.3, a nuclear criticality safety program shall be developed and maintained in the licensed site to meet the CNSC nuclear criticality safety requirements [Canadian Nuclear Safety Commission, 2019b]. The scope of the program is dependent upon the category of operations with fissionable materials. The designed subcritical pile contains the following inventories:

- Fuel salt volume: 142,500 cm^3

- Mass of uranium: 26.94 kg
- Mass of U-235: 0.955 kg (small quantities ≤ 0.700 kg of U-235 [Canadian Nuclear Safety Commission, 2019b])
- Mass of graphite: 14,020 kg (active core + reflectors)
- Mass of beryllium: 27.19 kg

By the regulatory definition of ”small” and ”large” fissile quantities, this experiment will contain ”large” quantities of fissionable material, hence it is subject to the guidelines in the Nuclear Liability and Compensation Act. [Canadian Nuclear Safety Commission, 2019b]. A program will be developed to ensure that the entire process remains subcritical such that inadvertent criticality cannot occur. Program management practices are also included in the safety criticality program. This includes establishing responsible persons (e.g., supervisors) for ensuring nuclear criticality safety [Canadian Nuclear Safety Commission, 2014a]. Individuals that work or access the work area must be made aware of nuclear criticality safety and trained when appropriate. Written procedures, material control, equipment control, operational control and reviews, emergency procedures and a quality management program are all required under the management program [Canadian Nuclear Safety Commission, 2014a]. Proper human performance and administrative measures should be established to support safe operation.

Nuclear criticality safety is achieved by control of one or more parameters of a system within subcritical limits and allowances for process contingencies [Canadian Nuclear Safety Commission, 2014a]. As outlined in REGDOC-2.4.3, control may be exercised through physical restraints, use of instrumentation, chemical means, reliance on a natural or credible course of event, administrative procedures or other means [Canadian Nuclear Safety Commission, 2019b]. These controls should incorporate the principles of double contingency, redundancy, independence, diversity, fail-safe design and testability, where appropriate to ensure the availability and reliability of the system. As per REGDOC-2.5.2, two independent means of preventing re-criticality from any pathway or mechanism when the reactor is in the Guaranteed Shutdown State (GSS) [Canadian Nuclear Safety Commission, 2014b].

The shutdown margin for GSS shall be such that the core will remain subcritical for any credible changes in core configuration and reactivity addition. That and in addition to the largely negative temperature reactivity coefficient of the fuel salt and the graphite moderator, a deep subcritical state (i.e. GSS) is ensured. Furthermore, eight in-core flux detectors will provide real-time flux monitoring and communicate via control feedback system with the external neutron source, which can be switch off for any signs of rapid increase in flux. Where possible, this should be achieved without operator intervention [Canadian Nuclear Safety Commission, 2014b].

4.3 Material

The selected $NaF - BeF_2 - UF_4$ fuel salt is a eutectic mixture with the following weight composition:

- 72.09%wt-NaF.
- 14.02%wt-BeF_2.
- 13.89%wt-UF_4.

The melting temperature of the salt mixture is 736.46 K [Capelli *et al.*, 2014]. Density data were taken from Blanke *et al.* [1956]:

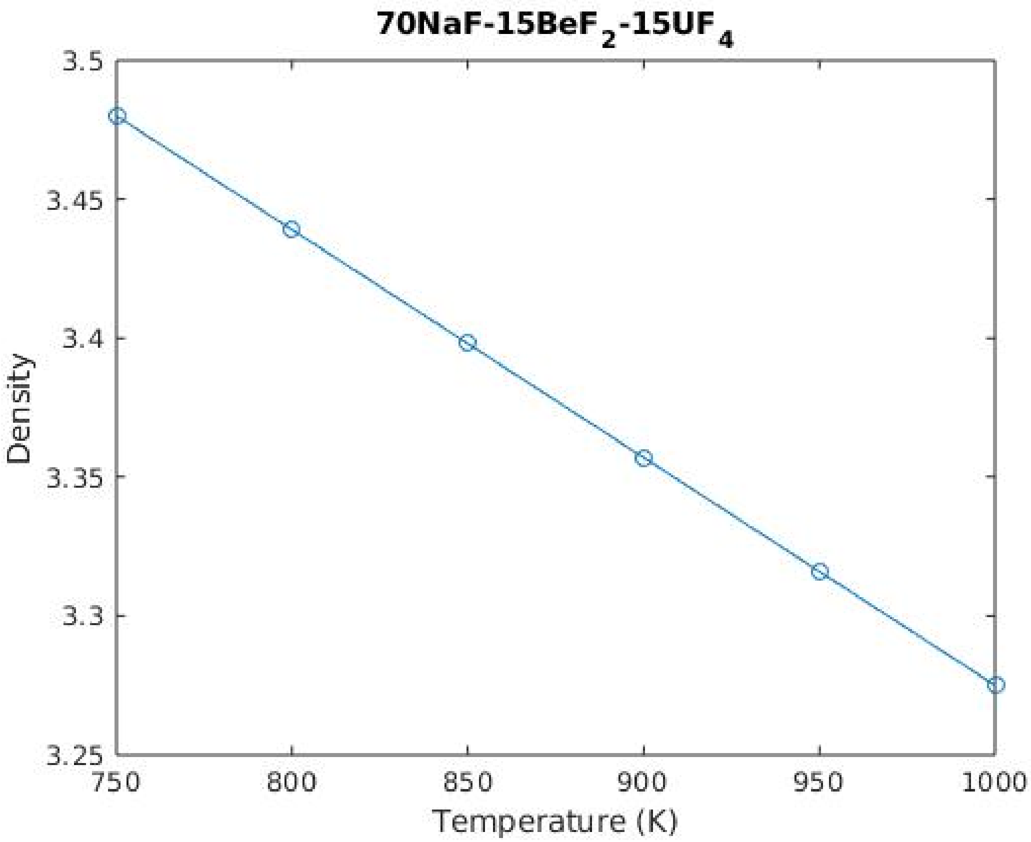

Figure 4.1: $NaF - BeF_2 - UF_4$ salt mixture density profile with respect to temperature.

An enrichment level of 3.50% was selected. For the reflector and moderator, a high purity graphite with a density of 1.80 g/cc was used. Density variation with respect to temperature is assumed to be negligible for graphite. For the external coating of the subcritical pile, stainless steel was used. Likewise, the density of the stainless steel was assumed to be constant with temperature variation. Hence, only the fuel salt density was varied with temperature in the analysis. Tables 4.1, 4.2 and 4.3 summarizes the compositions of fuel salt, graphite and stainless steel:

Table 4.1: Fuel Salt weight composition.

$NaF - BeF_2 - UF_4$		
Isotope	M (g/mol)	Wt%
Be-9	9.0122	5.4832
F-19	18.9984	60.8901
Na-23	22.9898	28.1943
U-234	234.0401	0.0017
U-235	235.0439	0.1925
U-238	238.0508	5.2382

Table 4.2: Graphite molar composition.

Graphite		
Isotope	M (g/mol)	At%
C	12.0107	99.9999982
B-10	10.0129	0.0000003
B-11	11.0093	0.0000015

Table 4.3: Stainless steel weight composition.

Stainless Steel		
Isotope	M (g/mol)	Wt%
Ni	58.6934	10.00
C	12.0107	0.03
Fe	55.8450	67.90
Cr	51.9961	19.00
Ti-46	47.8670	0.20
Si	28.0858	1.00
S	32.0657	0.03

4.4 Subcritical Pile

Changing the active core height changes the length of the fuel channels, whereas changing the active core diameter changes the number of fuel channels in the lattice. Changing the thickness of graphite reflectors changes neutron leakage in each direction. Either increasing the amount of fuel salt by increasing the active core height and diameter, or decreasing neutron leakage by increasing reflectors thicknesses, increases the k_{eff} of the subcritical pile. In order to meet the k_{eff} criterion for the subcritical pile, the active core height and diameter, thickness of the top, bottom and side reflectors were varied until a k_{eff} of 0.941 was achieved at 750 K. The final core design parameters are as follow:

Table 4.4: Summarized subcritical pile specifications

Design Parameter	**Details**
Active core height	210 cm
Active core diameter	70 cm
Pitch distance	16.4 cm
Top reflector thickness	40 cm
Bottom reflector thickness	30 cm
Side reflector thickness	30 cm
Stainless steel coating thickness	0.5 cm
Number of fuel channels	54
Fuel enrichment	3.5%

4.5 Neutron Source

In order to maintain a steady state neuron flux similar to that in a critical setting, an external neutron source is needed to provide a steady supply of neutrons. For the purpose of measuring different reactor's parameters, it is desirable to implement an external neutron source with operational flexibility, providing either a constant neutron flux, or an adjustable frequency of neutron pulses. Such operational flexibility can be obtained using a Deuterium-Deuterium fusion-based neutron source (DD), hence, the main reason it was selected for conducting the subcritical experiment.

There are multiple types of commonly used high flux neutron generators, which are suitable for subcritical physics experiment application, such as californium-252 fission neutron source, Deuterium-Tritium fusion-based neutron source, accelerator-driven lead-/lithium spallation neutron sources, etc. However, there are many advantages for using a DD neutron source, including:

- Ease of acquiring and transporting deuterium since it is a stable isotope, unlike tritium and californium-252 isotopes.
- Compact and relatively small setup.
- Relative low cost.
- Operational flexibility: constant flux mode or adjustable frequency pulsation mode.
- Semi-isotropic point source intensity profile.
- Generates approximately monoenergetic neutrons with an average energy of 2.45 MeV.

The primary components of a DD neutron generator are ([Starfire Industries LLC, 2019], [Ayllon *et al.*, 2018]):

1. High voltage power supply (50 - 250 kV).
2. Radio frequency driven multicusp ion source.
3. Copper based deuterium solid target.
4. Air or water based cooling system for the target.

A compact one-piece DD source is commercially available and can be purchased from manufacturers such as Starfire Industries LLC [Starfire Industries LLC, 2019]. However, due to the high temperature (up to 700 ^oC) inside the IMSR-400 subcritical pile, the DD neutron source would have to be collimated into a beam. Furthermore, collimating the DD neutron source would significantly reduce the utilization efficiency of generated neutrons. Instead, similar source configuration to the Yalina subcritical experiment can be built on site, using a separate multicusp ion source to bombard a copper based deuterium solid target situated at the center of the subcritical pile [Persson *et al.*, 2005].

Although a DD source behaves like a point source, neutron yield and energy are dependent on the polar angle relative to the direction of the incident ion beam. Energy and relative yield profiles with respect to the polar angle were plotted based on data from references Persson *et al.* [2005] and Starfire Industries LLC [2019].

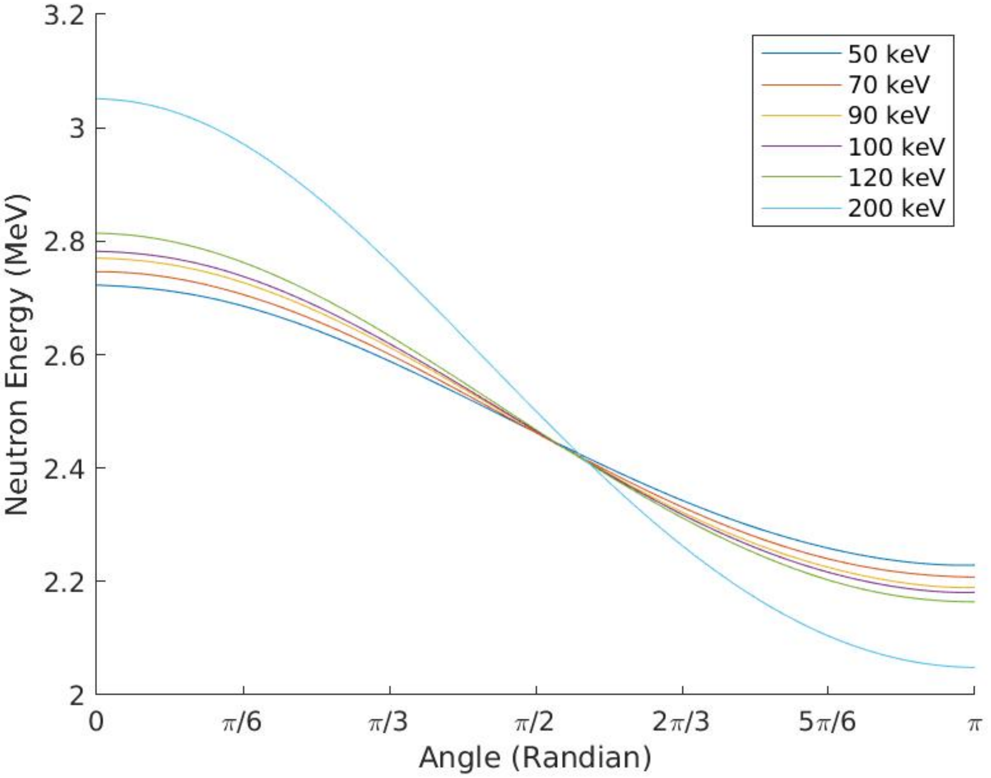

Figure 4.2: Energy angular dependency profile.

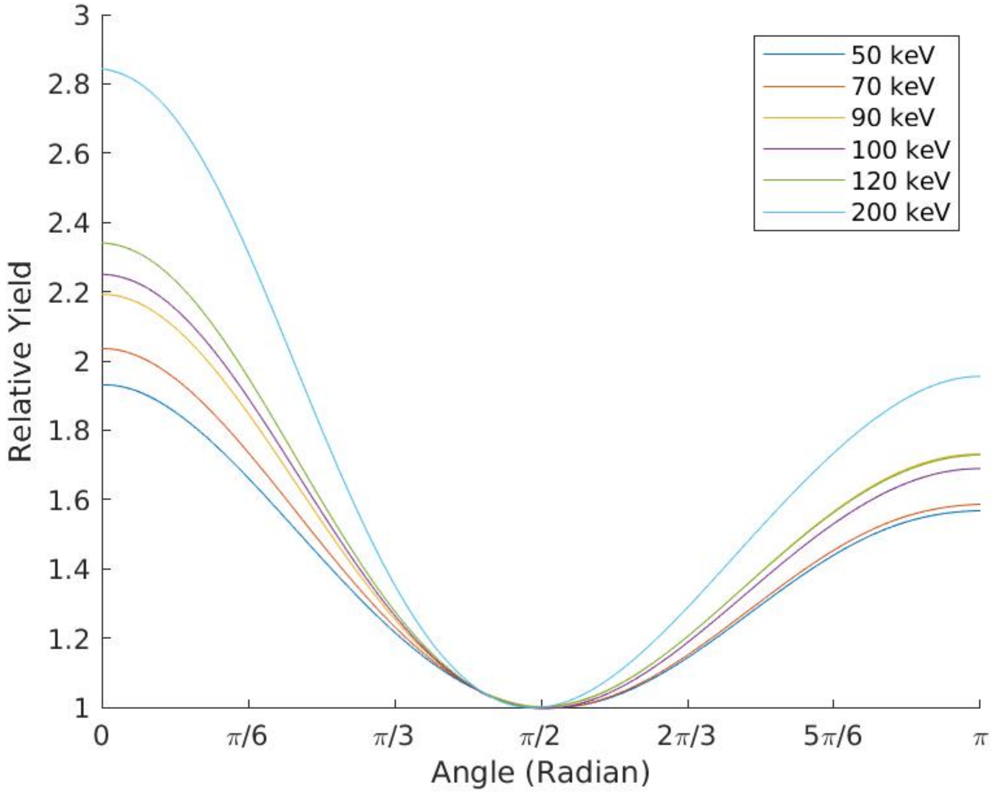

Figure 4.3: Relative yield angular dependency profile.

The energy and relative yield angular profiles associated with 200 keV deuterium ions were used in the current analysis.

4.6 In-core Flux Detectors

Helium-3 neutron detectors are commonly used in low-flux (relative to power reactor) and well-moderated environments thanks to helium-3's high absorption cross section for thermal neutrons. The average microscopic cross section of helium-3 at thermal energies is 5300 barns, decreasing as the inverse of the average neutron velocity (1 barn at 1 MeV and 0.2 barns at 10 MeV). Hence, the overall sensitivity of a helium-3 detector would also decrease based on the inverse of the neutron velocity [Chabot, 2009]. Moreover, it is common practice for manufacturers to specify helium-3 detector sensitivity in terms of neutron-induced count rate per unit thermal neutron flux independent of the neutron spectrum in the monitored space. Detector sensitivity is expressed by the unit **cps/nv**, or counts-per-second per $n\ cm^{-2}\ s^{-1}$. This means that for every neutron crossing a unit surface area of the helium-3 gas per second, a number of pulses is registered by the detector per second [Chabot, 2009]. The sensitivity of a helium-3 detector is characteristic of several design qualities, which can be optimized to improve the over all sensitivity. General description of these design qualities is provided in this section.

When a helium-3 nucleus absorbs a neutron, the reaction produces two ionized daughter products, tritium and hydrogen, with total kinetic energy of 764 keV, ionizing the gas in the chamber [Gobain, 2020]. The sensitivity of a helium-3 detector to neutrons and change in the neutron population is dictated by the following factors [Gilbert *et al.*, 2015]:

- Exogenous factors:
    - Diameter of the helium-3 gas chamber.
    - Pressure of the helium-3 gas.
    - Mixed impurities with the helium-3 gas.
- Endogenous factors:
    - Delay in flux-temperature feedback.
    - Location of the detector.
    - Neutron spectrum.

The exogenous factors contribute to the ratio between daughter products that successfully ionize the gas mixture in the chamber, versus the daughter products that collide with the wall (lost signal). The larger the diameter of the gas chamber, the less likely daughter products would collide with the wall. The larger the pressure, the denser the gas inside the chamber, and therefore, the smaller the mean free path of daughter products in the gas. Finally, mixing helium-3 with a denser low absorbent gas results in increasing the stopping power of the gas in the chamber, and thus, fewer daughter products will make it to the wall [Gilbert *et al.*, 2015].

The endogenous factors contribute to the detectability of change in the neutron signal as a result of varying core material's temperature. Firstly, the impact on the neutron population in the test core due to temperature change in graphite and fuel is not instantaneous. The time, which the neutron population in the test core takes to converge at the terminal value, is expressed by the number of generations (g) and the k_{eff}:

$$n = n_0 \sum_{g=1}^{\infty} k_{\text{eff}}^{g} \tag{4.1}$$

Where the duration of a single generation is the prompt generation time (Λ). Since the prompt generation time is in the order of milliseconds (0.001 second for graphite moderator), it would be sufficient to wait approximately 0.1 second after the temperature distribution in the core reaches equilibrium before collecting flux measurements. Secondly, accurate determination of reactor parameters such as k_{eff} require appropriate siting of the helium-3 detector inside core. Ideally, it would be desirable to fully capture the variation in the neutron population, which is characteristic of any reactivity insertion. In reality, different siting of the helium-3 detector may result in an overestimation or an underestimation of the k_{eff}. Lastly, variations in the neutron spectrum would affect the sensitivity of the helium-3 detector as a result of the change in the average absorption cross section of helium-3. For the IMSR-400's subcritical pile, graphite is the main source of neutron moderation and it does not expand with temperature, although slight spectrum hardening might occur when graphite heats up.

Note that in order to regard the experiment as feasible, the change in the neutron signal due to the reactivity feedback from temperature variation must be detectable. The conservative criterion for proving neutron signal change detectability is as follow:

$$1 - \frac{n(T \pm 50)}{n(T)} \geq 10\sigma \tag{4.2}$$

Where $n(T)$ is the detected neutron signal at a certain temperature T, $n(T \pm 50)$ is the neutron signal detected at 50 K temperature increments or decrements and σ is the statistical error (i.e. standard deviation) in the measurements. Note that the use of cumulative count rate instead of the count rate would significantly reduce the statistical error. By assuring that the change in the neutron signal is at least an order of magnitude larger than the statistical error, the change in the neutron signal can be easily distinguished from variations due to random errors.

Since helium-3 has a high thermal neutron absorption cross-section, it would be detrimental to the k_{eff} of the test core if an oversized helium-3 detector was used. Based on the literature review, a stainless-steel helium-3 detector, 1.270 cm in diameter, 24.992 cm in height, and under 10 atm of pressure would achieve a satisfactory sensitivity of 23 cps/nv [Gobain, 2020]. Furthermore, it would also be detrimental to the k_{eff} if the helium-3 detector was positioned near the center of the core. Additionally, placing the detector at a close proximity from the source will bias the readings of the detector by incorporating the change in the detected source rate.

The total change in the neutron signal, registered by the helium-3 detector, is approximately the sum of two signal change effects:

$$\Delta n_{tot} = \Delta n_{fission} + \Delta n_{src}, \tag{4.3}$$

Here $\Delta n_{fission}$ is the change in the neutron signal due to the change in the number of detected fission neutrons, and Δn_{src} is the change in the neutron signal due to the change in the number of detected source neutrons. Change in the detected source neutrons occurs not due to variations in the source output, but rather due to the change in the density of the fuel salt as temperature changes, allowing more neutrons to leak out. It can be concluded that excessive bias from the neutron source could cause an an overestimation of the k_{eff}.

Thermal flux mapping of the top and bottom sections of the subcritical pile with initially no in-core flux detectors was performed at 750 K isothermal core temperature as shown in figures 4.4 and 4.5.

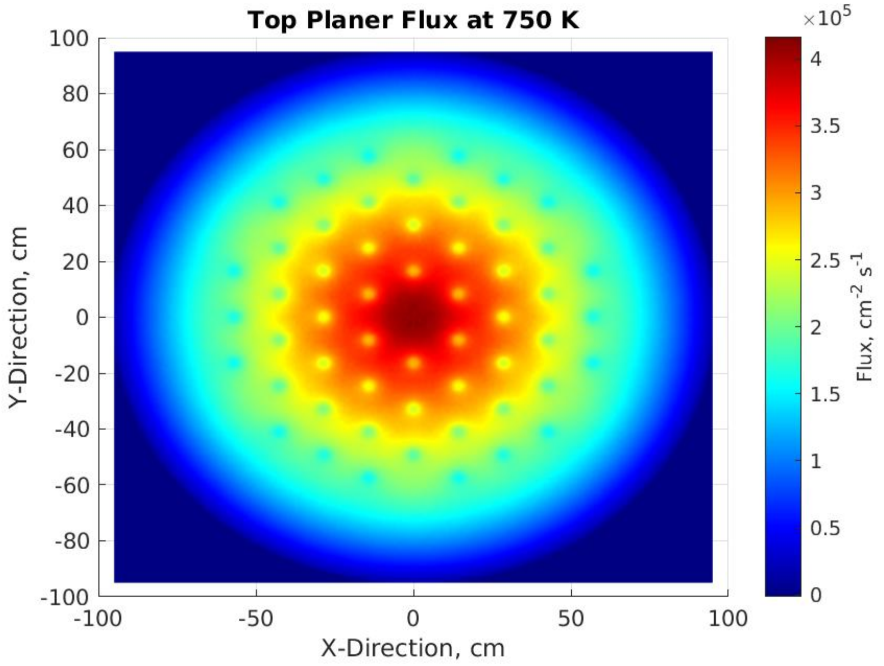

Figure 4.4: Top plane flux distribution at 750 K.

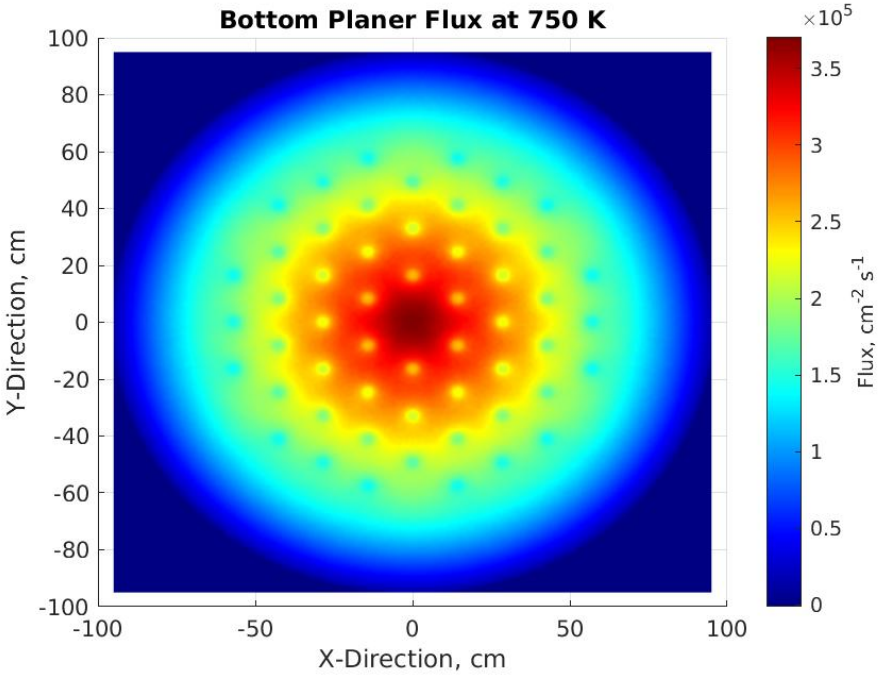

Figure 4.5: Bottom plane flux distribution at 750 K.

It can be observed that the thermal neutron flux at the top plane is higher than the bottom plane, which can be attributed to the larger thickness of the top reflector, resulting in less neutron leakage in the upward vertical direction. Flux mapping was also done at 1000 K, showing an identical pattern. In order to investigate the different zones potential to overestimate or underestimate the k_{eff}, equation (3.5) was used to compute the k_{eff} at 1000 K:

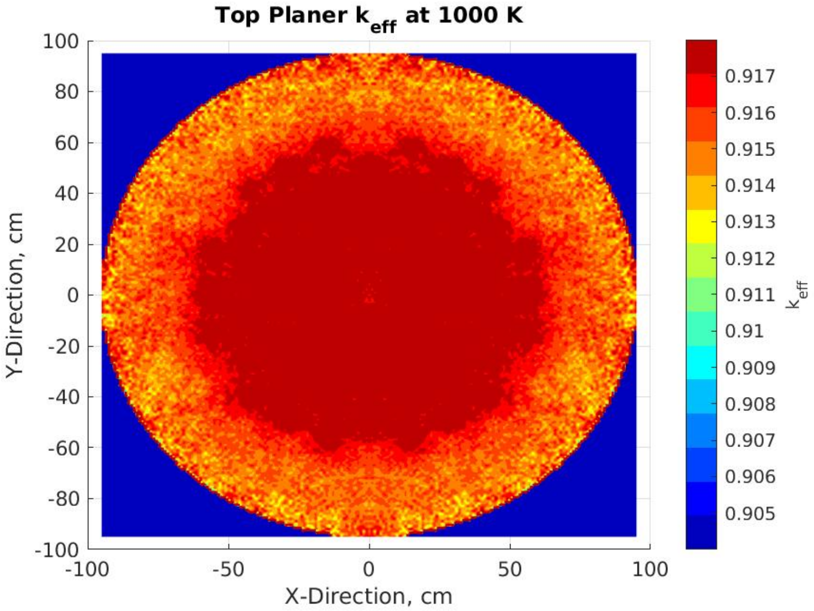

Figure 4.6: Computed k_{eff} at the top plane.

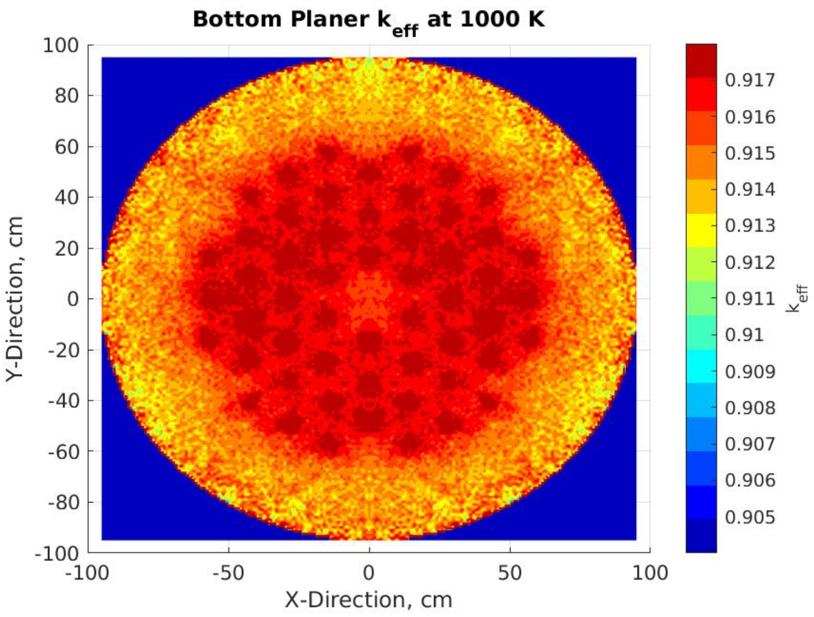

Figure 4.7: Computed k_{eff} at the bottom plane.

The k_{eff} automatically computed by Serpent at 1000 K is 0.911553. The k_{eff} is largely overestimated near the center of the core in either plane. Also, there is a lesser degree of overestimation in the bottom plane, which can be attributed to thinner bottom reflector. It is possible to conclude that placing the helium-3 detectors at the core peripheral regions would be most appropriate for more accurate estimation of the k_{eff}. Taking all factors into consideration, it was decided to make four thimbles, each containing two helium-3 detectors, one at the top and one at the bottom:

- North thimble: X = -72.5, Y = 0.0
- North-west thimble: X = -51.26524, Y = -51.26524
- West thimble: X = 0.0, Y = -72.5
- South-west thimble: X = 51.26524, Y = -51.26524

Thimbles are angularly spaced by 45^o. More details about the complete core configuration can be found in chapter 5.

Chapter 5

Simulation of Experiment

5.1 Serpent Code

Neutronic analyses of the IMSR-400 subcritical test were performed using Serpent, which is an ANSI-C based continuous energy Monte-Carlo reactor physic code, developed by VTT Technical Research Center in Finland [Leppänen, 2013]. The continues energy interaction data, including neutron cross sections and thermal scattering cross sections were imported from JEFF-3.1.1 library. The geometry of the subcritical pile can be defined using the **surf**, **lat** and **cell** input cards. Boolean intersection logic is applied using the **cell** input card to specify material or lattice filling between surfaces. Materials can be defined in terms of the atomic composition and the average temperature of each material, using the **mat** input card and based on the format in the Serpent's manual [Leppänen, 2008b].

Specifying the temperature of a certain material, using the **tmp** option, tells Serpent to sample the neutron cross section of isotopes at the specified temperature. Using the **therm** input card and based on the format in the Serpent's manual [Leppänen, 2008b], the thermal scattering cross section of the moderator can be sampled at the specified moderator temperature. If the **therm** input card is not used, the moderator's nuclides will be treated as free atoms, resulting in significant errors in the computation of k_{eff}. Furthermore, experimental values of the neutron cross sections are available only in 300 K increments (in Serpent) starting from 300 K up to 1800 K. Similarly, thermal scattering cross sections of graphite are available at certain temperatures [Leppänen, 2008a]. Nevertheless, Doppler broadening is applied to the neutron cross-section data, while interpolation is applied to thermal scattering cross-section data. Modeling the subcritical pile requires the external source calculation mode, which is activated using the **nps** input card. Time dependant external neutron source mode can be activated by defining a time binning structure, using the **tme** input card, and then referencing the name of the time binning structure in the definition of the **nps** input card.

Normalization of reaction rates, power and flux in the external source mode requires using **set srcrate**, which defines the source intensity in neutrons per second. The **src** input card is used to define a specific neutron emission profile with respect to energy, time, space and angle. The **src** input card can be used multiple times (each with a special name/identifier) in the input file. Information about the emission profiles are specified within the **src** input card, using the following options:

- Particle type: neutron (**n**) or photon (**p**).
- Direction, at which particles are emitted, using **sd** option.
- Material, cell or point where the source is located, using **sm**, **sc** or **sp** options respectively.
- Energy of the particle, using **se** option.
- The relative yield of a source with respect to other sources, defined within the geometry, using **sw** option.
- Defining a time range for the source emission, using **st** option.

Alternative to using the options described, the **si** option can be used to define a source with complex energy, time, spacial and angular profiles. However, using the **si** option requires modifying the **usersrc.c** subroutine, located in the Serpent installation directory. Next, the **det** input card is used to compute a certain response such as deposited fission energy, flux distribution and different reaction rates. Neutron energy groups, at which responses are scored, can be defined using the **ene** input card. User-defined detectors must indicate the neutron energy group structure to be used. Also, if the time dependent mode is activated, the **tme** input card must be referenced in the definition of the **det** input card. Note that, seperate **tme** input cards must be defined for the **nps** and the **det** input cards.

5.2 Neutron Cross-section Library

The standard neutron cross-section library, used to conduct neutronic analysis of the IMSR-400, is the JEFF3.1.1 library, imported in ACE format [Leppänen, 2008b]. Referencing the JEFF3.1.1 library in the input file was done as follow:

```
set acelib "/home/moe235/jeff311/sss_jeff311u.xsdata"
```

The thermal scattering data of metallic beryllium were imported from the Nuclear Energy Agency [2016] website and used for the thermal scattering treatment of beryllium difluoride salt component. This was done because the treatment of beryllium in the salt as metallic beryllium is better than a free-atom treatment. According to Mei *et al.* [2013], the inelastic scattering cross-section of beryllium bound in the salt is larger than that of a free beryllium atom. This means that neutrons do not reduce speed as much and scatter at a smaller angle than expected, causing an overestimation of the k_{eff}. The transitional weight, which is described as the ion's migration ability, is expected to be small for beryllium since it is mainly contained in a clump of Na_2BeF_4 [Capelli *et al.*, 2014]. The validity of this assumption should be investigated. It is possible to generate salt mixture specific thermal scattering data, using NJOY code [Mei *et al.*, 2013]. However, it is out of the scope of this thesis.

5.3 Material Definition

The material files are made separate from the main input file, but are linked to the main input file, using the input card **include** as follow:

```
include "./materials/Graph.serp" %Graphite between 750-1000 K
include "./materials/Fuel.serp"  %%72.09NaF-%14.02BeF4-%13.89UF4 between 750-1000 K
include "./materials/SS.serp"    %Stainless-Steel 304L between 750 - 1000 K
include "./materials/OtherMat.serp" %Different Material at a Constant Temperature
```

Description of each material file is provided in subsections 5.3.1, 5.3.2, 5.3.3 and 5.3.4.

5.3.1 Graphite

Based on the **mat** input card format described in section 5.1 and the composition data of graphite in table 4.2, graphite was defined at 50 K temperature increments between 750 and 1000 K (only 750 K and 1000 K are shown below).

```
%%% T = 750 K
mat GraphT750 -1.80 tmp 750.00 moder graphT750 6000 rgb 75 75 75
C-nat.06c 99.999998
B-10.06c 0.0000004
B-11.06c 0.0000016
therm graphT750 750.0 grj3.16t grj3.18t
.
.
.
%%% T = 1000 K
mat GraphT1000 -1.80 moder graphT1000 6000 tmp 1000.0 rgb 75 75 75
C-nat.09c 99.999998
B-10.09c 0.0000004
B-11.09c 0.0000016
therm graphT1000 grj3.20t
```

Doppler broadening temperatures for *GraphT750* and *GraphT1000* material cards are specified at 750 and 1000 K respectively, using the **tmp** option. The thermal scattering data names, *graphT750* and *graphT1000*, are linked to the thermal scattering library, using **moder** and **therm** options. The entries *grj3.16t*, *grj3.18t* and *grj3.20t* indicate the thermal scattering data at 600, 700 and 1000 K respectively. Since thermal scattering data at 750 K is not available, interpolation is applied by defining the desired temperature and the range of two available thermal scattering data.

5.3.2 Fuel

Based on the **mat** input card format described in section 5.1 and the composition data of the fuel salt in table 4.1, the fuel salt was defined at 50 K temperature increments between 750 and 1000 K (only 750 K and 1000 K are shown below).

```
mat SaltT750 0.06659334 moder saltT750 4009 tmp 750 rgb 255 255 0
Be-9.06c   0.14020000
F-19.06c   1.55690000
Na-23.06c  0.72090000
U-234.06c  0.00004240
U-235.06c  0.00492148
U-238.06c  0.13393612
therm saltT750 750 be04.32t be05.32t
.
.
mat SaltT1000 0.06267044 moder saltT1000 4009 tmp 1000 rgb 255 255 0
Be-9.09c   0.14020000
F-19.09c   1.55690000
Na-23.09c  0.72090000
U-234.09c  0.00004240
U-235.09c  0.00492148
U-238.09c  0.13393612
therm saltT1000 be06.32t
```

As mention in section 5.2, the thermal scattering library of beryllium metal was included in the definition of the fuel salt. Similar definition format of Doppler broadening and the thermal scattering library to graphite material cards was used. Specifying positive values of composition indicates a molar-based definition of the composition.

5.3.3 Stainless Steel

Based on the **mat** input card format described in section 5.1 and the composition data of the stainless steel in table 4.3, stainless steel was defined at 50 K temperature increments between 750 and 1000 K (only 750 K and 1000 K are shown below).

```
%%% T = 750 K
mat SST750 -8.027 tmp 750.0 rgb 112 128 144
Ni-nat.06c -0.100
C-nat.06c  -0.0003
Fe-nat.06c -0.67895
Cr-nat.06c -0.19
Ti-nat.06c -0.002
Si-nat.06c -0.01
S-nat.06c  -0.0003
.
.
%%% T = 1000 K
mat SST1000 -8.027 tmp 1000.0 rgb 112 128 144
Ni-nat.09c -0.100
C-nat.09c  -0.0003
Fe-nat.09c -0.67895
Cr-nat.09c -0.19
Ti-nat.09c -0.002
Si-nat.09c -0.01
S-nat.09c  -0.0003
```

Only Doppler broadening is applied in the definition of stainless steel since it is primary composed of heavy atoms (e.g. iron, cobalt and nickel), for which the free-atom treatment of the low-energy scattering cross section is appropriate.

5.3.4 Additional Material

Additional materials were defined such as argon (for cover gas) and helium-3 (for in-core flux detectors). Multiple helium-3 material cards were defined in order to score responses for each helium-3 detector separately.

```
%%% Argon Cover Gas
```

```
mat Argon -0.0016238 rgb 128 0 128
Ar-36.06c  0.334
Ar-38.06c  0.063
Ar-40.06c  99.604

%%% Helium-3 - Detector#1
mat He3_1 -0.0016283 rgb 255 140 0
He-3.06c -1.00000000
.
.
.
%%% Helium-3 - Detector#12
mat He3_12 -0.0016283
rgb 255 140 0
He-3.06c -1.00000000
```

Notice that for helium-3 and argon, temperature is assumed to be constant (constant cooling and circulation).

5.4 Geometry Definition

After materials are defined, surfaces, lattices and cells can be used to define the geometry of the core and fill defined volumes with desired materials.

5.4.1 Lattices

The lattice definition contains a mix of surface and cell definitions, used to define geometries that can be arranged in a lattice. Two lattice types were defined: a) active core hexagonal lattice and b) helium-3 detector thimbles circular lattice. The active core hexagonal lattice was defined as follow:

```
%% Fuel Channels
%%% Filled (universe #1)
surf A cyl    0.0 0.0 2.000
surf B hexyc  0.0 0.0 8.200
cell A 1 SaltT750  -A
```

```
cell B 1 GraphT750  A -B

%%% just Graphite (universe #2)
surf C hexyc  0.0 0.0 8.200
cell C 2 GraphT750 -C

%%% Hexagonal lattice of fueled channels: 53 channels, pitch = 14cm (universe #3)
lat 3 3 0 0 15 17 16.4
2 2 2 2 2 2 2 2 2 2 2 2 2 2 2
 2 2 2 2 2 2 2 2 2 2 2 2 2 2 2
  2 2 2 2 2 2 2 2 2 2 2 2 2 2 2
   2 2 2 2 2 2 2 2 2 2 2 2 2 2 2
    2 2 2 2 2 2 2 2 1 1 1 2 2 2 2
     2 2 2 2 2 2 1 1 1 1 1 1 2 2 2
      2 2 2 2 2 1 1 1 1 1 1 1 2 2 2
       2 2 2 2 1 1 1 1 1 1 1 1 2 2 2
        2 2 2 2 1 1 1 2 1 1 1 2 2 2 2
         2 2 2 1 1 1 1 1 1 1 1 2 2 2 2
          2 2 2 1 1 1 1 1 1 1 2 2 2 2 2
           2 2 2 1 1 1 1 1 1 2 2 2 2 2 2
            2 2 2 2 1 1 1 2 2 2 2 2 2 2 2
             2 2 2 2 2 2 2 2 2 2 2 2 2 2 2
              2 2 2 2 2 2 2 2 2 2 2 2 2 2 2
               2 2 2 2 2 2 2 2 2 2 2 2 2 2 2
                2 2 2 2 2 2 2 2 2 2 2 2 2 2 2
```

Universe number 1 (i.e. pattern 1) defines the circular fuel salt channel with 2 cm radius, bounded by a graphite hexagon with 8.2 cm outer-circle radius. Universe number 2 (i.e. pattern 2), represents an empty lattice position with graphite only. Using the **lat** input card type 3 (for hexagonal infinite lattice), the patterns in universes 1 and 2 are repeated and arranged in the hexagonal lattice with a pitch distance of 16.4 cm.

Next, the circular lattice of helium-3 detector thimbles was defined as follow:

```
%% Measuring Channels
%%% Thimble (universe #4)
pin 4
Argon      2.000
GraphT750

%%% Just Graphite (universe #5)
```

```
pin 5
GraphT750

%%% Circular lattice of empty thimbles (universe #6)
lat 6 4 0.0 0.0 2
1 0.000 0.000 5
8 72.50 180.0 4 4 4 4 5 5 5 5
```

Universe number 4 (i.e. pattern 4) represents a hollow cylinder with argon gas on the inside and graphite on the outside. Universe number 5 (i.e. pattern 5) represents a solid graphite cylinders. Since it is intended to have only four detector thimbles, the **lat** input card type 4 (for circular infinite lattice), the patterns in universes 4 and 5 are repeated and arranged over a radius of 72.50 cm. Now that the thimbles are created, helium-3 detector geometries can be defined and positioned inside the thimbles by surface intersection in the **cell** input card.

5.4.2 Surfaces

The definition of surfaces was done in three parts: a) infinite planes, b) infinite surfaces and c) finite surfaces. The definition of infinite planes was done as follow:

```
%%% Core === Planes                     %Under               < Above
surf C10 pz   0.000000                 %Outside             < External Coating
surf C11 pz   0.500000                 %External Coating    < Bottom Reflector
surf C12 pz   30.50000                 %Bottom Reflector    < Active Core
surf C14 pz   240.5000                 %Active Core         < Top Reflector
surf C15 pz   280.5000                 %Top Reflector       < External Coating
surf C16 pz   281.0000                 %External Coating    < Outside
```

The start reference point is 0.0 cm and the end reference point is 281.0 cm, representing the bottom and top vertical ends of the subcritical core respectively. The comments in the code describes the filling sections above and under each surface. **Outside** indicates a void filling.

Next, the definition of infinite surfaces was done as follow:

```
%%% Core === Infinite Cylinders        %Inward              < Outward
```

```
surf C17 cyl  0.000000  0.000000  70.00 %Active Core         < Side Reflector
surf C18 cyl  0.000000  0.000000  95.00 %Side Reflector      < Coating
surf C19 cyl  0.000000  0.000000  95.50 %Coating             < Outside
```

Only infinite cylinders were used in the definition of the subcritical pile geometry. The comments in the code provide indications of the section filling inward and outward of each infinite cylinder.

Finally, the definition of finite surfaces was done as follow:

```
%%% Core === Finite Cylinders
surf C20 cyl  0.000000  0.000000  95.50  0.000000  281.00 %Dummy cylinder
surf C21 cyl  0.000000  0.000000  4.000  135.0000  281.00 %Source Thimble

%%% Detectors === Finite Cylinders
%%%% Detector Thimble 1
surf D10 cyl -72.50000  0.000000  0.635  31.0500  55.942 %Bottom Detector He-3 Gas
surf D11 cyl -72.50000  0.000000  0.640  31.0000  55.992 %Bottom Detector Gas Chamber
surf D14 cyl -72.50000  0.000000  0.635  215.058  239.95 %Top Detector He-3 Gas
surf D15 cyl -72.50000  0.000000  0.640  215.008  240.00 %Top Detector Gas Chamber

%%%% Detector Thimble 2
surf D16 cyl -51.26524 -51.26524  0.635  31.0500  55.942 %Bottom Detector He-3 Gas
surf D17 cyl -51.26524 -51.26524  0.640  31.0000  55.992 %Bottom Detector Gas Chamber
surf D20 cyl -51.26524 -51.26524  0.635  215.058  239.95 %Top Detector He-3 Gas
surf D21 cyl -51.26524 -51.26524  0.640  215.008  240.00 %Top Detector Gas Chamber

%%%% Detector Thimble 3
surf D22 cyl  0.000000 -72.50000  0.635  31.0500  55.942 %Bottom Detector He-3 Gas
surf D23 cyl  0.000000 -72.50000  0.640  31.0000  55.992 %Bottom Detector Gas Chamber
surf D26 cyl  0.000000 -72.50000  0.635  215.058  239.95 %Top Detector He-3 Gas
surf D27 cyl  0.000000 -72.50000  0.640  215.008  240.00 %Top Detector Gas Chamber

%%%% Detector Thimble 4
surf D28 cyl  51.26524 -51.26524  0.635  31.0500  55.942 %Bottom Detector He-3 Gas
surf D29 cyl  51.26524 -51.26524  0.640  31.0000  55.992 %Bottom Detector Gas Chamber
surf D32 cyl  51.26524 -51.26524  0.635  215.058  239.95 %Top Detector He-3 Gas
surf D33 cyl  51.26524 -51.26524  0.640  215.008  240.00 %Top Detector Gas Chamber
```

Only finite cylinders were used in the definition of the subcritical pile geometry. The comments in the code provide indications of the section filling each finite cylinder.

5.4.3 Cells

Using the materials, surfaces and lattices defined already, Boolean intersection logic is applied using the **cell** input card to position lattices and fill volumes with materials.

```
%%% SS Coating
cell C10 0 SST750    C10 -C11      -C19      %Bottom SS Coating
cell C11 0 SST750    C11 -C15  C18 -C19      %Side SS Coating
cell C12 0 SST750    C15 -C16      -C19  C21 %Top SS Coating

%%% Reflectors
cell C13 0 GraphT750 C11 -C12      -C18      %Bottom Reflector
cell C14 0 fill 6    C12 -C14  C17 -C18  D11 D15 D17 D21 D23 D27 D29 D33
cell C15 0 fill 6    C14 -C15      -C18  C21 %Top Reflector

%%% Active Core
cell C16 0 fill 3    C12 -C14      -C17  C21 %Full Active Core

%%% Detectors
%%%% Thimble 1
cell D10 0 He3_1         -D10                %Bottom Detector He-3 Gas
cell D11 0 SST300    D10 -D11                %Bottom Detector Gas Chamber
cell D14 0 He3_3         -D14                %Top Detector He-3 Gas
cell D15 0 SST300    D14 -D15                %Top Detector Gas Chamber

%%%% Thimble 2
cell D16 0 He3_4         -D16                %Bottom Detector He-3 Gas
cell D17 0 SST300    D16 -D17                %Bottom Detector Gas Chamber
cell D20 0 He3_6         -D20                %Top Detector He-3 Gas
cell D21 0 SST300    D20 -D21                %Top Detector Gas Chamber

%%%% Thimble 3
cell D22 0 He3_7         -D22                %Bottom Detector He-3 Gas
cell D23 0 SST300    D22 -D23                %Bottom Detector Gas Chamber
cell D26 0 He3_9         -D26                %Top Detector He-3 Gas
cell D27 0 SST300    D26 -D27                %Top Detector Gas Chamber

%%%% Thimble 4
cell D28 0 He3_10        -D28                %Bottom Detector He-3 Gas
cell D29 0 SST300    D28 -D29                %Bottom Detector Gas Chamber
cell D32 0 He3_12        -D32                %Top Detector He-3 Gas
cell D33 0 SST300    D32 -D33                %Top Detector Gas Chamber
```

```

%%% Neutron Source
cell N10 0 Argon        -C21                %Source Thimble Cavity

%%% Outside
cell U12 0 outside   C20
```

The negative sign next to the surface name indicates ”toward the negative direction” and ”inward” for planes and cylinders respectively. Notice the use of **fill** option for lattices, and material identifiers for enclosed volumes by surfaces.

5.5 Calculation Options

Standard to all external neutron source calculation modes, the boundary condition in all directions are set as ”black” (i.e. type 1: neutron dies once crossed to ”outside”), and the source emission rate (for normalization purpose) is set as 300 million neutrons per second:

```
%%% Black Boundry condition
set bc 1

%%% External Source Rate Normalization Option
set srcrate 3.0E+08
```

5.5.1 Calculation Mode

The definition of calculation options depends on whether or not time dependence is applied. The calculation options for the static external neutron source mode are as follows:

```
%%% External Neutron Source Mode Enabled via nps input card
set nps 40000000 4000
```

For the static mode, 40 million neutron histories, distributed over 4000 batches, were used.

Next, the calculation options for the dynamic external neutron source mode are as follows:

```
%%% Enable emission of delayed neutrons
set delnu 1

%%% Time bin structure of neutron source emission (type 2: uniform binning)
tme srctime 2 1 0.000 600.0

%%% External Neutron Source Mode Enabled via nps input card
set nps 120000000 12000 srctime
```

In the dynamic mode, the emission of delayed neutrons was enabled via the **delnu** input card (switch off by default). A time binning structure was defined via the **tme** input card, indicating no population control and a running time duration of 600 seconds. 120 million neutron histories, distributed over 12000 batches, were used for the constant source operation calculations. For the pulsed source operation, 1 billion neutron histories, distributed over 10000 batches, and a total running time of 410 seconds were used.

5.5.2 Source Definition

Source definition was done using the **si** option in the **src** input card. There were three types of calculations performed, each with unique source definition:

1. Static continuous DD source operation.
2. Dynamic fluctuating (at 0,1 and 2%) DD source operation.
3. Dynamic pulsed DD source operation.

Static Continues DD Source Operation

The source definition in the static continues DD source operation was done by first inserting the following lines in the **usersrc.c** Serpent's subroutine:

```
  /* Type 4: Point Source Polyenergitic for Static Source Mode */
  else if (params[0] == 4)
```

```
{
  double xc, yc, zc, pE1, pE2, pE3, pE4, pE5, pE6, pE7, pE8, pE9;
  double pW1, pW2, pW3, pW4, pW5, pW6, pW7, pW8, pW9;
  /* Define geometrical parameters */
  xc = params[1];
  yc = params[2];
  zc = params[3];
  pE1 = params[4];  pE2 = params[5];  pE3 = params[6];
  pE4 = params[7];  pE5 = params[8];  pE6 = params[9];
  pE7 = params[10]; pE8 = params[11]; pE9 = params[12];
  pW1 = params[13]; pW2 = params[14]; pW3 = params[15];
  pW4 = params[16]; pW5 = params[17]; pW6 = params[18];
  pW7 = params[19]; pW8 = params[20]; pW9 = params[21];

  /* Coordinates */
  *x = xc;
  *y = yc;
  *z = zc;

  /* Isotropic direction */
  IsotropicDirection(u, v, w, id);

  /* Ployenergitic DD Source */
  *E = pE1*acos(-*w)*acos(-*w)*acos(-*w)*acos(-*w)*acos(-*w)*acos(-*w)*acos(-*w)*
  acos(-*w) + pE2*acos(-*w)*acos(-*w)*acos(-*w)*acos(-*w)*acos(-*w)*acos(-*w)*acos
  (-*w) + pE3*acos(-*w)*acos(-*w)*acos(-*w)*acos(-*w)*acos(-*w)*acos(-*w) + pE4*
  acos(-*w)*acos(-*w)*acos(-*w)*acos(-*w)*acos(-*w) + pE5*acos(-*w)*acos(-*w)*acos
  (-*w)*acos(-*w) + pE6*acos(-*w)*acos(-*w)*acos(-*w) + pE7*acos(-*w)*acos(-*w) +
  pE8*acos(-*w) + pE9;

  /* Anistropical Relative Yield of the DD Source */
  *wgt = pW1*acos(-*w)*acos(-*w)*acos(-*w)*acos(-*w)*acos(-*w)*acos(-*w)*acos(-*w)*
  acos(-*w) + pW2*acos(-*w)*acos(-*w)*acos(-*w)*acos(-*w)*acos(-*w)*acos(-*w)*acos
  (-*w) + pW3*acos(-*w)*acos(-*w)*acos(-*w)*acos(-*w)*acos(-*w)*acos(-*w) + pW4*
  acos(-*w)*acos(-*w)*acos(-*w)*acos(-*w)*acos(-*w) + pW5*acos(-*w)*acos(-*w)*acos
  (-*w)*acos(-*w) + pW6*acos(-*w)*acos(-*w)*acos(-*w) + pW7*acos(-*w)*acos(-*w) +
  pW8*acos(-*w) + pW9;

  /* All at times 0.0 */
  *t = 0.0;
}
```

Where pW and pE are polynomial fitting coefficients of the relative yield and energy angular profiles shown in figures 4.3 and 4.2 respectively. Then, the source definition in the Serpent input file was done as follows:

```
src 1 n si 22 4  0.00  0.00 135.50
2.218931e-04 -3.503849e-03
2.368881e-02 -9.013268e-02
1.978139e-01 -1.499677e-01
-2.331793e-01 -1.115409e-02
3.051273e+00 1.061613e-02
-1.702834e-01 1.107757e+00
-3.663414e+00 6.086049e+00
-3.673442e+00 -9.885682e-01
-1.284070e-01 2.844128e+00
```

The first entry after **si** indicates the number of parameters used to define the source profile. The second entry references the exact source definition from the **usersrc.c** subroutine. The next three entries indicate the location of the point source (X = 0 cm, Y = 0 cm and Z = 135.5 cm). The remaining entries are the polynomial fitting coefficients of the energy and relative yield angular dependencies (see figures 4.2 and 4.3).

Dynamic Fluctuating DD Source Operation

Similar lines of code to the static calculation were inserted into the **usersrc.c** Serpent's subroutine, except for the line defining the time of emission (removed ***t = 0.0;**). Multiple **src** input cards were defined, each with a specific time range (**st** option) and yield (**sw** option) in order to induce source fluctuation with time, based on a stable period of 20 seconds:

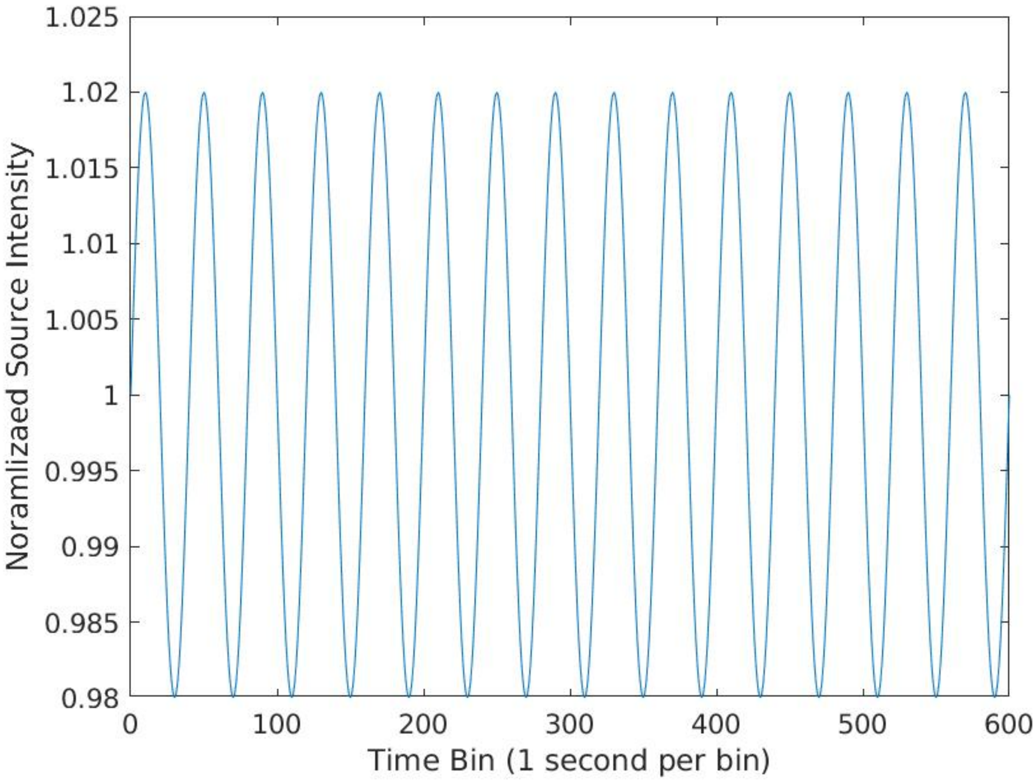

Figure 5.1: Forced yield fluctuation of 2% of the DD source.

Essentially, the source output would change every second. The source definition was made into a separate file and linked in the Serpent input file:

```
include "./SRC_DEF/src5f0.txt"
% OR
include "./SRC_DEF/src5f1.txt"
% OR
include "./SRC_DEF/src5f2.txt"
```

Which contains:

```
src      1 n si 22 5   0.00   0.00 135.50
2.218931e-04 -3.503849e-03
2.368881e-02 -9.013268e-02
1.978139e-01 -1.499677e-01
-2.331793e-01 -1.115409e-02
3.051273e+00 1.061613e-02
```

```
-1.702834e-01 1.107757e+00
-3.663414e+00 6.086049e+00
-3.673442e+00 -9.885682e-01
-1.284070e-01 2.844128e+00
sw 1.000000e+00 st   0.0   1.0
.
.
.
src   600 n si 22 5  0.00  0.00 135.50
2.218931e-04 -3.503849e-03
2.368881e-02 -9.013268e-02
1.978139e-01 -1.499677e-01
-2.331793e-01 -1.115409e-02
3.051273e+00 1.061613e-02
-1.702834e-01 1.107757e+00
-3.663414e+00 6.086049e+00
-3.673442e+00 -9.885682e-01
-1.284070e-01 2.844128e+00
sw 9.984357e-01 st 599.0 600.0
```

Dynamic Pulsed DD Source Operation

The same **usersrc.c** option used for the source fluctuation was used for the pulsed source operation. The only difference is in the use of the **st** option in the definition of the time range, and no use of the **sw** option:

```
src     1 n si 22 6  0.00  0.00 135.50
2.218931e-04 -3.503849e-03
2.368881e-02 -9.013268e-02
1.978139e-01 -1.499677e-01
-2.331793e-01 -1.115409e-02
3.051273e+00 1.061613e-02
-1.702834e-01 1.107757e+00
-3.663414e+00 6.086049e+00
-3.673442e+00 -9.885682e-01
-1.284070e-01 2.844128e+00
st   0.0000000000   0.0000010000

src     2 n si 22 6  0.00  0.00 135.50
2.218931e-04 -3.503849e-03
2.368881e-02 -9.013268e-02
```

```
1.978139e-01 -1.499677e-01
-2.331793e-01 -1.115409e-02
3.051273e+00 1.061613e-02
-1.702834e-01 1.107757e+00
-3.663414e+00 6.086049e+00
-3.673442e+00 -9.885682e-01
-1.284070e-01 2.844128e+00
st   0.0250000000   0.0250010000
.
.
.
```

Notice how the first source lasts for only 1 microseconds, and the second source start emitting neutrons after 25 milliseconds and lasts for the same duration. This definition corresponds to source pulsation at 40 Hz and a pulse width of 1 microseconds.

5.5.3 User-defined Detectors

The detector definition consist of time binning (dynamic mode only), energy-group structure, the response type, material/cell where response is scored and the volume of material/cell. For the static calculations detectors were defined as follow:

```
%%% 1 energy-group structre (Type 1 Grid Definition: Specify Energy Bin Boundries)
ene 1 1
1.000E-11 1.000E+01

%%% Total fission energy deposition (unit: Watt)
det POWER  de 1 dr -8 void

%%% Macroscopic total capture rate in Helium-3 Detector (unit: Rxn. cm-3.s-1)
det He3_1  de 1 dr -2 He3_1  dm He3_1  dv 31.5324
det He3_3  de 1 dr -2 He3_3  dm He3_3  dv 31.5324
det He3_4  de 1 dr -2 He3_4  dm He3_4  dv 31.5324
det He3_6  de 1 dr -2 He3_6  dm He3_6  dv 31.5324
det He3_7  de 1 dr -2 He3_7  dm He3_7  dv 31.5324
det He3_9  de 1 dr -2 He3_9  dm He3_9  dv 31.5324
det He3_10 de 1 dr -2 He3_10 dm He3_10 dv 31.5324
det He3_12 de 1 dr -2 He3_12 dm He3_12 dv 31.5324
```

For the dynamic fluctuation calculations detectors were defined as follow:

```
%%% Time bin structure of detectors
tme dettime 2 2400 0.000 600.0

%%% 1 energy-group structre (Type 1 Grid Definition: Specify Energy Bin Boundries)
ene 1 1
1.000E-11 1.000E+01

%%% Total fission energy deposition (unit: Watt)
det POWER  de 1 dr -8 void di dettime

%%% Macroscopic total capture rate in Helium-3 Detector (unit: Rxn. cm-3.s-1)
det He3_1  de 1 dr -2 He3_1  dm He3_1  dv 31.5324 di dettime
det He3_3  de 1 dr -2 He3_3  dm He3_3  dv 31.5324 di dettime
det He3_4  de 1 dr -2 He3_4  dm He3_4  dv 31.5324 di dettime
det He3_6  de 1 dr -2 He3_6  dm He3_6  dv 31.5324 di dettime
det He3_7  de 1 dr -2 He3_7  dm He3_7  dv 31.5324 di dettime
det He3_9  de 1 dr -2 He3_9  dm He3_9  dv 31.5324 di dettime
det He3_10 de 1 dr -2 He3_10 dm He3_10 dv 31.5324 di dettime
det He3_12 de 1 dr -2 He3_12 dm He3_12 dv 31.5324 di dettime
```

Notice that the time-binning structure **dettime** was defined such that to collect detector response every 0.25 second, starting at 775 second and ending at 800 second.

For the dynamic pulsed calculations detectors were defined as follow:

```
%%% Time bin structure of detectors
tme dettime 2 50000 775.0 800.0

%%% 1 energy-group structre (Type 1 Grid Definition: Specify Energy Bin Boundries)
ene 1 1
1.000E-11 1.000E+01

%%% Total fission energy deposition (unit: Watt)
det POWER  de 1 dr -8 void di dettime

%%% Macroscopic total capture rate in Helium-3 Detector (unit: Rxn. cm-3.s-1)
det He3_3  de 1 dr -2 He3_3  dm He3_3  dv 31.5324 di dettime
det He3_6  de 1 dr -2 He3_6  dm He3_6  dv 31.5324 di dettime
```

Since a single pulse response profile spans over 25 milliseconds for 40 Hz pulsation, the time binning for the pulsed calculations were defined such that to collect response every 0.5 millisecond in order to capture the full pulse response profile. Detector response was collected for the last 25 seconds, registering 1000 pulse profiles. This was done in order to reduce statistical error and conserve memory usage.

5.6 Mesh and Geometry Plotting

The geometry plots can be automatically generated by Serpent using the **plot** input card as follow:

```
plot 1 500 735
plot 2 500 735
plot 3 500 500
```

Where **plot** type 1, 2 and 3 are cross-sectional views of the X-Z plane at Y=0, Y-Z plane at X=0 and X-Y plane at Z=0 respectively.

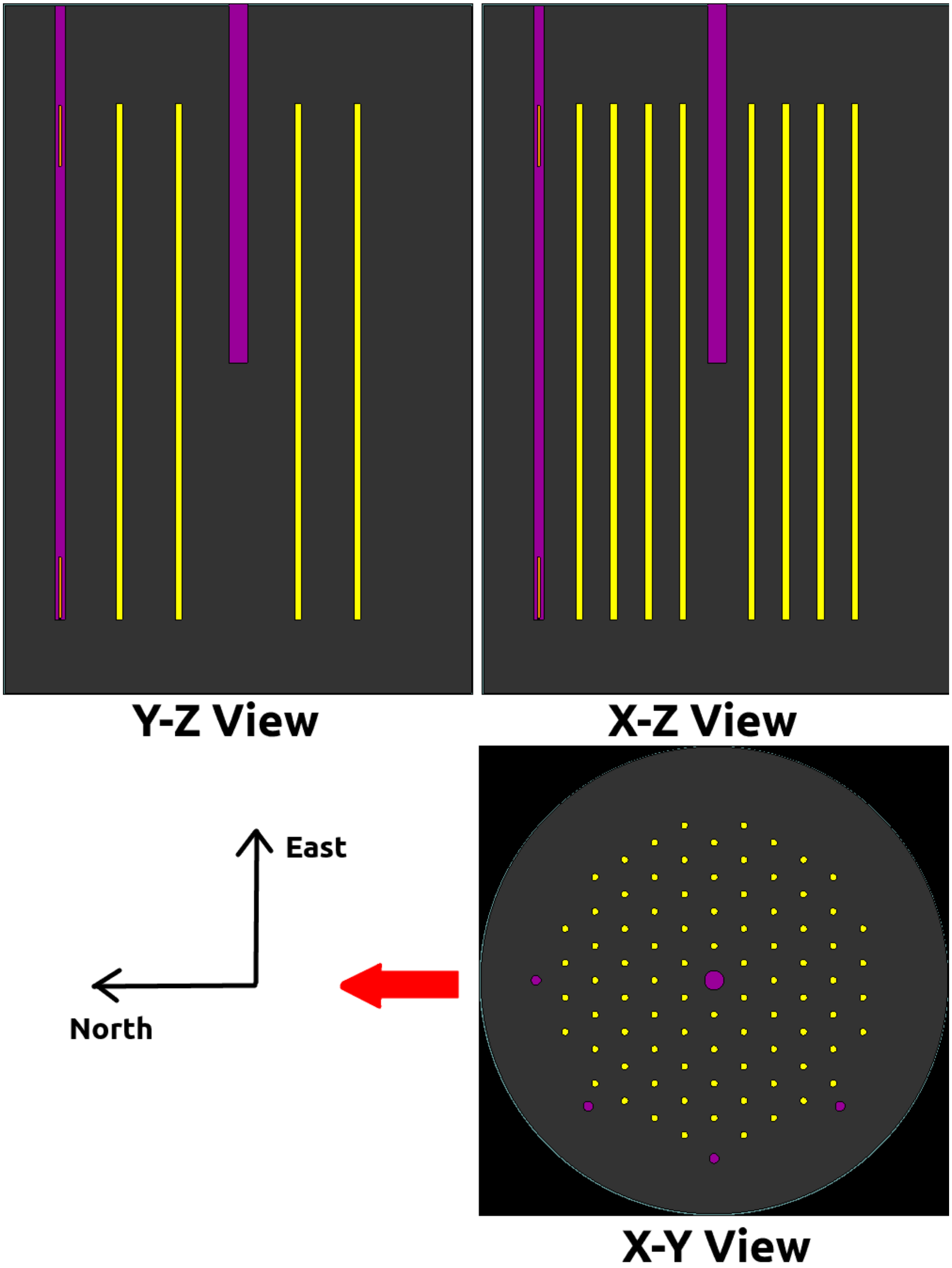

Figure 5.2: Serpent printed Geometry.

Helium-3 detectors, labeled as **He3_1**, **He3_3**, **He3_4**, **He3_6**, **He3_7**, **He3_9**, **He3_10** and **He3_12**, are positioned in the geometry as follow:

Table 5.1: Detectors positions.

Serpent identifier	Short name	Thimble	Position
He3_1	Det.1	North	Bottom
He3_3	Det.3	North	Top
He3_4	Det.4	North-West	Bottom
He3_6	Det.6	North-West	Top
He3_7	Det.7	West	Bottom
He3_9	Det.9	West	Top
He3_10	Det.10	South-West	Bottom
He3_12	Det.12	South-West	Top

5.7 Data Analysis

Since the main Serpent output files are in MATLAB format, MATLAB was used extensively for data analysis and plotting. Additionally, several MATLAB scripts were produced to modify Serpent's input files, submit runs, define the external neutron source shape, extrapolate salt density data, etc. A list of the main MATLAB scripts used in the analysis with a brief description of the function of each script is shown in table 5.2:

Table 5.2: List of the MATLAB scripts used in the analysis.

Script Name	**Details**
ExtractAnalyze.m	Fully analyze Serpent's raw outputs, and then generate output text files and plots.
INPSRCGEN.m	Prompt user to select the external neutron source operational mode (constant/pulsed), time-dependence (with/without), location of the point source, neutron emission-time profile, reactor run time, energy/relative yield angular profile of the DD source, etc. Then, it generates multiple Serpent input files, each with different material temperature, and a source definition file matching user's selection.

Chapter 6

Results

6.1 Static Continuous DD Source

First, the bias in detector readings due to the primary neutrons from the external DD neutron source was investigated. Using the **nphys** input card, the fission reaction mode was switched off. U-235 fission is treated as radiative capture. Total absorption cross section is preserved. This allows for the determination of the absorption rate in each helium-3 detector strictly from the source primary neutrons. The ratio between detector readings with and without fission neutrons production was computed at 750, 800, 850, 900 and 1000 K core isothermal temperature as shown in figure 6.1. This confirms the initial predictions that top detectors would experience a larger degree of source biasing due to the top reflector (see section 4.6). Additionally, the reduction in the density of the fuel salt with increasing temperature indeed increased source biasing from 1.5% to 2.6% for the top detectors, and from 1.2% to 2.1% for the bottom detectors.

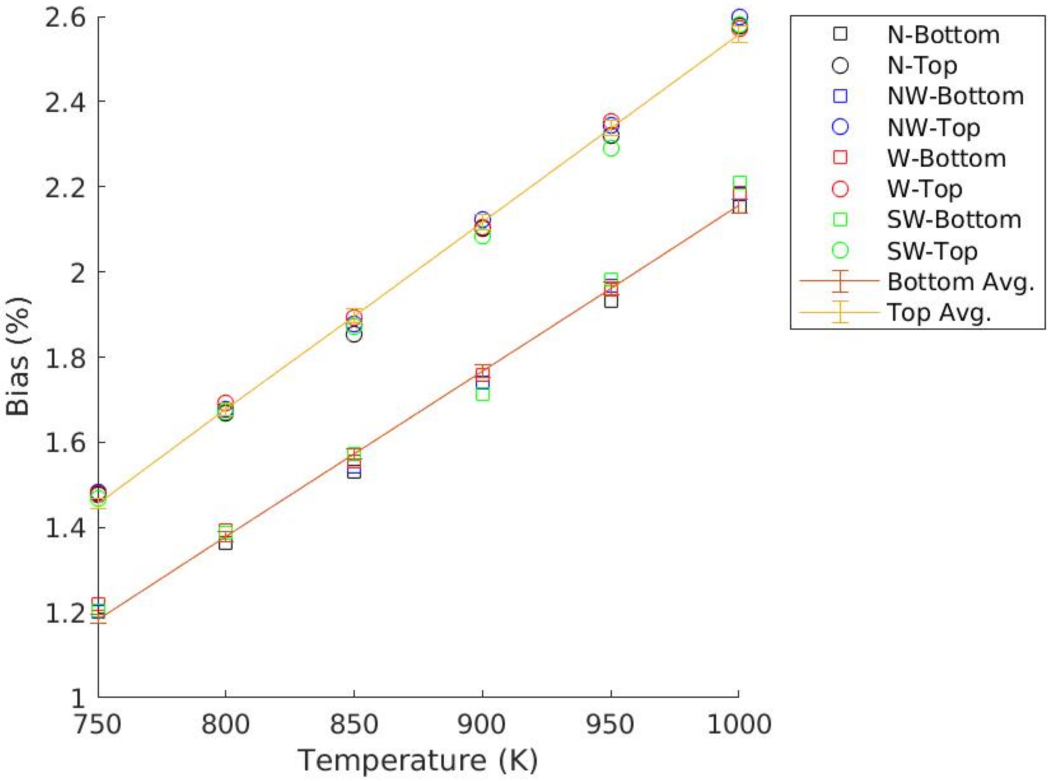

Figure 6.1: Bias profile with respect to temperature for each detector.

The k_{eff} profiles with respect to temperature with source bias were computed using equation (3.5). Serpent automatically produces k_{eff} values. Only the first k_{eff} value at 750 K was used to compute k_{eff} at 800 K, using equation (3.5). Next k_{eff} values were computed using detector readings and detector's computed k_{eff} values. The Serpent's and detector's computed k_{eff} values were compared as shown in figures 6.2, 6.3, 6.4 and 6.5:

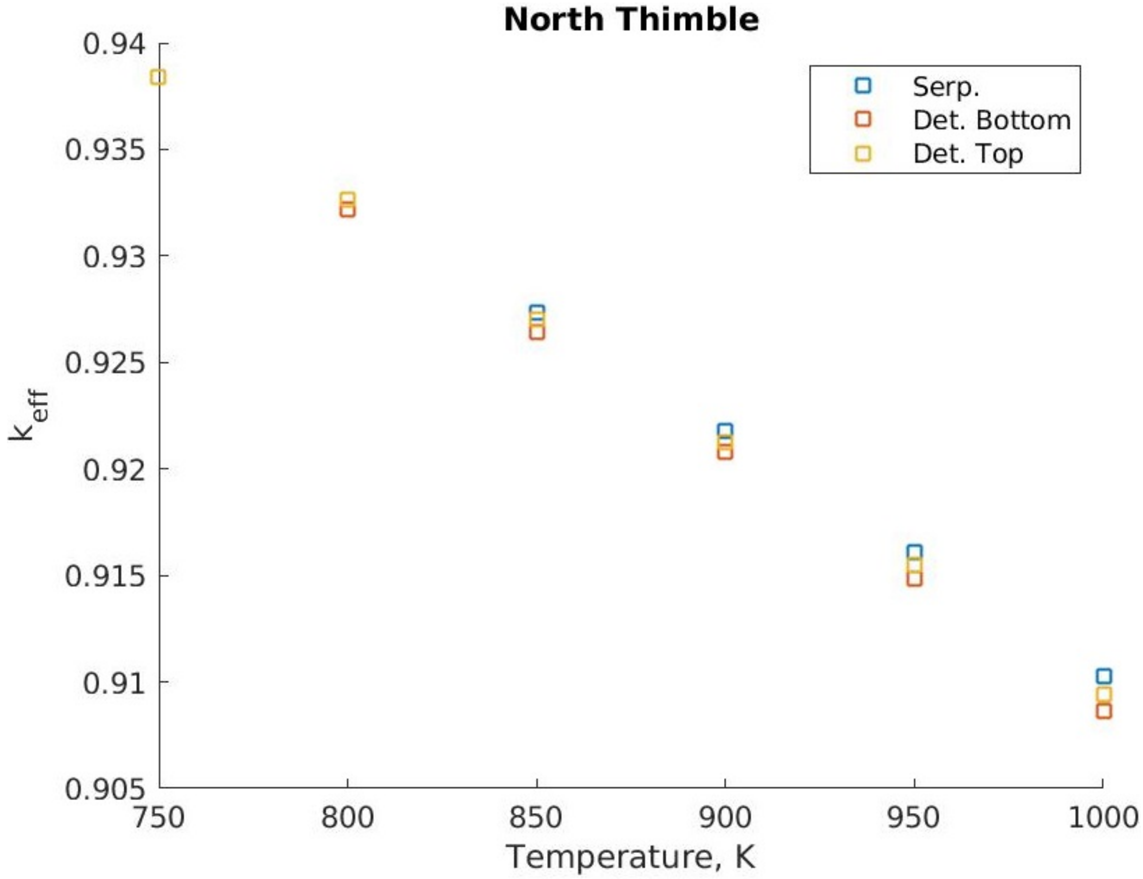

Figure 6.2: N thimble calculated k_{eff} profiles with respect to temperature (with bias) for the static source case.

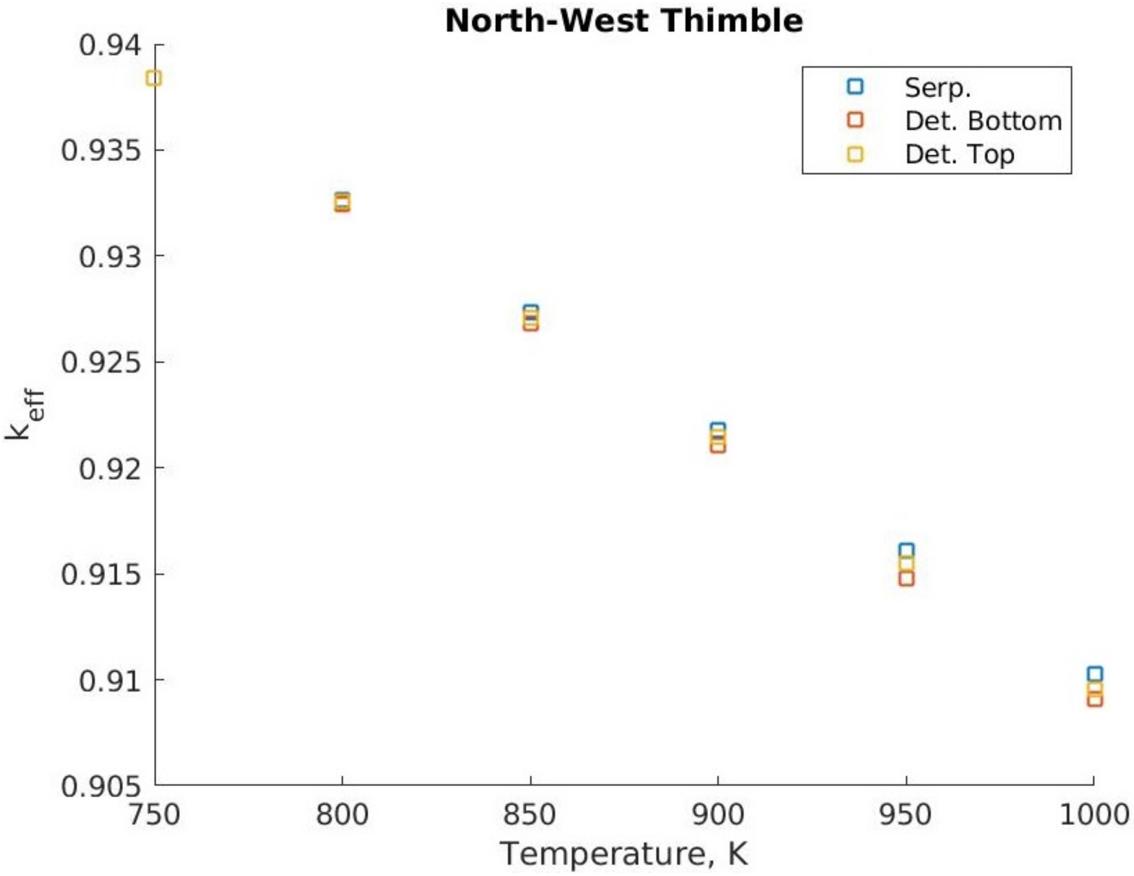

Figure 6.3: NW thimble calculated k_{eff} profiles with respect to temperature (with bias) for the static source case.

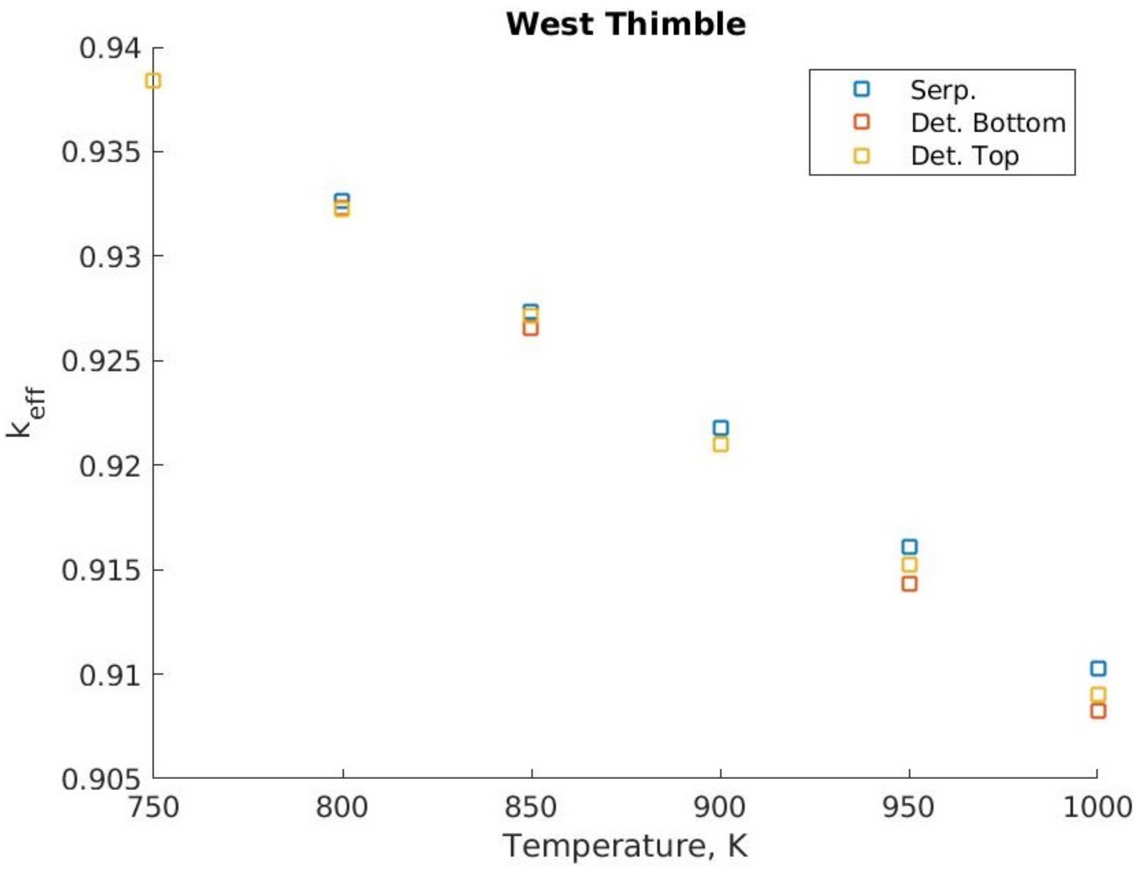

Figure 6.4: W thimble calculated k_{eff} profiles with respect to temperature (with bias) for the static source case.

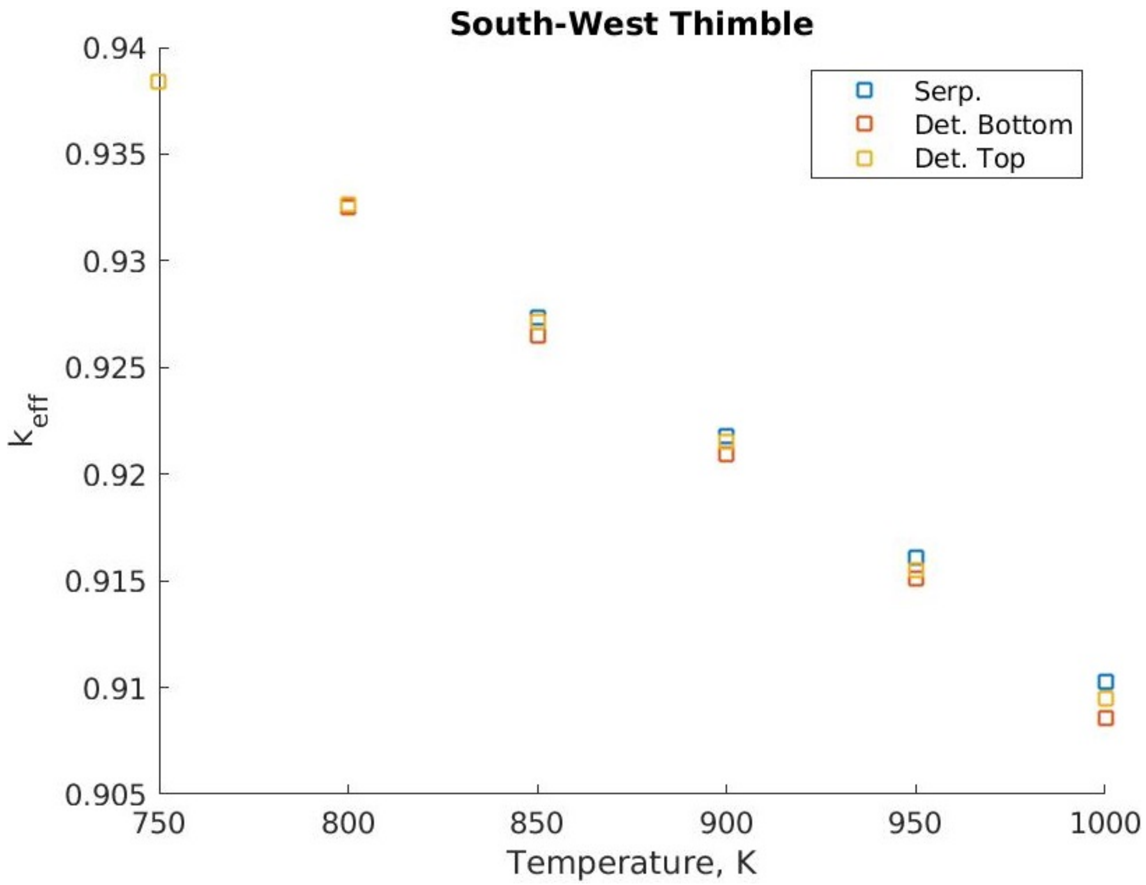

Figure 6.5: SW thimble calculated k_{eff} profiles with respect to temperature (with bias) for the static source case.

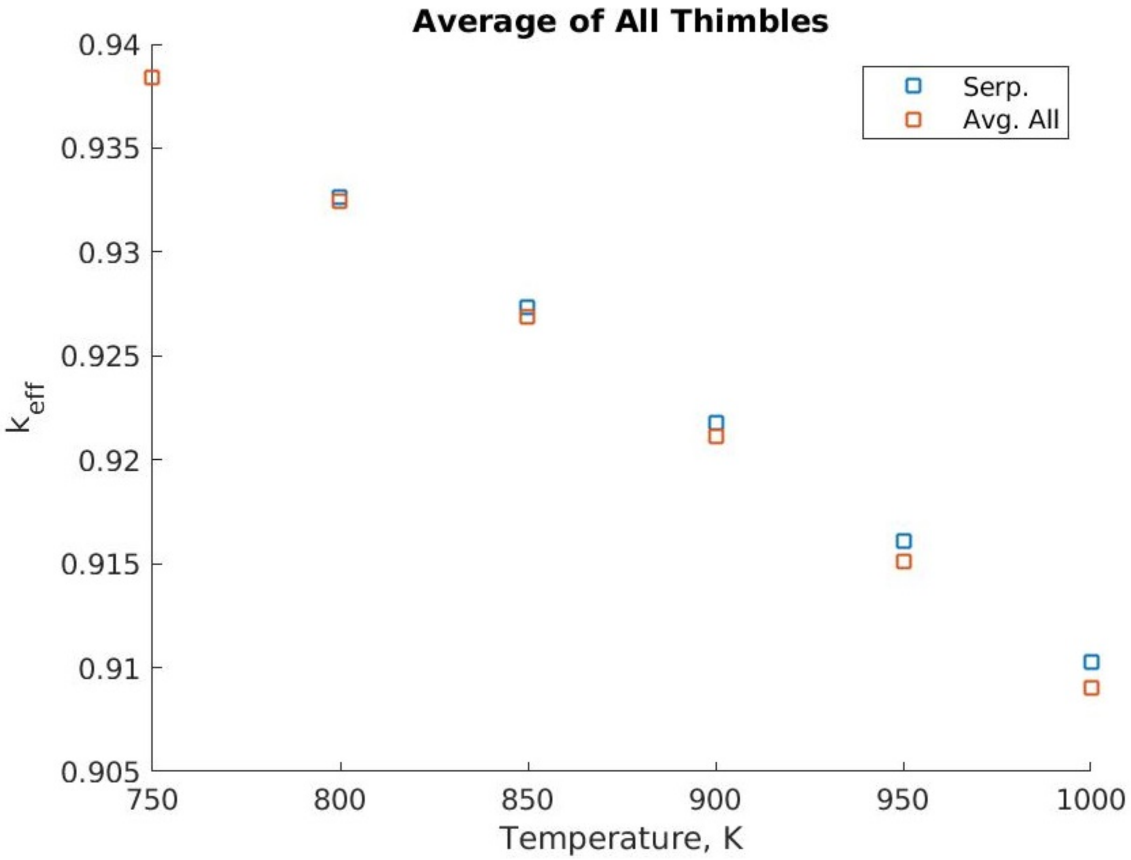

Figure 6.6: All thimbles average calculated k_{eff} profiles with respect to temperature (with bias) for the static source case.

In order to correct for source biasing, the bias fraction for each detector at each temperature is added to the detector readings as follow:

$$n_{corrected} = n_{biased}[1 - bias(det, T)] \tag{6.1}$$

The k_{eff} profiles with respect to temperature were reproduced after applying the source biasing corrections as shown in figures 6.7, 6.8, 6.9 and 6.10:

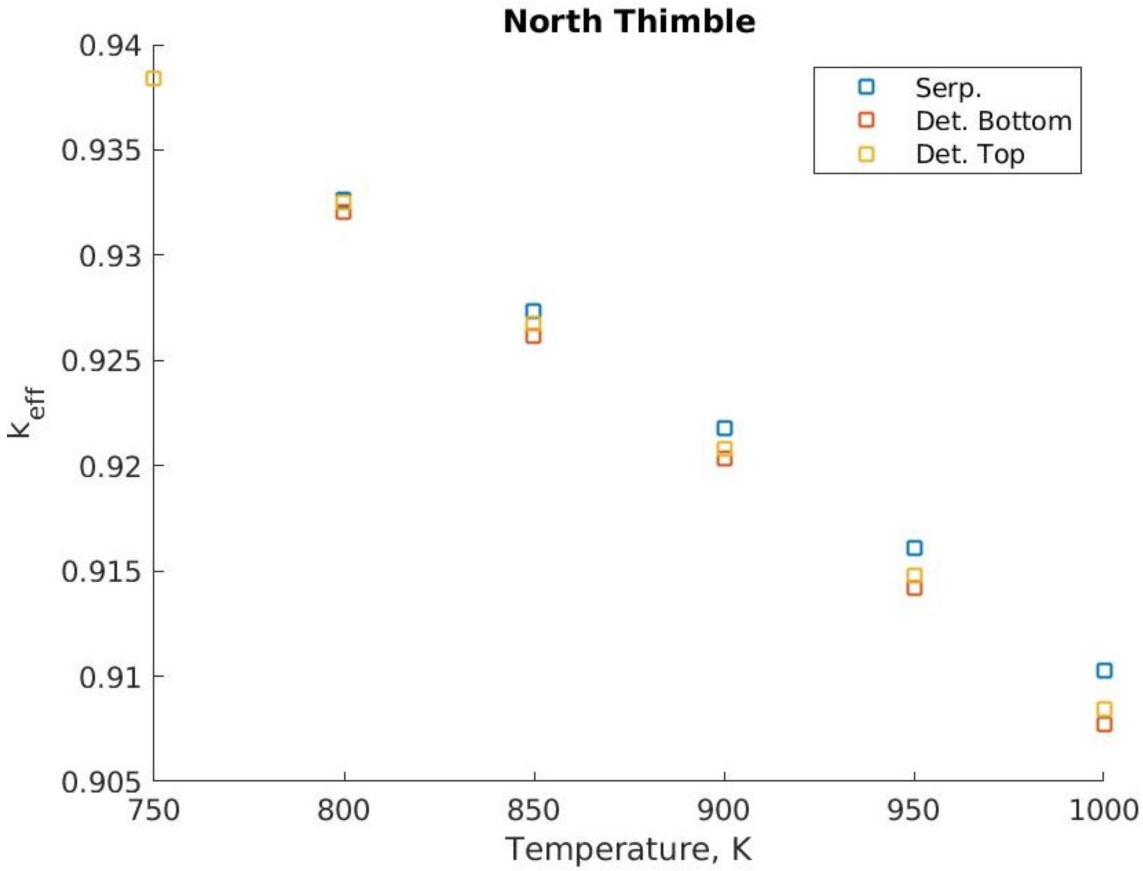

Figure 6.7: N thimble calculated k_{eff} profiles with respect to temperature for the static source case.

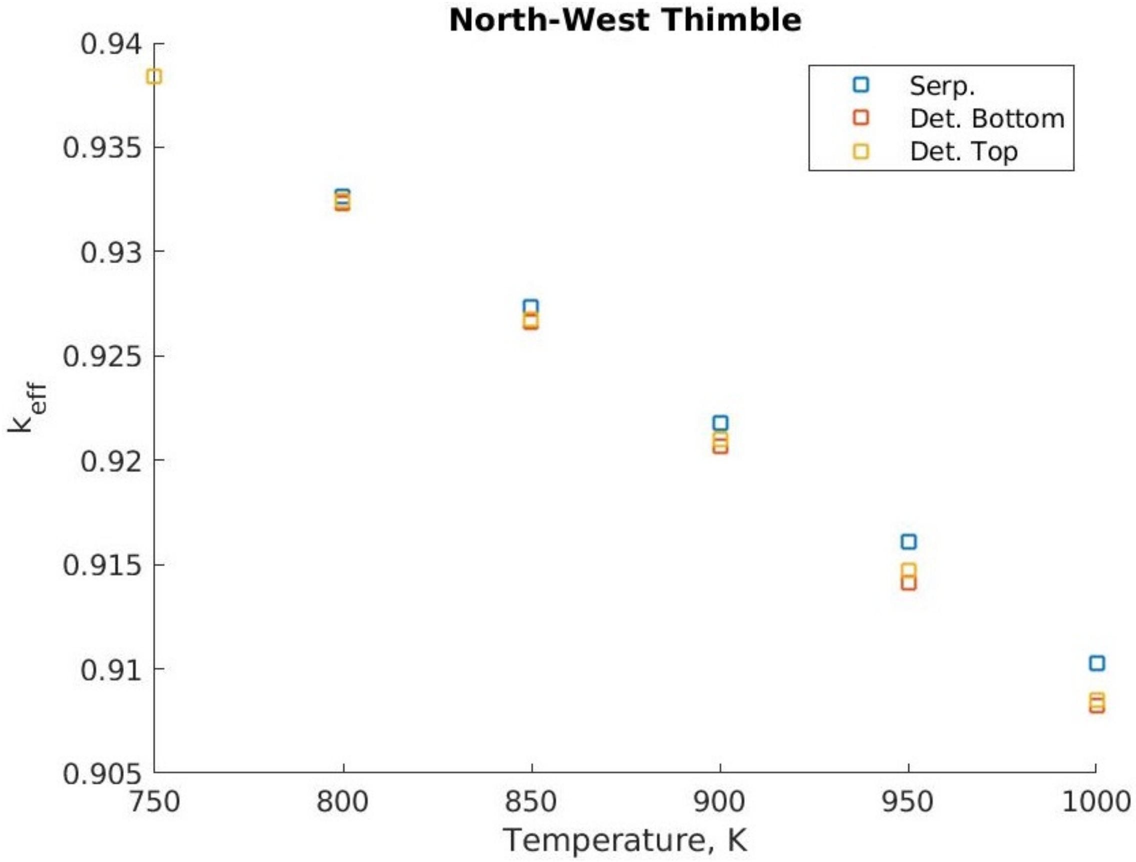

Figure 6.8: NW thimble calculated k_{eff} profiles with respect to temperature for the static source case.

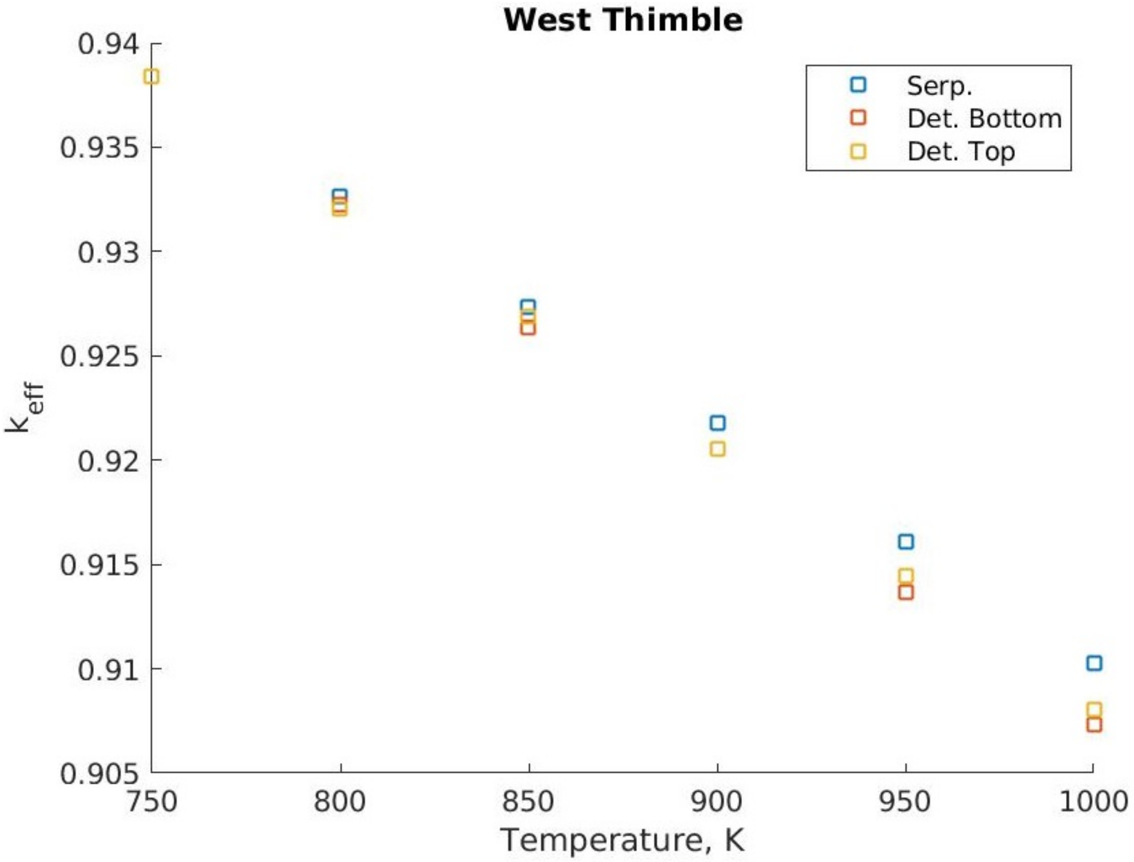

Figure 6.9: W thimble calculated k_{eff} profiles with respect to temperature for the static source case.

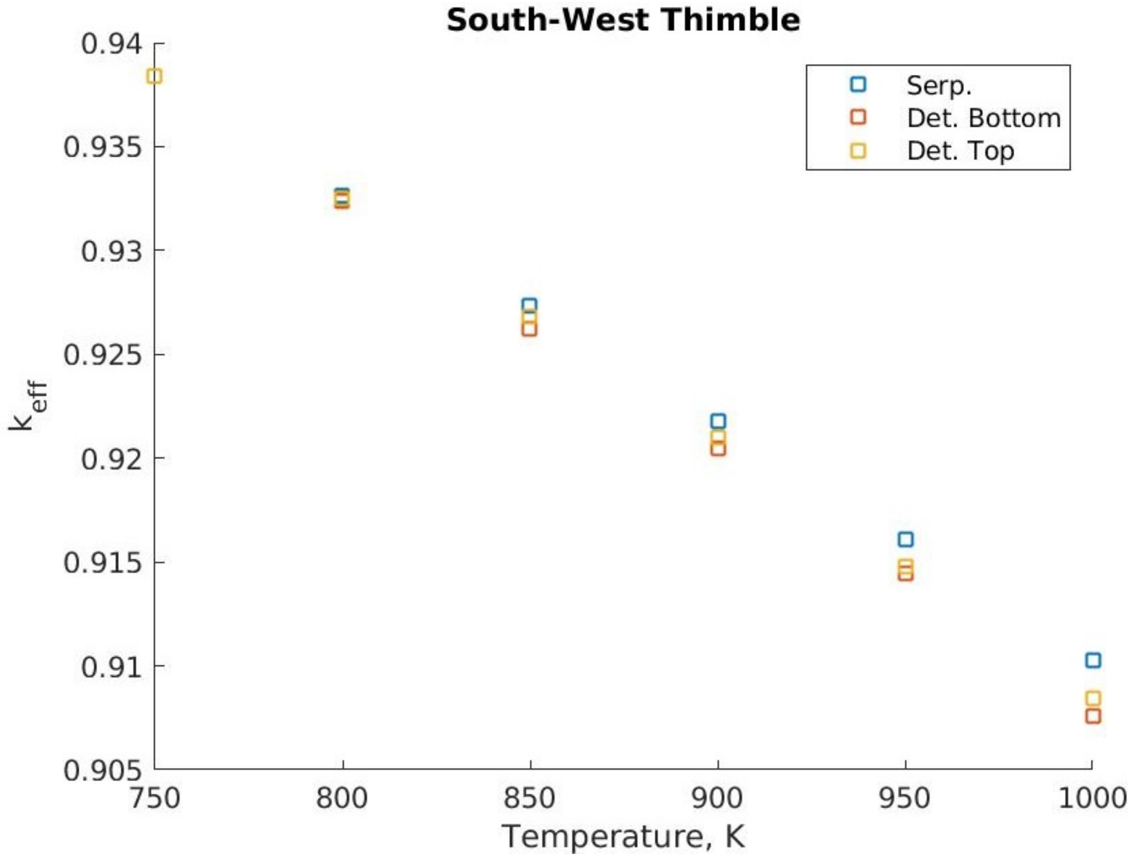

Figure 6.10: SW thimble calculated k_{eff} profiles with respect to temperature for the static source case.

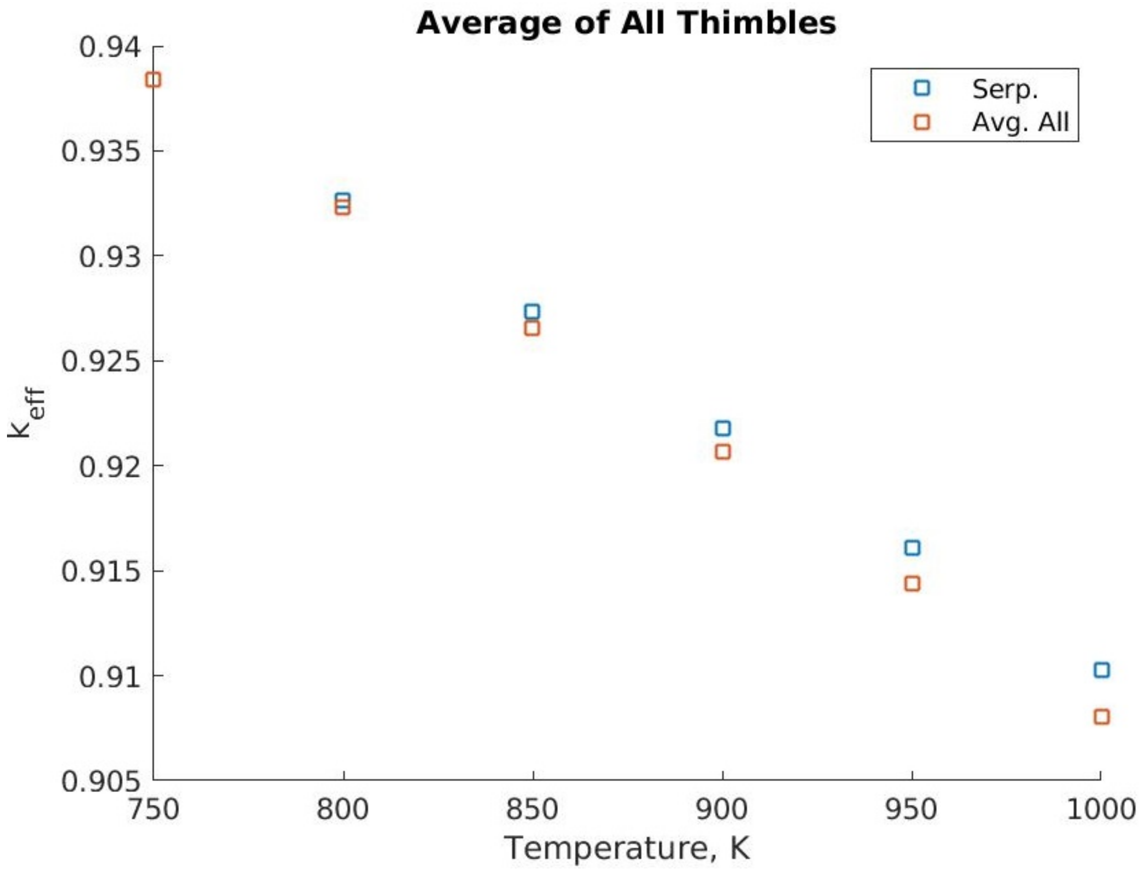

Figure 6.11: All thimbles average calculated k_{eff} profiles with respect to temperature for the static source case.

Comparing the bias-corrected results in figures 6.7, 6.8, 6.9 and 6.10 with the source-biased results in figures 6.2, 6.3, 6.4 and 6.5, it is possible to see that correcting for source biasing did not improve the accuracy of detectors' predictions of the k_{eff} profile. Therefore, it was decided to ignore the source biasing effect in the next calculations.

The Serpent's and detector's produced k_{eff} profiles with respect to temperature are displayed in table 6.1 along with computed errors for detector 6, which produced the most accurate predictions of the k_{eff}. Refer to table 5.1 for the location of each detector.

Table 6.1: k_{eff} profile with respect to temperature for each detector for the static source case.

T(K)	Serp.	Det1	Det3	Det4	Det6	Det7	Det9
750	0.938413	0.938413	0.938413	0.938413	0.938413	0.938413	0.938413
800	0.932628	0.932172	0.932637	0.932456	0.932591	0.932336	0.932216
850	0.927356	0.926425	0.927031	0.926850	0.927062	0.926588	0.927165
900	0.921778	0.920776	0.921280	0.921073	0.921485	0.921000	0.921010
950	0.916117	0.914827	0.915489	0.914769	0.915475	0.914330	0.915238
1000	0.910237	0.908613	0.909445	0.909120	0.909568	0.908239	0.909040
T(K)	Serp.	Det10	Det12	AVG	10σ %	$1 - n_2/n_1$ %	ϵ_{act} %
750	0.938413	0.938413	0.938413	0.938413	0.03	-	-
800	0.932628	0.932510	0.932632	0.932447	0.16	8.82	0.00
850	0.927356	0.926515	0.927122	0.926860	0.25	7.66	-0.03
900	0.921778	0.920912	0.921506	0.921141	0.33	7.32	-0.03
950	0.916117	0.915119	0.915470	0.915109	0.42	7.40	-0.07
1000	0.910237	0.908538	0.909468	0.909026	0.51	6.22	-0.07

The temperature here is the core isothermal, meaning that both graphite and fuel salt share the same temperature. The standard error (σ) was computed using the error propagation equation as follow:

$$\sigma_{k2} = \sqrt{\left(\frac{\partial k_2}{\partial k_1}\sigma_{k1}\right)^2 + \left(\frac{\partial k_2}{\partial n_1}\sigma_{n1}\right)^2 + \left(\frac{\partial k_2}{\partial n_2}\sigma_{n2}\right)^2} \tag{6.2}$$

Where the derivatives are that of equation 3.5. σ is then normalized by dividing σ by k_2. The error between Serpent's and detector's computed k_{eff} values (ϵ_{act}) was computed as follows:

$$\epsilon_{act} = \frac{k_{det} - k_{serp}}{k_{serp}} \tag{6.3}$$

Negative ϵ_{act} indicates that the k_{eff} value was underestimated by the detector reading, and vice-versa.

It can be observed from table 6.1 that the maximum absolute discrepancy between Serpent's and detector 6's computed k_{eff} values is 0.07% (i.e. 70 pcm). Also, 10σ is increasing due to error propagation (can be reduced by using more neutron histories). The maximum 10σ is 0.51% whereas the change in detector 6 readings (1-n_2/n_1) is between 6.22 and 8.82%. Therefore, the neutron signal change detectability condition in equation 4.2 was satisfied for static calculations.

Next, the total α_T was computed from Serpent's and detectors' data.

Table 6.2: α_T profile with respect to temperature for detector 6 and average all detector readings for the static source case.

T(K)	Serp. (pcm/K)	Det4 (pcm/K)	AVG (pcm/K)	ϵ_{act} %
750	-	-	-	-
800	-13.22	-13.31	-13.64	0.65
850	-12.19	-12.79	-12.93	4.91
900	-13.05	-13.06	-13.40	0.05
950	-13.41	-14.25	-14.31	6.27
1000	-14.10	-14.19	-14.63	0.60

The averages of α_T from Serpent and detector 6 readings are -13.19 and -13.52 pcm/K respectively. Hence, detector 6 readings underestimate the average α_T by 2.45%. The maximum error between Serpent's and detector 6's α_T values is 6.27%.

For the temperature range 900 to 1000 K, the total α_T was broken down to α_{mod}, α_{den} and α_{dopp}:

Table 6.3: α_T, α_{mod}, α_{den} and α_{dopp} values between 900 and 1000 K.

T_G(K)	T_S(K)	k_{eff}	α_{mod}(pcm/K)	α_{den}(pcm/K)	α_{dopp}(pcm/K)	α_T(pcm/K)
900	900	0.921778	-7.9	-4.0	-1.8	-13.8
1000	900	0.915079				
1000	1000d	0.911709				
1000	1000	0.910237				

Where T_G and T_S are the graphite and fuel salt temperatures respectively. The "1000d" entry of T_S corresponds to the fuel salt at 900 K, but the density is that of the fuel salt at 1000 K. Each row represents a separate Serpent simulation. The first and last rows describe the subcritical pile at 900 and 1000 K isothermal temperatures respectively. In the second simulation, the temperature of graphite was increased from 900 to 1000 K while the fuel salt was kept at 900 K. In the third simulation, only the density of the fuel salt was changed to the fuel salt density at 1000 K while the temperature of the composition was kept at 900 K. α_{mod} was calculated based on the first and second rows:

$$\alpha_{\text{mod}} = \frac{\frac{1}{k_1} - \frac{1}{k_2}}{1000\ K - 900\ K} = \frac{\frac{1}{0.921778} - \frac{1}{0.915079}}{1000\ K - 900\ K} = -7.9\ pcm/K$$

α_{den} was calculated based on the second and third rows:

$$\alpha_{\text{den}} = \frac{\frac{1}{k_2} - \frac{1}{k_3}}{1000\ K - 900\ K} = \frac{\frac{1}{0.915079} - \frac{1}{0.911709}}{1000\ K - 900\ K} = -4.0\ pcm/K$$

α_{dopp} was calculated based on the third and fourth rows:

$$\alpha_{\text{dopp}} = \frac{\frac{1}{k_3} - \frac{1}{k_4}}{1000\ K - 900\ K} = \frac{\frac{1}{0.911709} - \frac{1}{0.910237}}{1000\ K - 900\ K} = -1.8\ pcm/K$$

Based on table 6.3, the α_{mod} represents 57.6% of the negative temperature-reactivity effect. Next in magnitude is the α_{den} effect with 29.4%, and last is the α_{dopp} effect with 12.9%.

Hence, the total fuel effect (i.e. α_{prompt}) is 42.4% or 5.8 pcm/K. Even if the negative magnitude of α_{mod} is reduced due to plutonium isotopes build-up, α_{prompt} is negative enough for the reactor to remain dynamically stable.

6.2 Dynamic Fluctuating DD Source

As explained in subsection 5.5.2, the source output is forced into sinusoidal fluctuation by source definition. According to Seidi *et al.* [2014], sinusoidal behavior is an appropriate mathematical representation of a most neutron sources, hence, it was implemented. Dynamic external neutron source calculations were performed for 0, 1 and 2% source output fluctuations in order to determine whether or not the feasibility condition (see equation (4.2)) would still be satisfied even with source fluctuation.

6.2.1 0% Source Fluctuation

At 0% source fluctuation, detector readings were integrated over the total reactor run time of 600 seconds. Then, the k_{eff} profiles with respect to temperature were produced after applying the source biasing corrections (see section 6.1) as shown in figures 6.12, 6.13, 6.14 and 6.15:

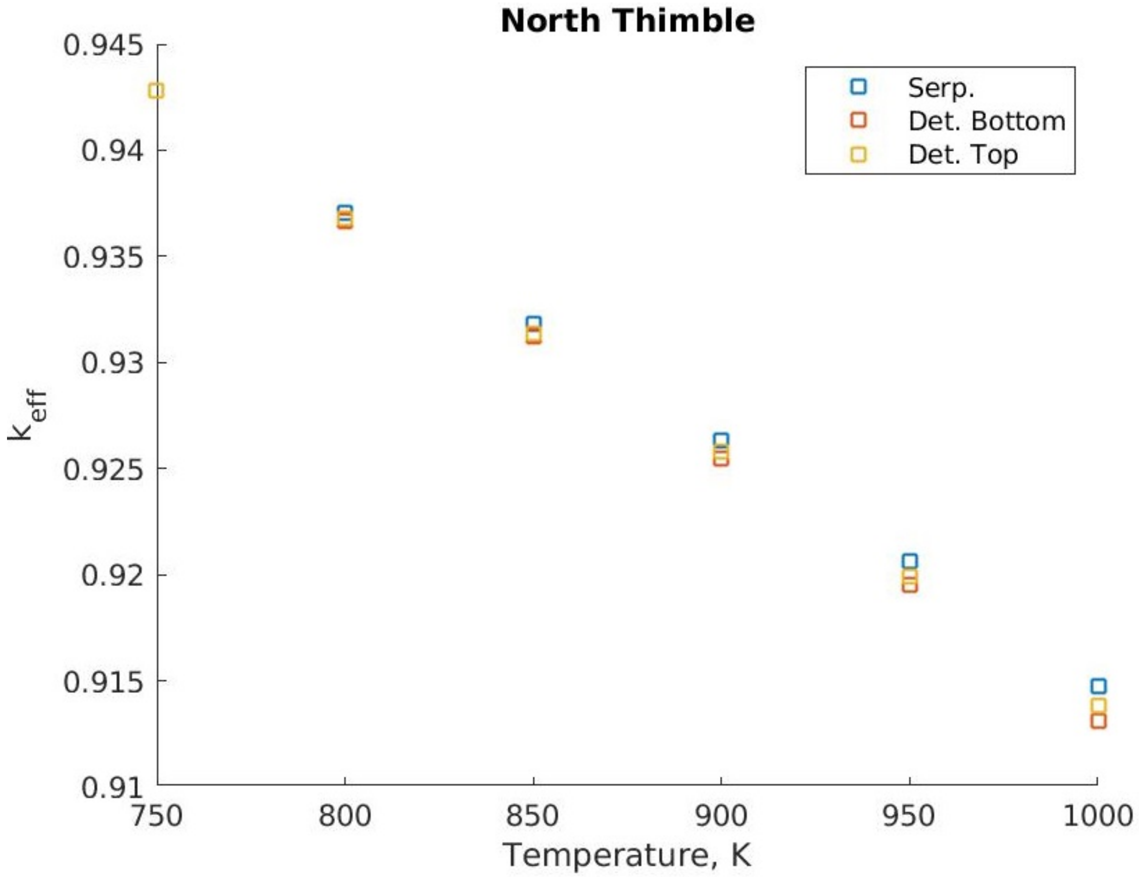

Figure 6.12: N thimble calculated k_{eff} profiles with respect to temperature for the 0% fluctuating source case.

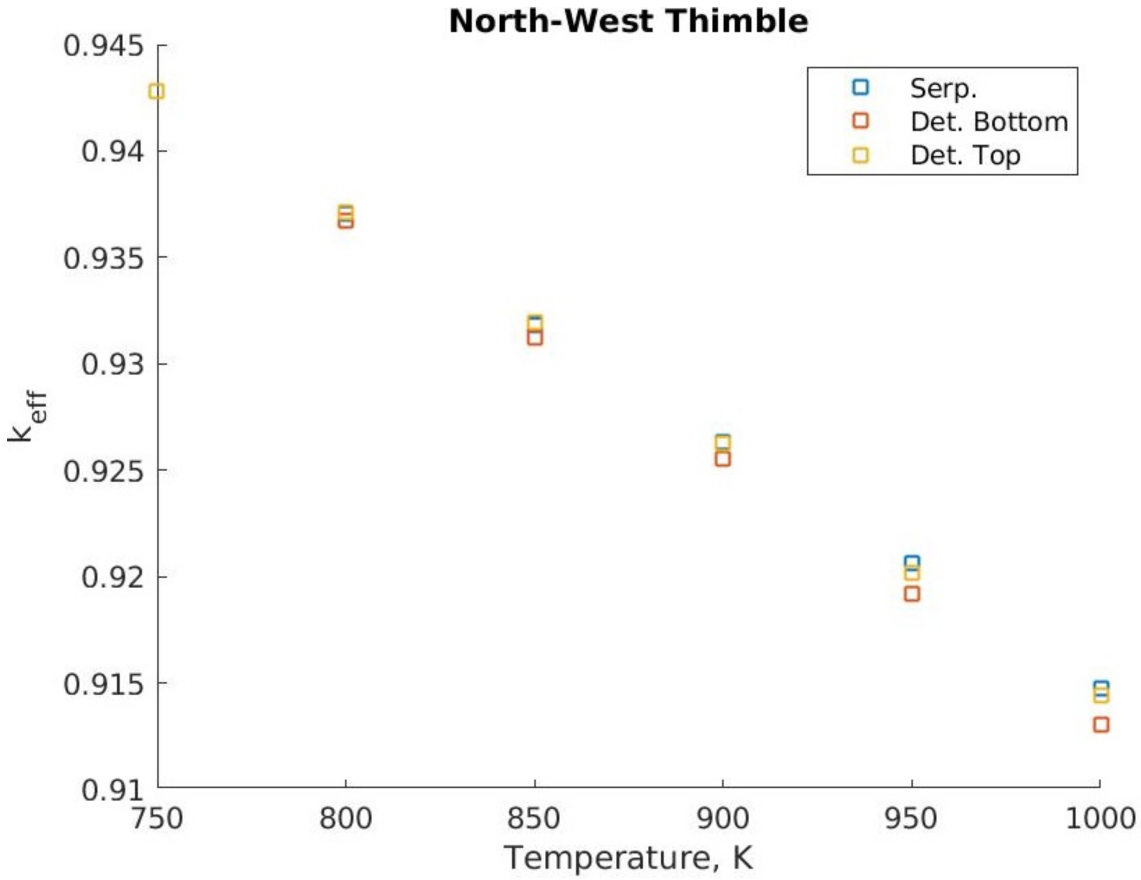

Figure 6.13: NW thimble calculated k_{eff} profiles with respect to temperature for the 0% fluctuating source case.

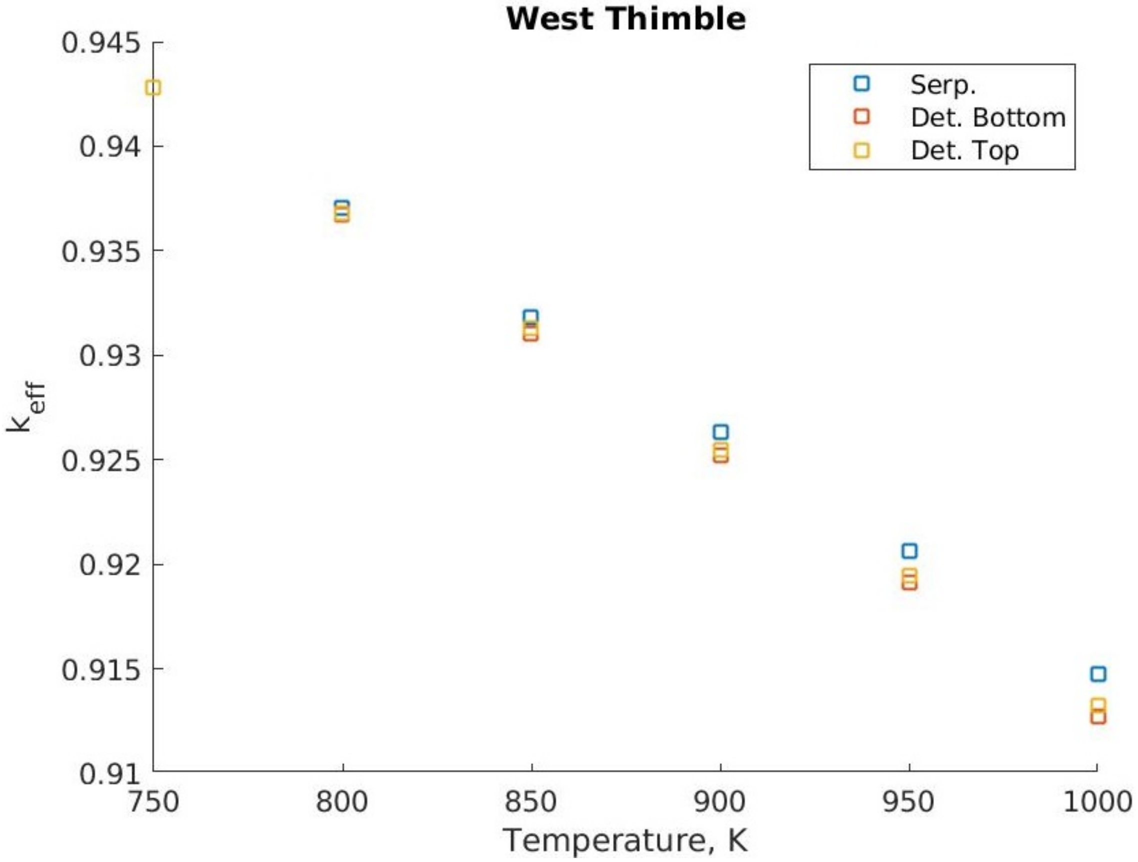

Figure 6.14: W thimble calculated k_{eff} profiles with respect to temperature for the 0% fluctuating source case.

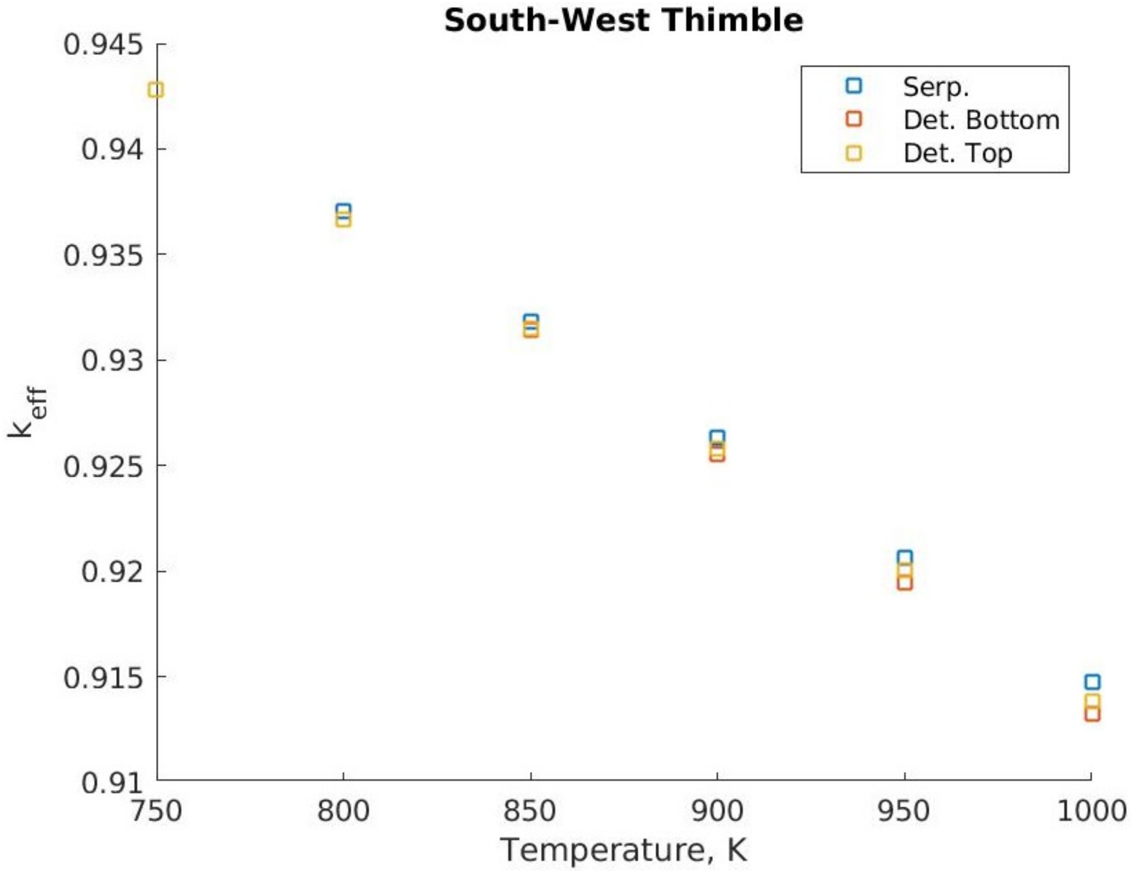

Figure 6.15: SW thimble calculated k_{eff} profiles with respect to temperature for the 0% fluctuating source case.

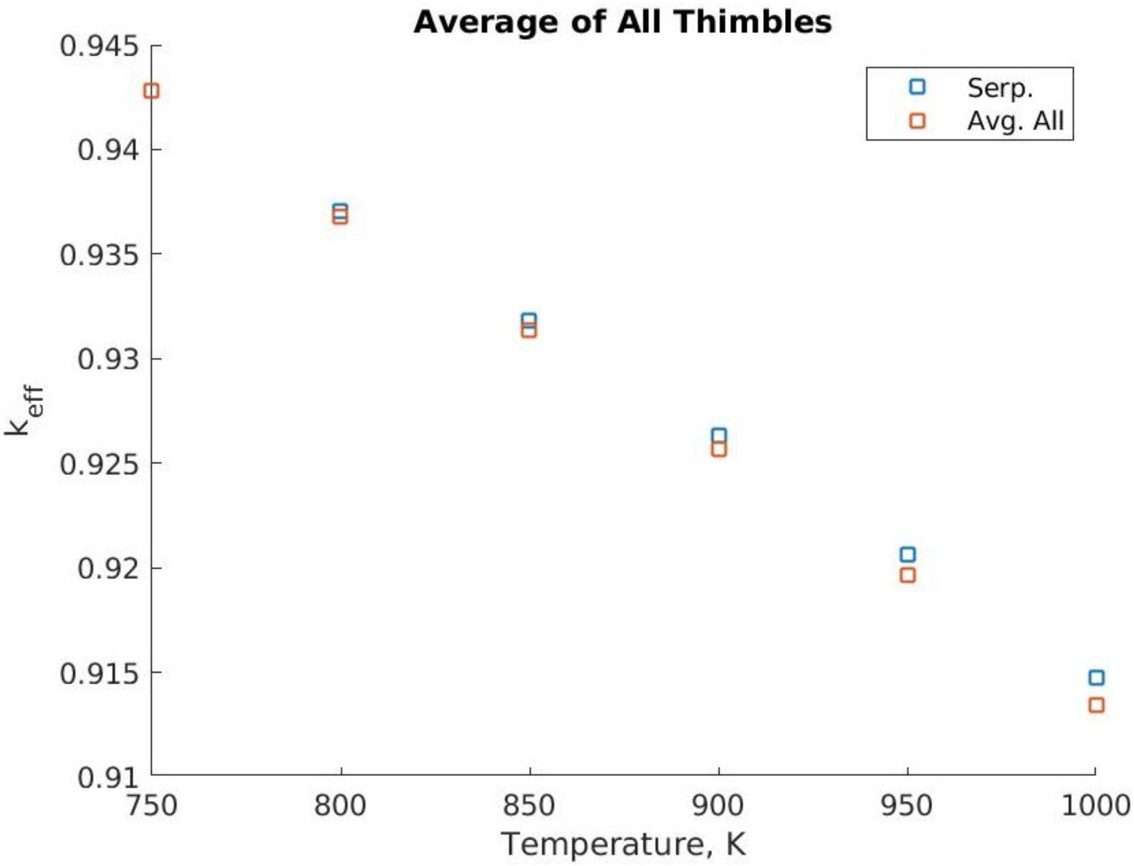

Figure 6.16: All thimbles average calculated k_{eff} profiles with respect to temperature for the 0% fluctuating source case.

The Serpent's, detector 6's and detectors' averaged produced k_{eff} profiles with respect to temperature are displayed in table 6.4 along with computed errors:

Table 6.4: k_{eff} profile with respect to temperature for each detector for the 0% fluctuating source case.

T(K)	Serp.	Det4	AVG	10σ %	$1 - n_2/n_1$ %	ϵ_{act} %
750	0.942823	0.942823	0.942823	0.00	-	-
800	0.937059	0.937114	0.936769	0.51	9.67	0.01
850	0.931825	0.931930	0.931380	0.80	7.93	0.01
900	0.926304	0.926232	0.925642	1.09	7.70	-0.01
950	0.920635	0.920149	0.919630	1.40	7.82	-0.05
1000	0.914739	0.914390	0.913429	1.72	7.12	-0.04

Comparing with the results in table 6.1, it can be observed that the k_{eff} values are off by +0.05 on average. This is due to the automatic disabling of delayed neutrons emission in the static mode. However, this should not have any impact on the predictions of the α_T as will be shown.

It can be observed from table 6.4 that the maximum absolute discrepancy between Serpent's and detector 6's computed k_{eff} values is 0.05% (i.e. 50 pcm). Also, the maximum 10σ is 1.72% whereas the change in detector 6 readings (1-n_2/n_1) is between 7.12 and 9.67%. Therefore, the neutron signal change detectability condition in equation 4.2 was satisfied for the dynamic mode with 0% source output fluctuations.

Next, the total α_T was computed from Serpent's and detector's data.

Table 6.5: α_T profile with respect to temperature for detector 6 and average all detector readings for the 0% fluctuating source case.

T(K)	Serp. (pcm/K)	Det4 (pcm/K)	AVG (pcm/K)	ϵ %
750	-	-	-	-
800	-13.05	-12.92	-13.71	-0.96
850	-11.99	-11.87	-12.35	-0.98
900	-12.79	-13.20	-13.31	3.20
950	-13.30	-14.28	-14.12	7.37
1000	-14.00	-13.69	-14.76	-2.23

The average of α_T from Serpent and detector 6 readings are -13.03 and -13.19 pcm/K respectively. Hence, detector 6 readings overestimate the average α_T by 1.28%. The maximum error between Serpent's and detector 6's α_T values is 7.37%.

6.2.2 1% Source Fluctuation

At 1% source fluctuation, detector readings were integrated over the total reactor run time of 600 seconds. Then, the k_{eff} profiles with respect to temperature were produced after applying the source biasing corrections (see section 6.1) as shown in figures 6.17, 6.18, 6.19 and 6.20:

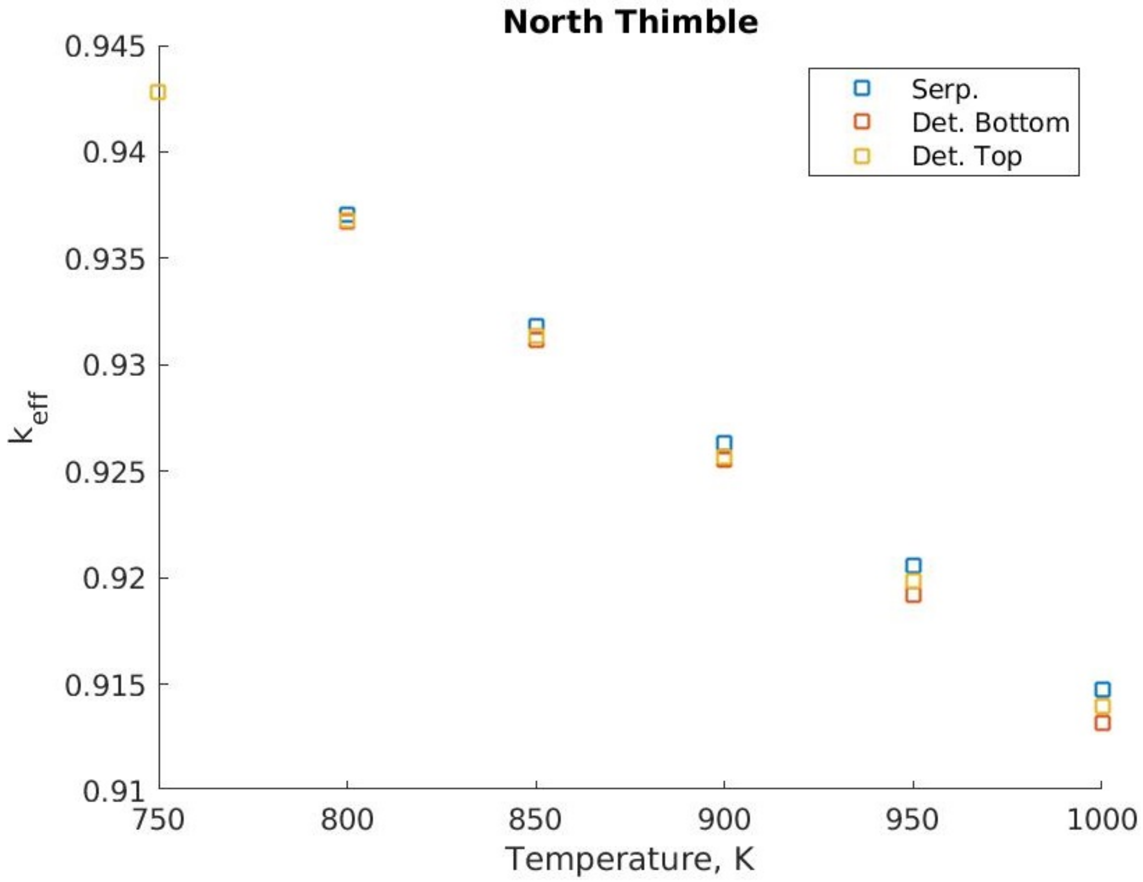

Figure 6.17: N thimble calculated k_{eff} profiles with respect to temperature for the 1% fluctuating source case.

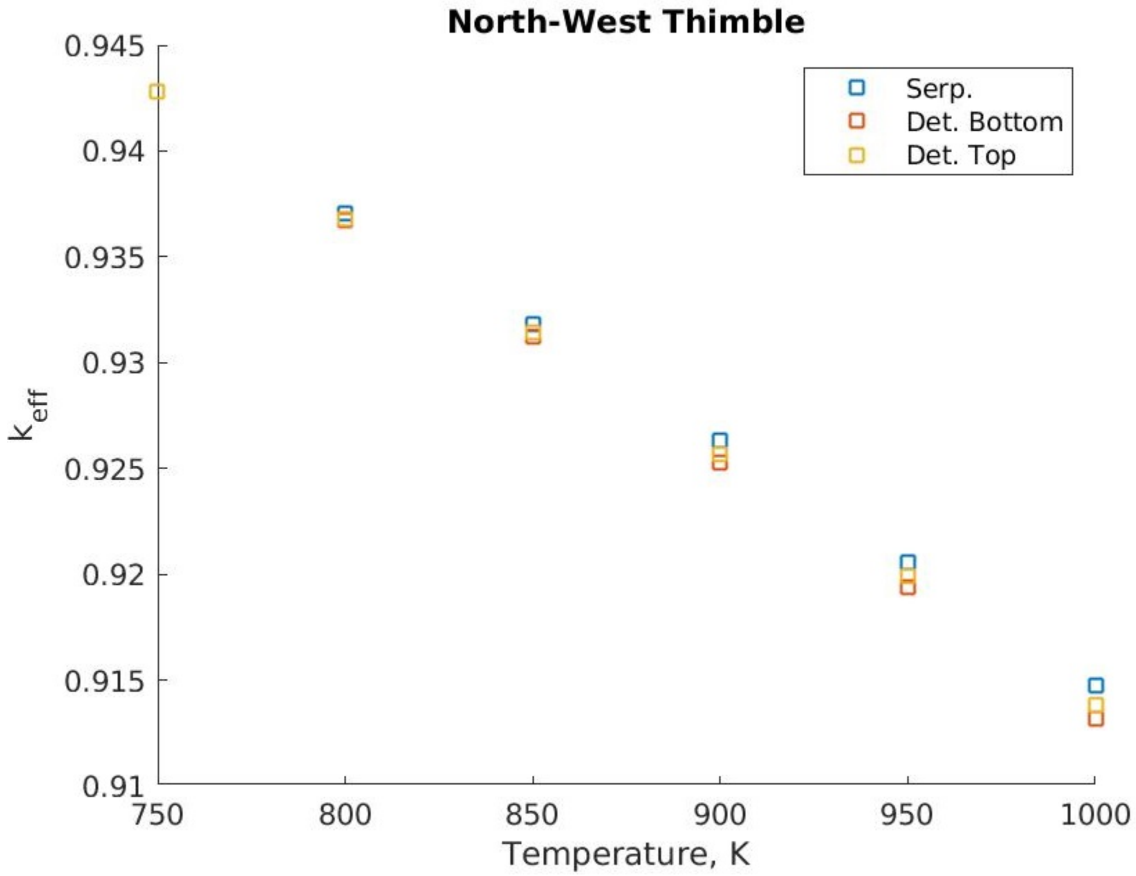

Figure 6.18: NW thimble calculated k_{eff} profiles with respect to temperature for the 1% fluctuating source case.

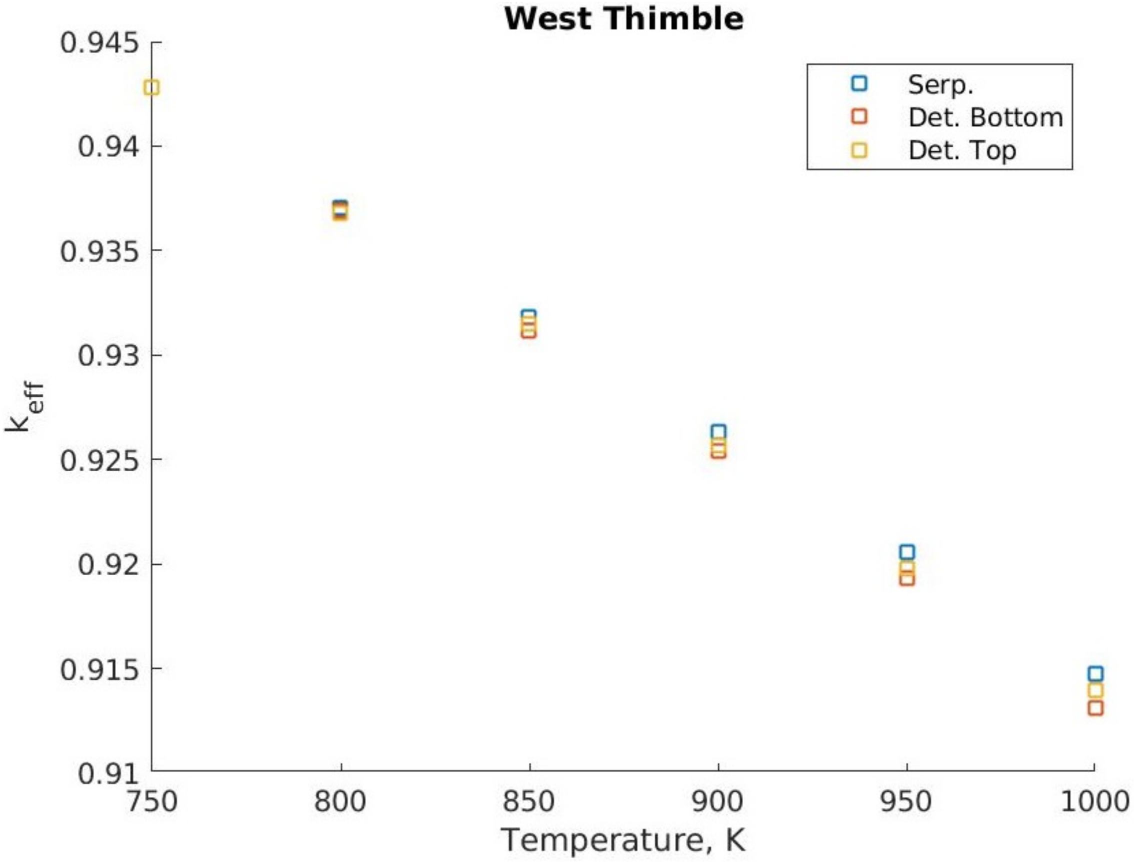

Figure 6.19: W thimble calculated k_{eff} profiles with respect to temperature for the 1% fluctuating source case.

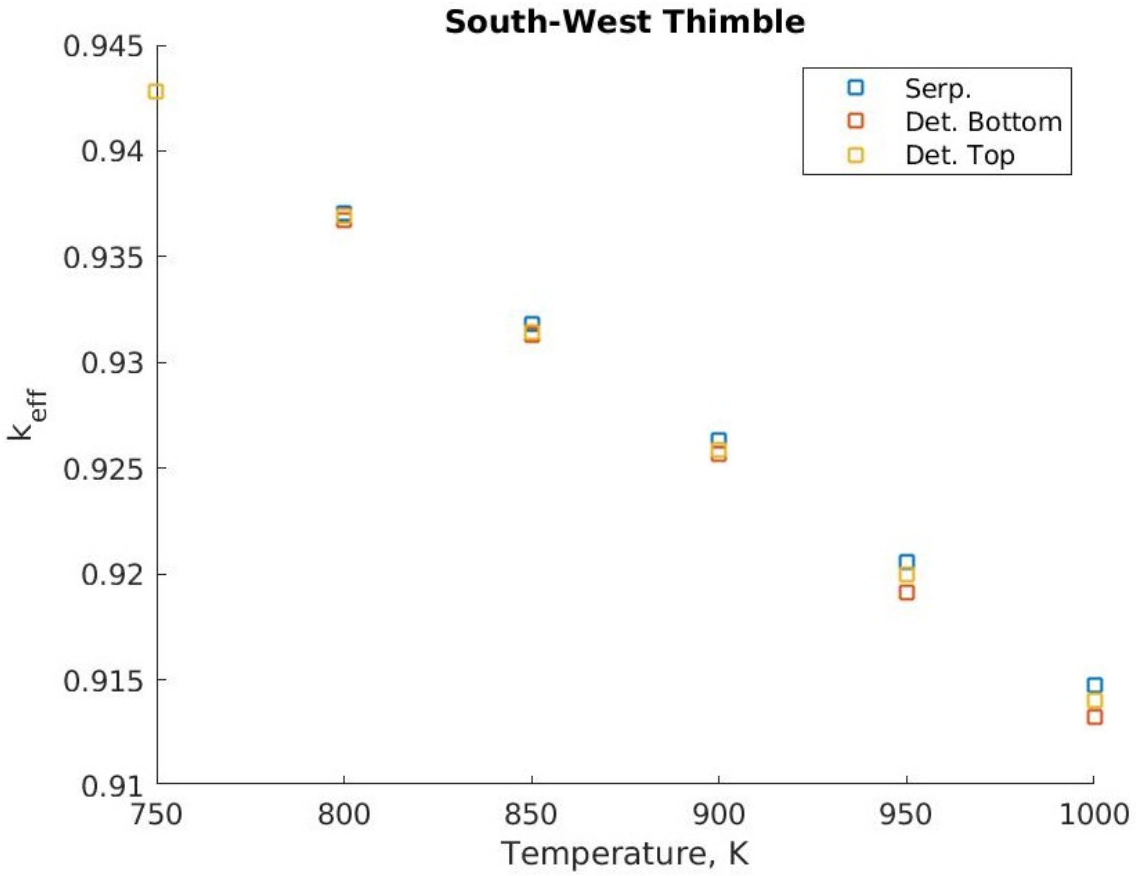

Figure 6.20: SW thimble calculated k_{eff} profiles with respect to temperature for the 1% fluctuating source case.

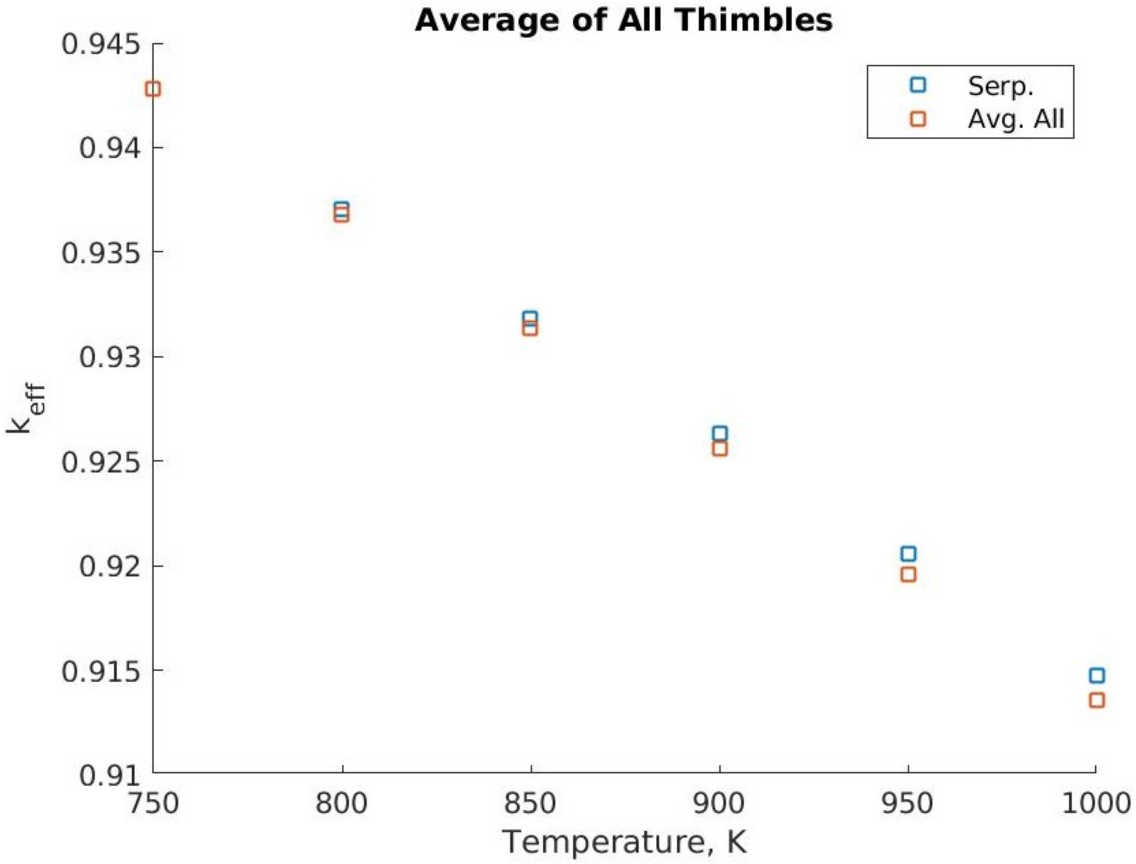

Figure 6.21: All thimbles average calculated k_{eff} profiles with respect to temperature for the 1% fluctuating source case.

The Serpent's, detector 6's and detectors averaged produced k_{eff} profiles with respect to temperature are displayed in table 6.6 along with computed errors:

Table 6.6: k_{eff} profile with respect to temperature for each detector for the 1% fluctuating source case.

T(K)	Serp.	Det4	AVG	10σ %	$1 - n_2/n_1$ %	ϵ_{act} %
750	0.942800	0.942800	0.942800	0.00	-	-
800	0.937034	0.936764	0.936785	0.51	9.64	-0.03
850	0.931809	0.931419	0.931330	0.80	7.92	-0.04
900	0.926296	0.925642	0.925609	1.09	7.98	-0.07
950	0.920540	0.919935	0.919592	1.38	7.28	-0.07
1000	0.914744	0.913825	0.913563	1.71	7.23	-0.10

It can observed from table 6.6 that the maximum absolute discrepancy between Serpent's and detector 6's computed k_{eff} values is 0.10% (i.e. 100 pcm). Also, the maximum 10σ is 1.71% whereas the change in detector 6 readings (1-n_2/n_1) is between 7.23 and 9.64%. Therefore, the neutron signal change detectability condition in equation 4.2 was satisfied for the dynamic mode with 1% source output fluctuations.

Next, the total α_T was computed from Serpent's, detector 6's and detectors' averaged data.

Table 6.7: α_T profile with respect to temperature detector 6 and average all detector readings for the 1% fluctuating source case.

T(K)	Serp. (pcm/K)	Det4 (pcm/K)	AVG (pcm/K)	ϵ %
750	-	-	-	-
800	-13.05	-13.67	-13.62	4.71
850	-11.97	-12.25	-12.51	2.37
900	-12.77	-13.40	-13.27	4.91
950	-13.50	-13.40	-14.14	-0.72
1000	-13.77	-14.54	-14.35	5.60

The average of α_T from Serpent and detector 6 readings are -13.01 and -13.45 pcm/K respectively. detector 6 readings underestimate the average α_T by 3.38%. The maximum error between Serpent's and detector 6's α_T values is 5.60%.

6.2.3 2% Source Fluctuation

At 2% source fluctuation, detector readings were integrated over the total reactor run time of 600 seconds. Then, the k_{eff} profiles with respect to temperature were produced after applying the source biasing corrections (see section 6.1) as shown in figures 6.22, 6.23, 6.24 and 6.25:

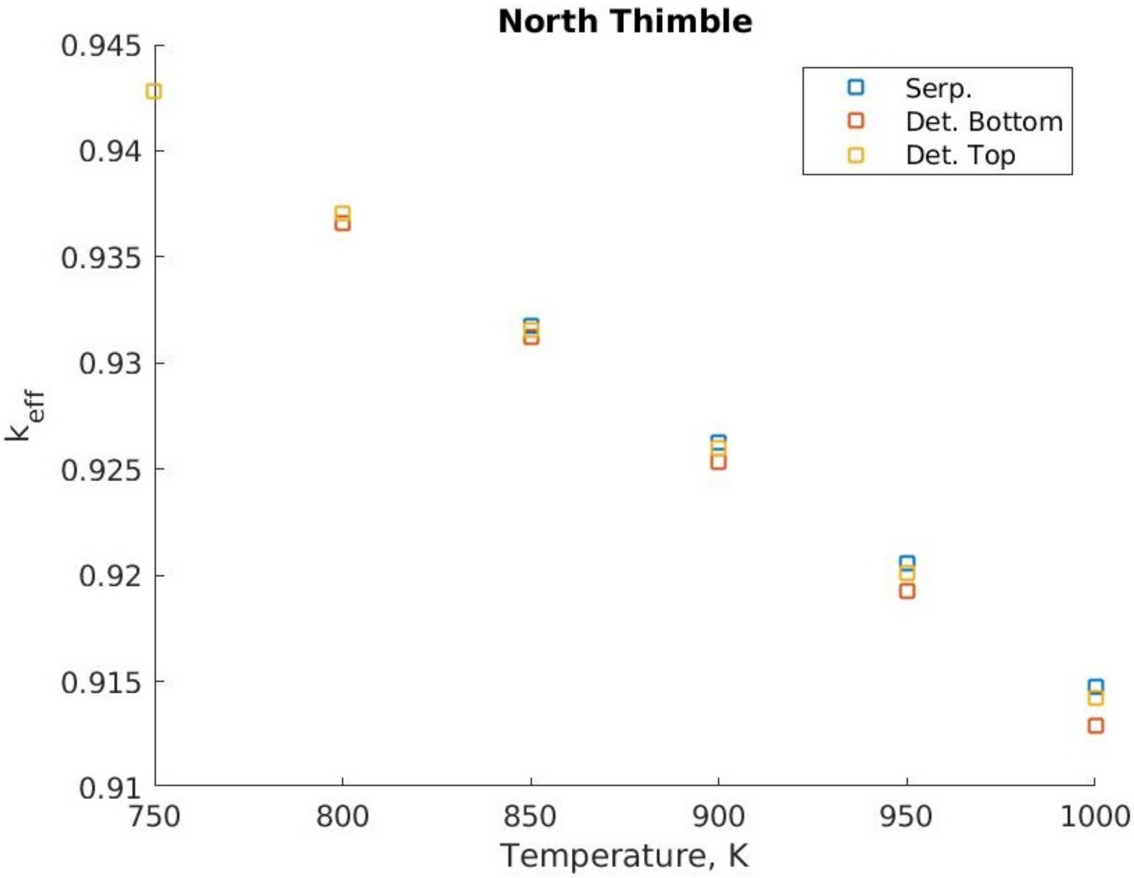

Figure 6.22: N thimble calculated k_{eff} profiles with respect to temperature for the 2% fluctuating source case.

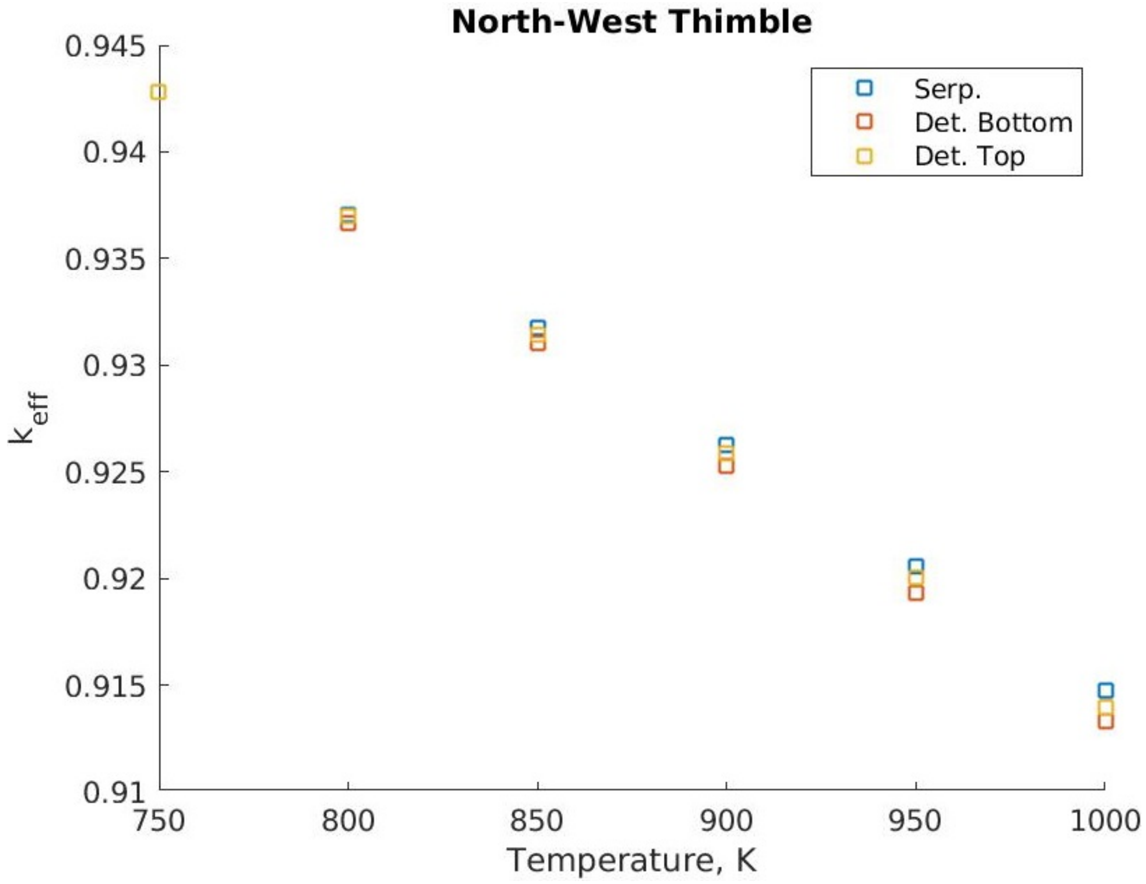

Figure 6.23: NW thimble calculated k_{eff} profiles with respect to temperature for the 2% fluctuating source case.

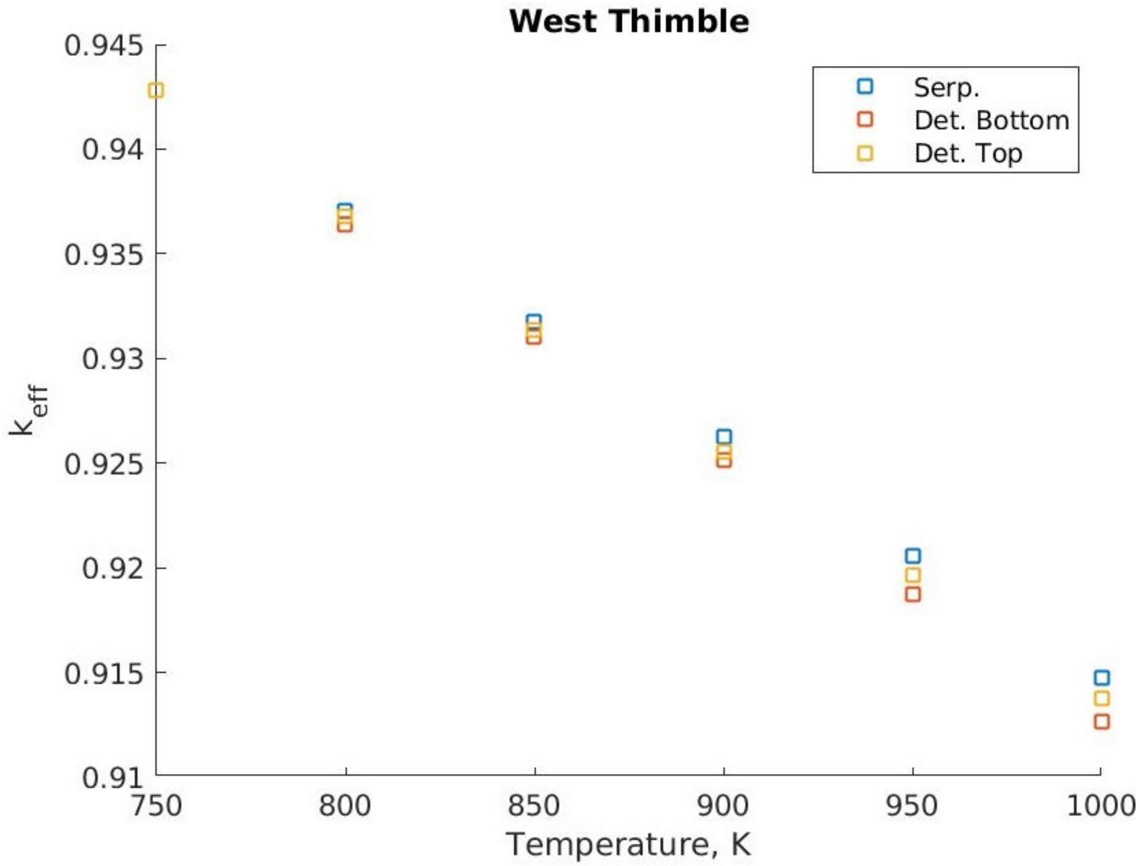

Figure 6.24: W thimble calculated k_{eff} profiles with respect to temperature for the 2% fluctuating source case.

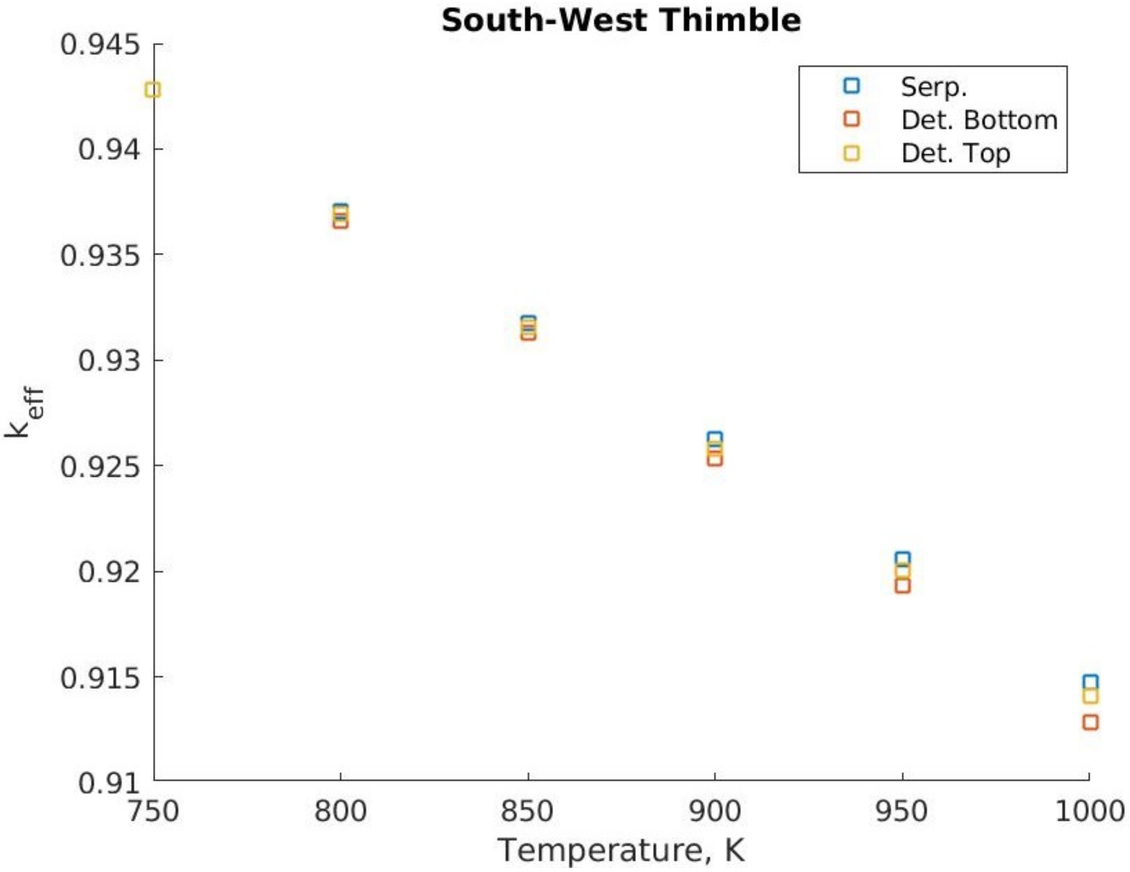

Figure 6.25: SW thimble calculated k_{eff} profiles with respect to temperature for the 2% fluctuating source case.

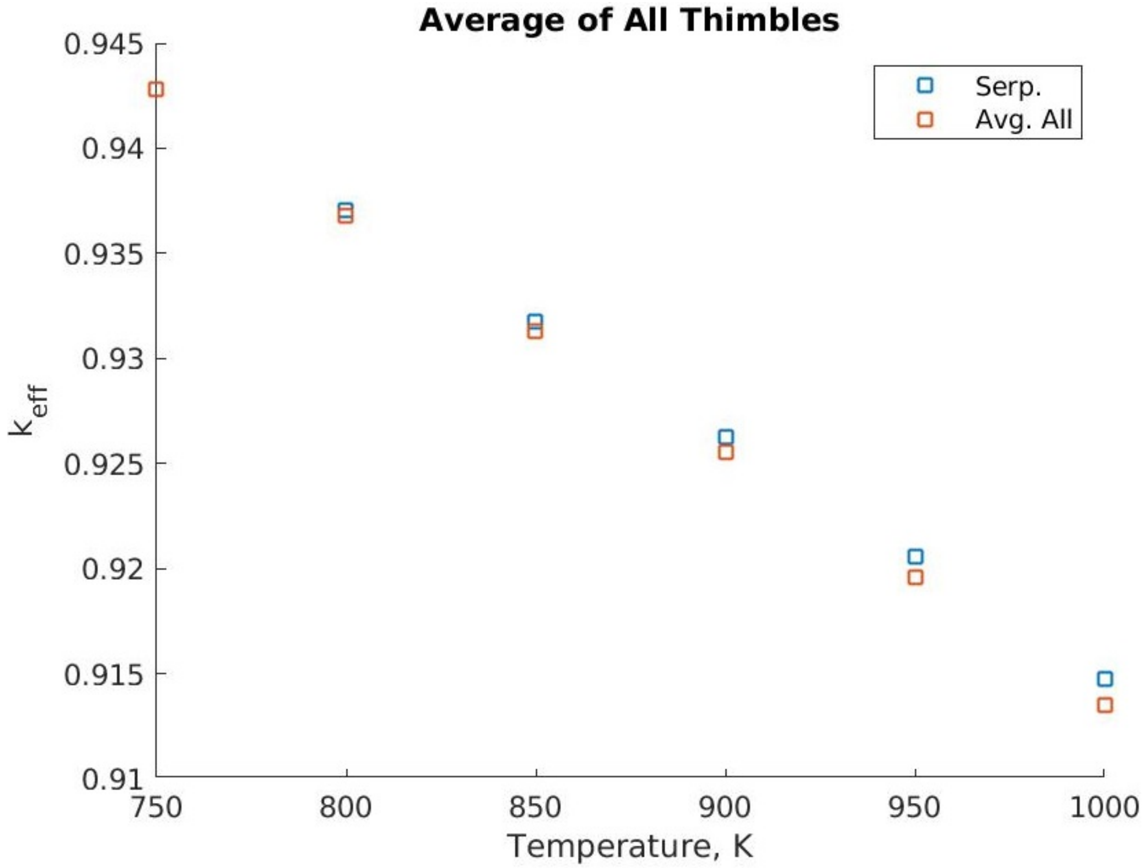

Figure 6.26: All thimbles average calculated k_{eff} profiles with respect to temperature for the 2% fluctuating source case.

The Serpent's, detector 6's and detectors' averaged produced k_{eff} profiles with respect to temperature are displayed in table 6.6 along with computed errors:

Table 6.8: k_{eff} profile with respect to temperature for each detector for the 2% fluctuating source case.

T(K)	Serp.	Det4	AVG	10σ %	$1 - n_2/n_1$ %	ϵ_{act} %
750	0.942823	0.942803	0.942803	0.00	-	-
800	0.937059	0.936967	0.936762	0.53	9.66	-0.01
850	0.931825	0.931449	0.931325	0.82	8.22	-0.04
900	0.926304	0.925857	0.925553	1.11	7.68	-0.05
950	0.920635	0.920045	0.919588	1.40	7.36	-0.06
1000	0.914739	0.913982	0.913505	1.72	6.92	-0.08

It can observed from table 6.8 that the maximum absolute discrepancy between Serpent's and detector 6's computed k_{eff} values is 0.08% (i.e. 80 pcm). Also, the maximum 10σ is 1.72% whereas the change in detector 6 readings (1-n_2/n_1) is between 6.92 and 9.66%. Therefore, the neutron signal change detectability condition in equation 4.2 was satisfied for the dynamic mode with 2% source output fluctuations.

Next, the total α_T was computed from Serpent's, detector 6's and detectors' averaged data.

Table 6.9: α_T profile with respect to temperature detector 6 and average all detector readings for the 2% fluctuating source case.

T(K)	Serp. (pcm/K)	Det4 (pcm/K)	AVG (pcm/K)	ϵ %
750	-	-	-	-
800	-13.06	-13.21	-13.68	1.19
850	-12.03	-12.64	-12.46	5.14
900	-12.74	-12.97	-13.39	1.78
950	-13.40	-13.64	-14.02	1.85
1000	-13.82	-14.42	-14.48	4.37

The average of α_T from Serpent and detector 6 readings are -13.01 and -13.38 pcm/K respectively. Hence, detector 6 readings underestimate the average α_T by 2.85%. The maximum error between Serpent's and detector 6's α_T values is 5.14%.

6.3 Dynamic Pulsed DD Source

The simulation of the pulsed neutron test was done as described in section 5.5.2. Detector tallies were setup for the total fission power of the core and the absorption reaction rate in detectors 3 and 6. By adding pulse profiles of each response tally, the accumulated pulse profiles with respect to the time duration of a single pulse are as follow:

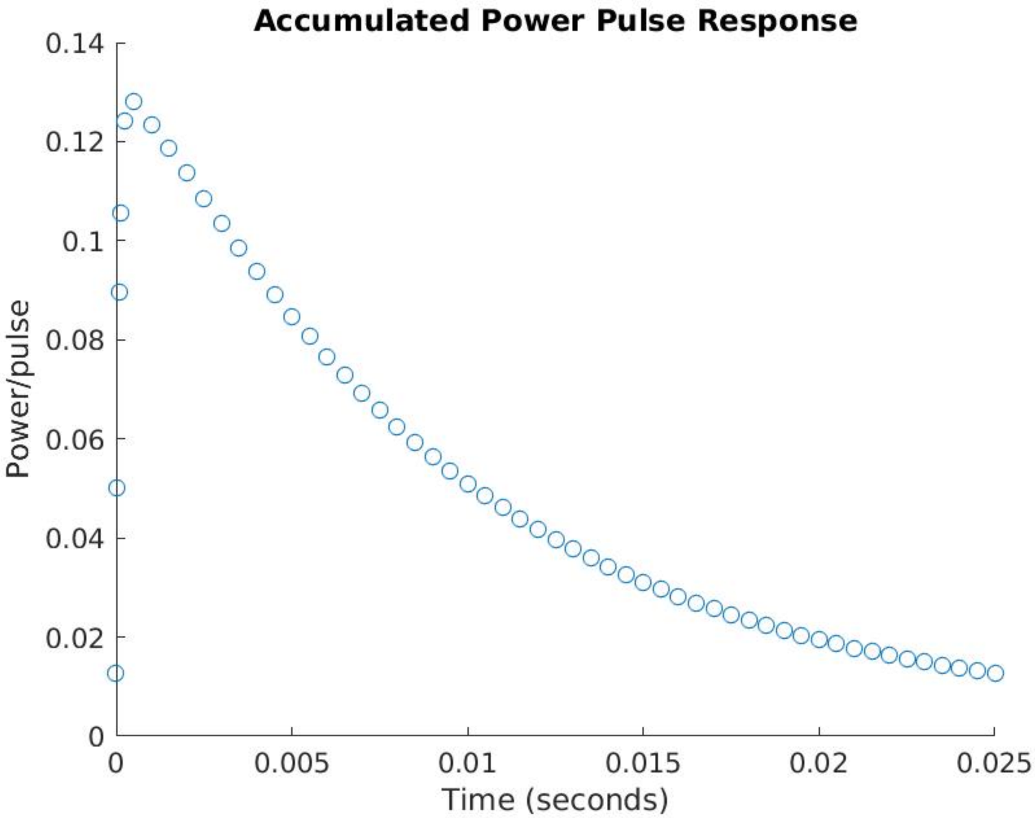

Figure 6.27: Accumulated power pulse profile with respect to time.

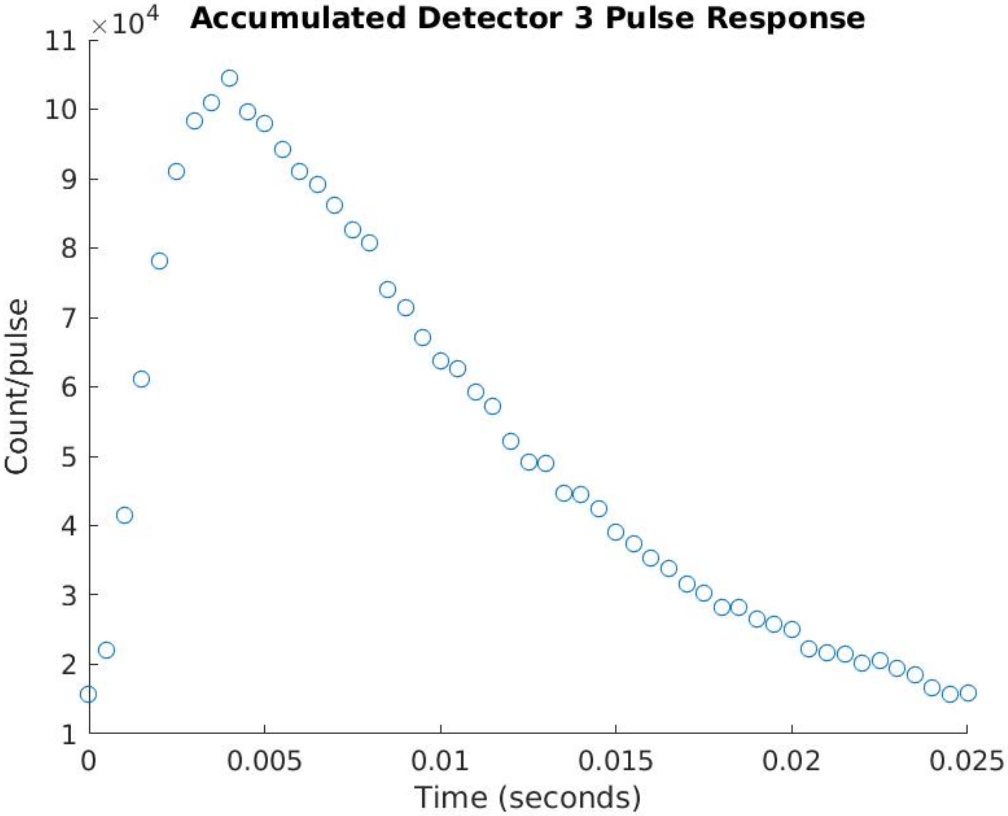

Figure 6.28: Helium-3 detector 3 accumulated count pulse profile with respect to time.

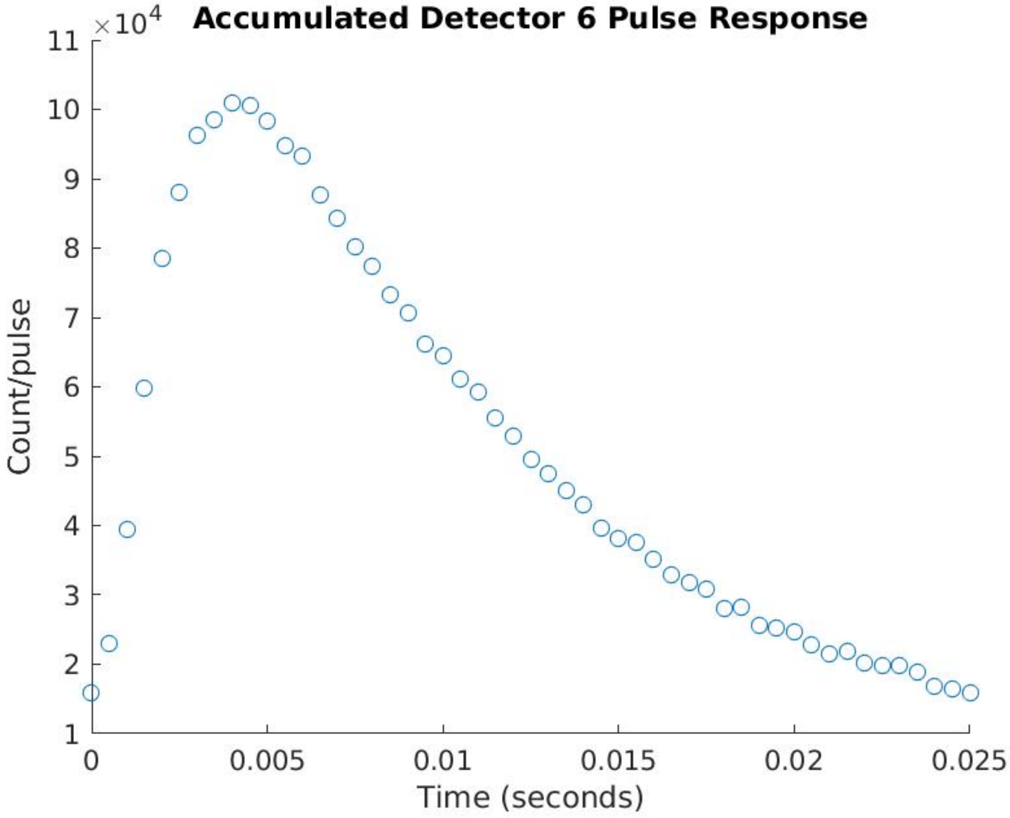

Figure 6.29: Helium-3 detector 6 accumulated count pulse profile with respect to time.

The Serpent-produced values of reactivity ρ, delayed neutron fraction β, prompt generation time Λ, prompt decay constant α (see equation (3.6)) and reactivity in dollars $-A_p/A_d$ (see equation (3.7)) are shown in the following table:

Table 6.10: Parameters produced directly from Serpent.

Parameter	Serpent computed values
ρ	-66.656 mk
β	6.377 mk
Λ	0.9129 ms
$-A_p/A_d$	-10.453 $
α	-80.001 mk/ms

Using the ρ value from Serpent, the accumulated pulse data and equation (3.7), β was computed then applied to equation (3.6).

Table 6.11: Cross solving the SA and SF equation using the ρ value from Serpent for power response.

Method	Cross computing SA and SF		
	Power response		
	Parameter	Value	Error%
SA	$-A_p/A_d$	-2.925 \$	-72.01
	β	22.785 mk	257
SF	α	-78.640 mk/ms	-1.70
	Λ	1.137 ms	24.59

Table 6.12: Cross solving the SA and SF equation using the ρ value from Serpent for detector 3 response.

Method	Cross computing SA and SF		
	Detector 3 response		
	Parameter	Value	Error%
SA	$-A_p/A_d$	-2.277 \$	-78.22
	β	29.271 mk	359
SF	α	-80.460 mk/ms	0.57
	Λ	1.192 ms	30.60

Table 6.13: Cross solving the SA and SF equation using the ρ value from Serpent for detector 6 response.

Method	Cross computing SA and SF		
	Detector 6 response		
	Parameter	Value	Error%
SA	$-A_p/A_d$	-2.230 \$	-78.67
	β	29.897 mk	369
SF	α	-80.320 mk/ms	0.40
	Λ	1.202 ms	31.68

Note that the errors are computed with respect to Serpent's predicted values shown in table 6.10. It is possible to see from the results in tables 6.11, 6.12 and 6.13 that the predictions of the reactivity in dollars $-A_p/A_d$ using the SA method were highly inaccurate and lead to significant overestimation of β by at least 257%. Additionally, using the resultant β in computing Λ, using the SF method resulted in at least 24.59% overestimation of Λ. However, the prediction of the prompt decay constant α using the SF method were within 1% deviation of the expected value. Using the Serpent produced values of β and Λ to alternately compute ρ, β and Λ using the SF method produced the following results:

Table 6.14: Solving the SF method equation using β and Λ from Serpent for power response.

Method	Use β and Λ from Serpent		
	Power response		
	Parameter	Value	Error%
SF	β	5.134 mk	-19.49
	Λ	0.9287 ms	1.73
	ρ	-65.412 mk	-1.86

Table 6.15: Solving the SF method equation using β and Λ from Serpent for detector 3 response.

Method	Use β and Λ from Serpent		
	Detector 3 response		
	Parameter	Value	Error%
SF	β	6.795 mk	6.57
	Λ	0.9077 ms	-0.57
	ρ	-67.073 mk	0.63

Table 6.16: Solving the SF method equation using β and Λ from Serpent for detector 6 response.

Method	Use β and Λ from Serpent		
	Detector 6 response		
	Parameter	Value	Error%
SF	β	6.667 mk	4.57
	Λ	0.9092 ms	0.40
	ρ	-66.945 mk	0.44

The Serpent-produced values of β and Λ were alternately substituted in equation (3.6) to solve for ρ, β and Λ separately, based on the computed decay constant α for each response. For detector 6 response, the predictions of β, Λ and ρ using the SF method were 0.44%, 0.40% and 4.57% respectively.

Chapter 7

Conclusions and Recommendations

The purpose of this thesis is to evaluate the feasibility of conducting a subcritical IMSR-400 physics test to demonstrate an overall negative temperature reactivity coefficient and explore the applicability of three reactivity measurement methods: 1) the Subcritical Multiplication method, 2) the Sjöstrand Area method and 3) the Slope Fit method. The study was primarily driven by particular interest in the experimental determination of the temperature reactivity coefficients, resulting from heating the graphite moderator and the molten fluoride fuel salt mixture. To that end, a subcritical scaled down version of the IMSR-400 (i.e. subcritical pile) was designed and modeled in Serpent, a continuous energy Monte-Carlo reactor physic code. The subcritical pile consists of an active core, graphite reflectors, instruments thimbles and source thimble. Vertical graphite channels, filled with the fuel salt and arranged in a hexagonal lattice comprises the active core. The active core is surrounded by graphite reflectors, used to reduce neutron leakage. Four instrument thimbles house eight helium-3 detectors, used to monitor the neutron flux inside the core. The source thimble houses a DD neutron generator, which emits quasi-monoenergetic neutrons semi-isotropically. Through the use of the DD neutron generator, an emulated criticality state of the neutron flux is maintained within the subcritical pile. The DD source was positioned at the center of the core to achieve symmetry of the flux profile.

Optimizing the size and siting of the helium-3 detector was done in order to minimize the adverse impact on the k_{eff} and the neutron flux shape, minimize primary neutron absorption, maximize sensitivity to change in neutron flux, minimize overshadowing between detectors, and improve accuracy of the Subcritical Multiplication method (see equation (3.5)). Selection of appropriate detector size and the total number of in-core detectors was done based on literature review. Siting of detectors was done by applying the Subcritical Multiplication method to thermal flux mapping data (see figures 4.4, 4.5, 4.6 and 4.7) in order to evaluate different zones potential to either overestimate or underestimate the k_{eff} of the core. Analysis showed that the core peripheral region is most appropriate for meeting optimization objectives. Positioning the eight helium-3 detectors in the core peripheral region resulted in a small total reactivity loss of 1.59 mk.

While operating the DD neutron source in constant mode, static (time independent) simulations were performed for the core isothermal temperature range 750 - 1000 K at 50 K increments. The Subcritical Multiplication method (see equation (3.5)) was used to compute k_{eff} and α_T based on the change in detector readings with each isothermal temperature change. Furthermore, assuming the DD source output fluctuates sinusoidally (0%, 1% and 2%) with a constant half-period of 20 seconds, dynamic (time dependent) simulations were performed, and k_{eff} and α_T profiles with respect to temperature were produced. The average predicted α_T from all cases is -13.4 pcm/K with a standard deviation of 2.48%, which shows that despite source fluctuation, accurate results can be obtained by accumulating enough neutron counts. The values of 10σ for source fluctuations of 0, 1 and 2% cases were four times higher than the static case. This can be attributed to the number of neutron histories used for the dynamic calculations. The dynamic mode generally requires a higher number of neutron histories for the same accuracy as the static mode. Hence, errors can be further reduced by utilizing more neutron histories. Nevertheless, the neutron signal change detectability condition (see equation (4.2)) was still satisfied by both static and dynamic simulations.

While operating the DD neutron source in pulsed mode, dynamic simulations were performed at 800 K core isothermal temperature. Fission power tally and two helium-3 detectors (3 and 6) were defined in Serpent to monitor the pulse response profile with respect to time. Averaged pulse profiles were analyzed using the Sjöstrand Area method and the Slop Fit method (see equations (3.7) and (3.6)) in order to compute the prompt decay constant (α), the delayed neutron fraction (β), and the prompt generation time (Λ). The combination of the Subcritical Multiplication method, the Sjöstrand Area method and the Slope Fit method in the determination of β and then Λ yielded highly inaccurate values, especially for β. Nevertheless, the prediction of α were withing 1% deviation of the expected value and produced reasonably accurate prediction of β and Λ. Although the predictions of the Sjöstrand Area method were inaccurate, it might still be useful for predicting the change in β for a circulating molten salt experiment.

To sum up, experimental determination of the isothermal temperature reactivity coefficient was proven feasible under different conditions for the subcritical physics test. Although, exact values of the temperature reactivity coefficients of the IMSR-400 may not be captured by the subcritical test, it would still be possible to demonstrate an overall negative temperature reactivity coefficient, which is characteristic of the IMSR-400. Furthermore, such experiment would help establish a baseline of expectations about fresh fuel salt neutronic and thermophysical properties, as well as, salt-graphite interactions.

In future work, a circulating fuel salt model will be designed and compared to the stagnated salt model. Applicability of the Sjöstrand Area method and Slope Fit method will be evaluated in predicting the change in β and reactivity loss due to circulation.

List of References

Adair, R. K. (1987). *The Great Design: Particles, Fields, and Creation*. Oxford University Press on Demand. 20

Ayllon, M., Adams, P. A., Batchelder, J. C., Bauer, J. D., Becker, T. A., Bernstein, L. A., Chong, S.-A., James, J., Kirsch, L. E., Leung, K.-N., *et al.* (2018). Design, Construction, and Characterization of a Compact DD Neutron Generator Designed for 40Ar/39Ar Geochronology. *Nuclear Instruments and Methods in Physics Research Section A: Accelerators, Spectrometers, Detectors and Associated Equipment*, **903**, 193–203. 44

Blanke, B., Bousquet, E., Jones, L., Murphy, E., and Vallee, R. (1956). Density of Fused Mixtures of Sodium Fluoride, Beryllium Fluoride, and Uranium Fluoride. Technical report, Mound Lab., Miamisburg, Ohio. 40

Brown, F. B. (2016). Monte Carlo Techniques for Nuclear Systems - Theory Lectures. *Los Alamos National Laboratory*, . 27, 28

Canadian Nuclear Safety Commission (2014a). REGDOC-2.4.1, Deterministic Safety Analysis. *Regulatory Document*, . 39

Canadian Nuclear Safety Commission (2014b). REGDOC-2.5.2, Design of Reactor Facilities: Nuclear Power Plants. *Regulatory Document*, . 39, 40

Canadian Nuclear Safety Commission (2019a). REGDOC-1.1.5, Supplemental Information for Small Modular Reactor Proponents. *Regulatory Document*, . 38

CANADIAN NUCLEAR SAFETY COMMISSION (2019b). REGDOC-2.4.3, Deterministic Safety Analysis. *Regulatory Document*, . 38, 39

CAPELLI, E., BENEŠ, O., AND KONINGS, R. (2014). Thermodynamic assessment of the LiF–NaF–BeF2–ThF4–UF4 system. *Journal of Nuclear Materials*, **449**(1-3), 111–121. 40, 55

CHABOT, G. (2009). Q&A: Instrumentation and Measurements - Surveys and Measurements (SM). 46, 47

CONCA, J. (2012). How Deadly Is Your Kilowatt? We Rank The Killer Energy Sources. 6

EIA (2019). EIA Projects Nearly 5% Increase in World Energy Usage by 2050, Led by Growth in Asia. 4

ENDO, T. AND YAMAMOTO, A. (2015). Theoretical expression of area ratio method using detected-neutron multiplication factor. *Trans. Am. Nucl. Soc*, **113**, 1208. viii, 35

GARLAND, W. J. (2014). *The Essential CANDU, a Textbook on the CANDU Nuclear Power Plant Technology*. McMaster University. 26

GILBERT, M. R., GHANI, Z., MCMILLAN, J. E., AND PACKER, L. W. (2015). Optimising the Neutron Environment of Radiation Portal Monitors: A computational study. *Nuclear Instruments and Methods in Physics Research Section A: Accelerators, Spectrometers, Detectors and Associated Equipment*, **795**, 174–185. 47, 48

GOBAIN, S. (2020). Helium-3 Neutron Proportional Counter. 47, 49

GOVERNMENT OF CANADA (2020). Uranium and Nuclear Power Facts. 1

GOVERNMENT OF ONTARIO (2017). Archived - The End of Coal. 2, 3

IPCC (2019). Global Warming of 1.5 C An IPCC Special Report on the Impacts of Global Warming of 1.5 C Above Pre-Industrial Levels and Related Global Greenhouse Gas Emission Pathways, in the Context of Strengthening the Global Response to the Threat of Climate Change. *Sustainable Development, and Efforts to Eradicate Poverty. https://www. ipcc. ch/sr15/. Accessed*, **1**. 3, 4

Lamarsh, J. and Baratta, A. (2001). *Introduction to Nuclear Engineering*. Prentice-Hall Inc., 3 edition. 1, 17

Leppänen, J. (2008a). *Serpent 1.1.0 Thermal Scattering Libraries Based on JEFF-2.2, JEFF3.1, ENDF/B-VI.8 and ENDF/B-VII*. Finland: VTT Technical Research Center. 54

Leppänen, J. (2008b). *Serpent 1.1.7 Cross Section Library Based on JEFF-3.11*. Finland: VTT Technical Research Center. 53, 55

Leppänen, J. (2013). *Serpent 1 User's Manual*. Finland: VTT Technical Research Center. 53

Lumen Learning (2020). Abundance of Elements in Earth's Crust. 1

Mei, L., Cai, X., Jiang, D., Chen, J., Zhu, Y., Liu, Y., and Wang, X. (2013). The investigation of thermal neutron scattering data for molten salt Flibe. *Journal of Nuclear Science and Technology*, **50**(7), 682–688. 55

Nuclear Energy Agency (2016). JEFF-3.2 Evaluated Data Library - Neutron data. 55

ORNL (1969). The Molten-Salt Reactor Experiment. 10

Persson, C.-M., Seltborg, P., Åhlander, A., Gudowski, W., Stummer, T., Kiyavitskaya, H., Bournos, V., Fokov, Y., Serafimovich, I., and Chigrinov, S. (2005). Analysis of Reactivity Determination Methods in the Subcritical Experiment Yalina. *Nuclear Instruments and Methods in Physics Research Section A: Accelerators, Spectrometers, Detectors and Associated Equipment*, **554**(1-3), 374–383. 33, 35, 45

Pioro, I. (2016). *Handbook of Generation IV Nuclear Reactors*. Woodhead Publishing. xii, 6, 7, 8

Power Technology (2017). The Bruce Power Generating Station Project. 2

Prince, B., Ball, S., Engel, J., Haubenreich, P., and Kerlin, T. (1968). Zero-Power Physics Experiments on the Molten Salt Reactor Experiment. Technical report, Oak Ridge National Lab., Tenn. 14

Robinson, R. (2016). Proposed IMSR400 Subcritical Physics Test Facility. Technical Specification Document: IMSR400-30500-TS-001. Unpublished. 37

Seidi, M., Behnia, S., and Khodabakhsh, R. (2014). Generalization of the Analytical Solution of Neutron Point Kinetics Equations with Time-Dependent External Source. *Journal of Theoretical and Applied Physics*, **8**(4), 211–218. 91

Starfire Industries LLC (2019). *nGenTM-400 Portable Neutron Interrogation*. 2109 S. Oak Street, Suite 100, Champaign, IL 61820 USA. 44, 45

Terrestrial Energy In (2016a). IMSR Molten Salt Reactor Technology. 8

Terrestrial Energy In (2016b). Status Report - IMSR-400. *Terrestrial Energy*, . 9

Wilson, P. D. (1996). The Nuclear Fuel Cycle from Ore to Wastes. *IAEA 2007, Management of Reprocessed Uranium – current status and future prospects*, . 5

List of Acronyms and Abbreviations

ARIS Advanced Reactors Information System.

CNSC Canadian Nuclear Safety Commission.

DD Deuterium-Deuterium Fusion Neutron Source.

IAEA International Atomic Energy Agency.

IMSR-400 Integral Molten Salt Reactor.

MSRE Molten Salt Reactor Experiment.

ORNL Oak Ridge National Laboratory.

SA Sjöstrand Area Method.

SF Slope Fit Method.

SM Subcritical Multiplication Method.

TEI Terrestrial Energy Incorporated.